

https://dspace.org/

Reprocessing of legacy seismic profile using advanced algorithms for shale gas exploration in the Karoo Basin (South Africa)

Robel, Berhanu

2024

University of the Witwatersrand, Johannesburg

https://hdl.handle.net/10539/50258

Robel, Berhanu. (2024). Reprocessing of legacy seismic profile using advanced algorithms for shale gas exploration in the Karoo Basin (South Africa) [Master's dissertation, University of the Witwatersrand, Johannesburg]. WIReDSpace. https://hdl.handle.net/10539/50258

Downloaded from a DSpace repository. https://dspace.org/

Reprocessing of legacy seismic profile using advanced algorithms for shale gas exploration in the Karoo Basin (South Africa)

Masters of Science (Dissertation) in Geophysics

School of Geosciences
University of the Witwatersrand, Johannesburg

Berhanu Robel
1348744

24 March 2024



A Dissertation submitted to the Faculty of Science, University of the Witwatersrand, Johannesburg, in fulfillment of the requirements for the degree of Master of Science.

Declaration

I, Robel Berhanu, declare that this dissertation is my own, unaided work. It is being submitted for the Degree of Masters of Science (dissertation) in the field of Geophysics at the University of the Witwatersrand, Johannesburg. It has not been submitted before for any degree or examination at any other University.



(Signature of candidate)

day of 24 March 2024

* Dissertation or Research Report as applicable

or Master of Science as applicable.

Abstract

The utilization of the reflection seismic technique has emerged as a crucial factor in the search for minerals and hydrocarbons due to its proficiency in producing visual representations of objects located at considerable depths (more than 500 m). Over the past 50 years, South Africa has accumulated and retained numerous reflection seismic profiles for the purpose of mineral exploration. As an example, by the end of 2003, the Anglo American Corporation of Gold Division had conducted over 36,000 km of reflection seismic surveys. This means that it is crucial to continuously enhance current seismic processing techniques and devise novel strategies to extract valuable information from previously collected seismic data. This research focuses on the reprocessing of a legacy reflection seismic profile from the Karoo Basin. The importance of reprocessing the data lies in improving imaging quality with the help of modern processing software that utilizes the implementation of advanced algorithms. It has been suggested that the Karoo Basin located in South Africa may contain shale gas that could be potentially extracted. Its potential has to be evaluated by considering different subsurface structures, such as dolerite dykes and sills that were formed following the deposition of sediments in the basin. Given the area's gas exploration potential, a legacy reflection seismic profile was reprocessed using standard processing workflow and the final reprocessed stacked section was compared with the legacy stacked section produced in 1992. The aim is to produce a seismic section with improved quality and resolution so that the area's underlying geological structures, e.g., dolerite sills, gas escape features, and geological boundaries, can be mapped. The findings indicate that enhancing the seismic section's quality can be achieved by reprocessing the profile. The reprocessing results exhibit adequate improvement in the quality of the data compared to the legacy stacked section. Some of the improved geological features include the dolerite intrusions, stratigraphic boundaries, and gas escape features present in the subsurface of the study area. In addition to a careful selection of pre-stack processing parameters and noise removal filters applied in this study, the main improvement in the data quality is due to the new velocity model and migration algorithm (e.g., Kirchhoff algorithm) used in the new processing workflows compared to the workflows that were used in the 1990s. In particular, the new velocity model is more accurate because the velocity picking was constrained by the latest borehole information and physical property studies (e.g., seismic velocity and density) conducted by others in the Karoo Basin. This outcome can be used to guide future exploration efforts and seismic designs in the region.

Acknowledgements

This research is aided by the Petroleum Agency South Africa (PASA) as part of the Shale Gas Initiation project. I thank Anglo Gold Ashanti for donating the data presented in this paper.

To my supervisors, Prof. Musa Manzi and Dr. Stephanie Enslin, I would like to convey my profound thanks and appreciation for their advice, willingness, and patience in helping me at every stage of the research project. I consider it a great honor and blessing to have worked with you and learned from you; it is a privilege I will always value.

Additionally, I would like to express my gratitude to my friends and colleagues for their help, for devoting their important time to peer review part of the work, and for their insightful and constructive criticism.

Above all, I want to thank my parents for everything they have done for me, for their love, financial support, and encouragement as well as for paving the way for me to succeed. My wonderful family for their encouragement and confidence in me. I'm grateful.

Contents

Preface

Declaration i
Abstract ii
Acknowledgements iii
Table of Contents iv
List of Figures vii

List of Figures **vii**

List of Tables 1

1 Introduction **1**

1.1 Background 1
1.2 Aims and Objectives 3
1.3 Project Outline 4

2 Geology of The Karoo Basin **5**

2.1 Overview 5
2.2 Exploration Wells in the Karoo Basin 7

3 Theoretical Background and Literature Review **10**

3.1 Seismic Technique 10
3.2 Seismic Prospecting 15
3.2.1 Different Types of Seismic Waves 15
3.2.2 Properties of Seismic Events 18
3.2.3 Seismic Noise 20
3.3 Field Equipment for Seismic Exploration 21
3.3.1 Seismic Sources 21
3.3.2 Vibroseis 21
3.3.3 Seismic Receivers 23
3.4 Two Dimensional Survey Design 25

3.4.1 The Near-surface Layer . . . 25
3.4.2 The Shallow Layer . . . 26
3.4.3 The Target Layer . . . 26
3.4.4 Group Interval . . . 26
3.4.5 The Fresnel Zone . . . 26
3.4.6 The Far Offset . . . 27
3.4.7 The Recording Length . . . 27
3.4.8 The Sampling Rate . . . 28
3.4.9 The Group Interval . . . 28
3.4.10 The Fold Coverage . . . 28
3.4.11 Interval of the Source . . . 29
3.4.12 The Position and Orientation of Line(s) . . . 29
3.5 Theoretical Aspects of Processing Seismic Data . . . 29
3.5.1 Demultiplexing . . . 29
3.5.2 Preprocessing . . . 30
3.5.3 Creating CDPs - Crooked Line Binning . . . 30
3.5.4 Floating Datum Static Corrections - Concept . . . 31
3.5.5 Geometric Spreading . . . 32
3.5.6 Automatic Gain Control . . . 33
3.5.7 RMS Amplitude AGC . . . 34
3.5.8 Noise Suppression . . . 34
3.5.9 Pre-stack Deconvolution . . . 36
3.5.10 Velocity Analysis . . . 37
3.5.11 Correcting Normal Moveout Velocity for a Flat Reflector . . . 38
3.5.12 Correcting Velocity for Dipping Reflectors . . . 39
3.5.13 Migration . . . 41
3.5.14 Migration Algorithm: Kirchhoff Migration . . . 44

4 Methodology **46**
4.1 Acquisition of Profile RT480 . . . 46
4.2 Processing Profile RT480 . . . 47
4.2.1 High-level Overview . . . 47
4.2.2 Building the Geometry from SPS Data . . . 48
4.2.3 CDP Sorting . . . 49
4.2.4 Floating Datum Static Corrections . . . 49
4.2.5 Merging Trace Headers and Geometry . . . 50
4.2.6 Verifying Correctness of Geometry . . . 51

4.2.7 Generating a Brute Stack . . . 52
4.3 Application of Gain Recovery Functions . . . 53
4.4 Pre-stack Processing . . . 54
4.4.1 First Break Picking . . . 54
4.4.2 Dealing with Poor Picks . . . 56
4.4.3 P-wave Refraction Tomography . . . 57
4.4.4 Refraction Statics . . . 58
4.4.5 Inversion Model . . . 58
4.4.6 Noise Suppression . . . 62
4.4.7 Pre-stack Deconvolution . . . 65
4.4.8 Velocity Analysis . . . 67
4.5 Stacking . . . 68
4.6 Post-Stack Processing . . . 69
4.6.1 Applying Seismic Migration . . . 69
4.6.2 Synthetic Seismogram . . . 70
4.6.3 Correlating the Section With a Synthetic Seismogram . . . 71
4.7 Summary - Methods . . . 73

5 Results and Discussions **75**
5.1 Seismic Resolution Limit . . . 75
5.2 Comparing Legacy and Reprocessed Data . . . 76
5.2.1 Technical Comparisons . . . 76
5.2.2 Structural Comparisons . . . 79
5.3 Interpretations . . . 86
5.3.1 Refraction Tomography . . . 86
5.3.2 Seismic Section . . . 87

6 Conclusion **91**

References **92**

List of Figures

1.1 (a) South African map showing the extent of the Karoo Basin. The red square bounds the legacy survey line used in this investigation. (b) This image zooms into the local geological setting of the study area. 3

2.1 A geological map of the study area showing the location of the 2D seismic line (black line) in relation to the Karoo sedimentary rocks. (b) Aeromagnetic data of the survey area (Scheiber-Enslin et al., 2021). The high magnetic responses are most likely caused by the the dolerite outcrops present in the region. 7

2.2 The geo-tectonic map of the Cape-Karoo region of southern Africa, with the locations of the examined deep boreholes (shown as white dots) and correlation profiles (shown as black lines). The Great Escarpment is also demarcated by the broken white line that runs around its perimeter. LIP (Large Igneous Province) (Linol et al., 2016). 8

3.1 Seismic design showing how a wireless or nodal system can be used to acquire the land seismic data (Makama et al., 2021). 12

3.2 (a) Seismic shot record taken from the data reprocessed in this study. One can observe some of the most common types of seismic waves such as primary waves (red arrows), ground rolls (blue arrows), and hyperbolic reflections (green arrows). This shot record has high-frequency signals caused by electrical noise (black arrows). (b) Frequency spectrum graph of the shot record. The spikes present approximately between 45 Hz and 50 Hz are most likely caused by background noise in the shot record as well as electrical noise such as power line signals. 14

3.3 (a) General trend for the propagation of compressional waves (P-waves) in a solid medium. (b) General propagation of shear waves (S-waves) in a solid medium (Bolt, 1978). 16

3.4 (a) Propagation of Love waves. The waves propagate in the same direction as the motion of the particles that make up the medium. (b) Propagation of Raleigh Waves (also known as ground rolls.). These waves propagate at a right angle to the direction of motion of the particles that make up the medium (Bolt, 1978). 17
3.5 The rays produced when a P-ray makes an oblique impact on a geological boundary that separates two media with distinct seismic velocity and densities. In this context, P denotes primary waves, and S signifies secondary waves. Additionally, V is the velocity of either primary or secondary waves, and ρ indicates the density of the respective layer (Kiran, 2005). 20
3.6 An example of the vibroseis truck in the field (Fathi et al., 2016). 22
3.7 An example of a geophone (a) and its internal components (b) (Spain et al., 1991). 24
3.8 Internal components of a node and the way in which the connections are configured electrically (Makama et al., 2021). 25
3.9 The Fresnel zone within a medium that is not uniform in all directions (anisotropic medium). The phase angles θ_1 and θ_2 are measured at specific points on wavefronts occurring at two different times: $t = t0$ and $t = t_0+\Delta t$ (Xu and Stovas, 2018). 27
3.10 To capture seismic data, channels are sampled simultaneously through demultiplexing. In this case, the data are organized into columns of samples, with one channel's samples appearing first. The samples from the subsequent channels M and N represent the recording channel and the time sample, respectively (Yilmaz, 2001, p. 43). 30
3.11 (a) These are the paths of rays linked with a horizontally level reflector that goes from the location of the shot (S) to multiple receivers (D). (b) Shows a possible common depth point (CDP) arrangement for a dipping reflector as seismic waves propagate from shot to receiver locations (Xue et al., 2016). 31
3.12 A schematic representation of geometric spreading of wavefronts. The frequency of the waves is reduced as the distance from the source increases and their respective wavelengths increase, therefore the geometric spreading correction must be applied to the data (Onajite, 2013). 33
3.13 Normal moveout (NMO) diagram of a flat/horizontal reflector. Here, S is the seismic source, G is the seismic receiver, M is the halfway between the seismic source and receiver, and D is the point at which the incident seismic ray is reflected (Yilmaz, 2001, p. 280). 38

3.14 Normal moveout (NMO) geometry for a single dipping reflector. This figure shows the source (S), the receiver (G), the distance between the source and the receiver (x), the midpoint between the source and receiver (M), the angle of incidence (α), the dip angle (ϕ), and point of reflection (D) (Yilmaz, 2001, p. 287). 39

3.15 The ray path for a reflection with zero offset off of a horizontal reflector. Here, the velocity of a layer is given by V and the density of a layer is given by ρ (Xue et al., 2016). 42

3.16 The ray path for a reflection with zero offsets from a dipping reflector, as well as the subsequent apparent dip (Xue et al., 2016). 43

3.17 The diagram shows how Kirchhoff migration sums an input of diffraction energy (a) summed and at the point of scatter and (b) the migrated section (Baker and Copson, 2003). 45

4.1 The initial map of the seismic profile with the survey pegs color-coded with the respective values of shot elevations. 49

4.2 The midpoints of shot-receiver pairs, color-coded by offset and elevations. The common depth point (CDP) bins were assigned throughout the center of the profile. The red circles on the cloud represent automatically generated hitpoints that enable one to define a path for the CDP bins to follow along the seismic profile. 49

4.3 Common Depth Point (CDP) - Time display of floating datum elevation statics for the profile. This correction helps reduce undesired seismic velocity variations across the profile and it was performed during the geometry setup process. 50

4.4 Two-dimensional view of the seismic line after geometry setup. At this stage, the geometry data were generated from the standard point source (SPS) database and were merged with the data across the common depth point (CDP) intervals. 51

4.5 (a) Shot gather with marked offset. The offset (red line) was converted to time using a constant velocity value. The first arrivals in the seismic shot match the peak of the red line, demonstrating that the earliest arrivals correlate to the lowest offsets. (b) Frequency spectrum of the shot record. 52

4.6 Preliminary brute stack of the entire profile. This is a brute stack of the raw shots generated after establishing the geometry of the seismic data. The red and black arrows indicate some reflections associated with boundaries between the layers, the blue arrows show dipping reflection events associated with sills, the light green arrow around 11 s two-way travel time (TWT) shows some noise in the data and the green arrows show some of the seismic reflection events present at greater depths. . . . 53

4.7 (a) Raw shot gather from the seismic data before applying a recovery function. One can observe that it is difficult to identify most of the seismic waves, e.g., noise (black arrows), P-wave first breaks (red arrows), ground rolls (blue arrows), and P-wave reflections (green arrows). (b) The same shot gather after applying normal AGC (automatic gain control) with a window length of 300 ms. It is evident that AGC helps enhance the desired signals of the wavelets. The different seismic events are indicated with the corresponding arrows. 54

4.8 (a) Manual first break picking performed on a shot gather, the red line along the first arrivals represents the picks applied on this gather. (b) The shot gathers is flattened using a linear moveout approach to determine if the picks are done correctly. A straight line (red) indicates that the correct picks have been applied. 55

4.9 Time-offset plot obtained to check quality of picks. All shots are included and a polygon selection method was applied to eliminate poor picks and reserve the better ones so that refraction statics are applied as accurately as possible. 56

4.10 (a) The refraction tomography of P-wave velocities for the seismic data. (b) The path followed by the seismic waves during propagation (ray path diagram). 57

4.11 (a) Velocity model window obtained for the initial velocity model. The structure of the subsurface is shown in elevation, with the strata being color-coded according to the speed at which they move. (b) First break picks for each shot gather. (c) The model of the sub-weathering layer. . . 59

4.12 Root mean square (RMS) calculation graph. This graph shows the process followed to quantify the root-mean-square value contrast between the calculated first break picks and a general model interpolated using the processing software. 60

4.13 (a) Elevations statics. (b) Residual statics. (c) Total statics. These are the static view windows for the seismic data. Receiver statics (blue) and shot statics (red) are shown across all windows. The total statics obtained (c) were by merging the model-based and the residual statics corrections represented by (a) and (b) respectively. 61

4.14 Results of applying the total corrections on the shot records is shown in this figure. (a) The original shot gather, (b) The shot gather after applying floating datum correction, and (c) The shot gather after applying total statics corrections. Primary waves (red arrows) and hyperbolic reflections (blue arrows) are the target events for correction and have been corrected sufficiently. 62

4.15 (a) A shot gather before applying a top mute. (b) The same shot gather after applying a front mute. The red arrows in both sub-figures show the noise removed using the muting process. 63

4.16 (a) The frequency-wavenumber (f-k) showing the original data. (b) Data after applying the f-k domain mute in the noise cone. 64

4.17 (a) A shot gather before applying an f-k (frequency-wavenumber) and a BS (band stop) filter. One can observe a ground roll cone (highlighted in purple). (b) The same shot gather after the application of f-k filtering, where ground rolls are removed. (c) Frequency spectrum graph with a very sharp spike between 45 Hz and 50 Hz. (d) Frequency spectrum graph after applying a bandstop filter. The spike on the frequency spectrum has been eliminated. 65

4.18 (a) A shot gather before applying deconvolution. (b) The same shot gather after applying deconvolution with a gap length of 36 ms. This length varies amongst different shot gathers. It is evident that wavelets are compressed and short-period multiples are reasonably eliminated (as shown with blue arrows). (c) The frequency spectrum graph of the record before deconvolution. (d) Frequency spectrum graph after deconvolution. 66

4.19 Velocity model for the seimic profile. The primary and secondary wave velocities of all the rock types that the profile covers were approximated using time values of reflections using a semblance approach. They were saved as NMO (Normal moveout) files. (a) Stacked section with estimated velocities across the entire profile. (b) The resulting velocity model with their estimated values. (c) The resulting velocity model. 67

4.20 Stacked section of the seismic profile RT480. This stack was Normal moveout (NMO) corrected using the velocity model generated from velocity analysis. No migration applied. 68

4.21 Stacked section of the seismic data. The red arrows show that the reflections were moved to their true depths (red arrows). Kirchhoff migration with a migration velocity of 5000 m/s was applied to achieve this image. 69

4.22 (a) A segment of the raw stack, with displaced reflections (red arrows). (b) The segment after applying 2D Kirchhoff migration to the seismic data. Kirchhoff migration with a migration velocity of 5000 m/s was used in this case, the reflections (red arrows) are geometrically relocated to their true position. 70

4.23 This synthetic seismogram was created using a sampling rate of 2 ms and a dominating frequency of 30 Hz. It contains characteristics of both minimum and maximum-phase wavelets. A synthetic seismogram helps us understand how seismic waves travel through different subsurface layers. They assist in interpreting stratigraphic features and identifying key seismic reflections. In this case, one can observe highly reflective events between 0.5 s and 1.5 s on the seismogram and they are associated to the geological boundaries present between 0.5 s and 1.5 s on the seismic section. 71

4.24 (a) Well log WE 1/66 (Scheiber-Enslin et al., 2021). (b) The synthetic seismogram was generated using velocity, density, and depth values observed in the area to calculate impedance and reflection coefficient. (c) A segment of the seismic data showing stratigraphic boundaries. One can generally observe that the depths of reflections from the stack correlate well with reflections obtained from the synthetic seismogram. 73

5.1 Comparing the original stack section (a) to the reprocessed stack section (b), areas with significant enhancements are highlighted in rectangles. Detailed views of these areas are presented in Figures 5.2 and 5.3. (c) Frequency spectrum graph of the entire legacy stack. (d) Frequency spectrum graph of the entire reprocessed data. 81

5.2 Close-up areas of the legacy stack (a) and reprocessed stack (b) with a frequency spectrum graph obtained for these particular sections (c). The reprocessed data (b) clearly image the geometry and continuity of the sills with increased quality as compared to the legacy one (a). This is shown using black arrows in the figure. The frequency trend of the reprocessed data is evidently smoother than the legacy data. The key observation here is that the higher frequencies on the legacy spectrum are adequately eliminated in the reprocessed section. The high frequencies on the legacy data are most likely related to noise that was not handled efficiently. . . . 83
5.3 Close-up areas of the legacy stack (a) and reprocessed stack (b) with a frequency spectrum graph obtained for these particular sections (c). The reprocessed data (b) clearly image the continuity of the base of the Ecca Group with increased quality as compared to the legacy one (a). This is shown using black and white arrows in the figure. The frequency trend of the reprocessed data is evidently smoother than the legacy data. The key observation here is that the higher frequencies on the legacy spectrum are highly eliminated in the reprocessed section. The high frequencies on the legacy data are related to noise. 84
5.4 Close-up areas of the legacy stack (a) aligned with those of the reprocessed stack (b). The black, white, and red arrows point to possible reflection events enhanced by reprocessing. (c) Corresponding frequency spectrum. High frequencies on the legacy spectrum are eliminated in the reprocessed section. 85
5.5 Close-up areas of the legacy stack (a) aligned with those of the reprocessed stack (b). The black, white, and red arrows point to possible reflection events enhanced by reprocessing. (c) Corresponding frequency spectrum. High frequencies on the legacy spectrum are eliminated in the reprocessed section. 85
5.6 Elevation profile of RT480. Here, the elevation difference (black line) across the survey line is plotted against peg numbers (blue line) assigned to each shot and receiver location. 86
5.7 (a) The refraction tomography of P-wave velocities for the data. (b) The path followed by the seismic waves during propagation (ray path diagram). 87
5.8 (a) Top 2 s TWT of time migrated zero offset seismic section for profile RT480 with prominent near-surface events highlighted. (b) One can interpret the three major stratigraphic groups and dolerite intrusions. (c) Well log WE 1/66 (Scheiber-Enslin et al., 2021). 88

5.9 Seismic section highlighting some of the geological artifacts such as sills and boundaries. The red arrows point to the features as labeled in the figure. 89
5.10 Seismic section highlighting major geological boundaries (red arrows) and an example of a gas escape feature (yellow oval shape). 89
5.11 Full 16 s two-way traveltime (TWT) post-stack time migrated seismic section. Major reflection events are evident on the stack, mostly in the top 2 s TWT. 90

1. Introduction

1.1 Background

The possibility of the Karoo Basin in South Africa being a shale gas reserve has been acknowledged, and it spans over 50% of the country. This means that the potential for shale gas needs to be investigated by considering several features in the subsurface, such as dolerite sill materials that were formed after sedimentation in the basin. These structures may also be associated with gas escape features. The shales in the deeper southern section of the basin form part of the Whitehill and Prince Albert Formation of the Ecca Group (Catuneanu et al., 1998). The basin was covered by lavas produced from the Karoo Large Igneous Province (LIP) intruded by a deep network of dolerite dykes and sills after the Karoo sedimentation process (Du Toit, 1920; Duncan and Marsh, 2006).

Given the potential of the area to provide significant shale gas energy reserves, initial estimates suggested that 450 tcf (trillion cubic feet) was possible. However, further inspections considering the repercussions of the dolerite network resulted in lowered estimates for the reserves. The new estimates from several studies include a probabilistic range between 14 - 172 tcf from Decker and Marot (2012) and 10 to 50 tcf (trillion cubic feet) from Chere et al. (2017) for the Whitehill, Collingham and Prince Albert Formations, i.e., the Lower Ecca shales.

As part of the investigation for the presence of oil and gas, legacy reflection seismic data were collected in the basin during the 1960/1970s. These data show that the maturity of the Karoo Basin increases towards the south, which may be due to the increased depth of burial and Cape Fold Belt metamorphism (Leith, 1970; Rowsell, 1976). Additionally, dolerite sills have intruded the shale layers of the Whitehill and the Prince Albert formations, resulting in the heating of the shale strata (Cawthorn, 2012).

The heating could result in the maturation of hydrocarbons and gas escape features in deeper sections of the basin (Svensen et al., 2004; Aarnes, 2011). Furthermore, seismic

methods have improved over the past years. Some of the main reasons for these improvements are the evolution of technology and engineering that produced various ways to upgrade existing hardware equipment required for acquisition and software products used for processing field data.

Considering the significance of developing effective techniques to acquire and process seismic data, this research focused on the reprocessing of a legacy seismic profile located in the eastern section of the basin. The reprocessing using modern technology is essential because it has been demonstrated in several legacy reprocessing workflows that this allows a significant improvement in structural imaging quality and signal-to-noise ratio (S/R) (Manzi et al., 2019; Westgate et al., 2020). For this reason, the profile is reprocessed with the intention of improving reflections corresponding to all observable subsurface structures.

Figure 1.1 shows the location of the seismic survey conducted in the basin (SW of Lesotho) close to the town of Trompsburg. About 65 km of the profile runs along the Kaapvaal craton's southern boundary. Two discrete crustal blocks seem to be defined by seismic reflectors in the top crust, which is separated by a southeast-dipping border. According to De Wit and Tinker (2004), there does seem to be an overthrust of Kaapvaal Craton crust by the younger terrain (>11 s TWT or > 35 km). It is possible that the lithosphere under the Natal - Namaqua area extends to depths more than 150 km, according to the regional Kaapvaal Project teleseismic array (Fouch et al., 2004). All of this is in agreement with surface geology (Thomas et al., 1994; Schmitz and Bowring, 2003).

.

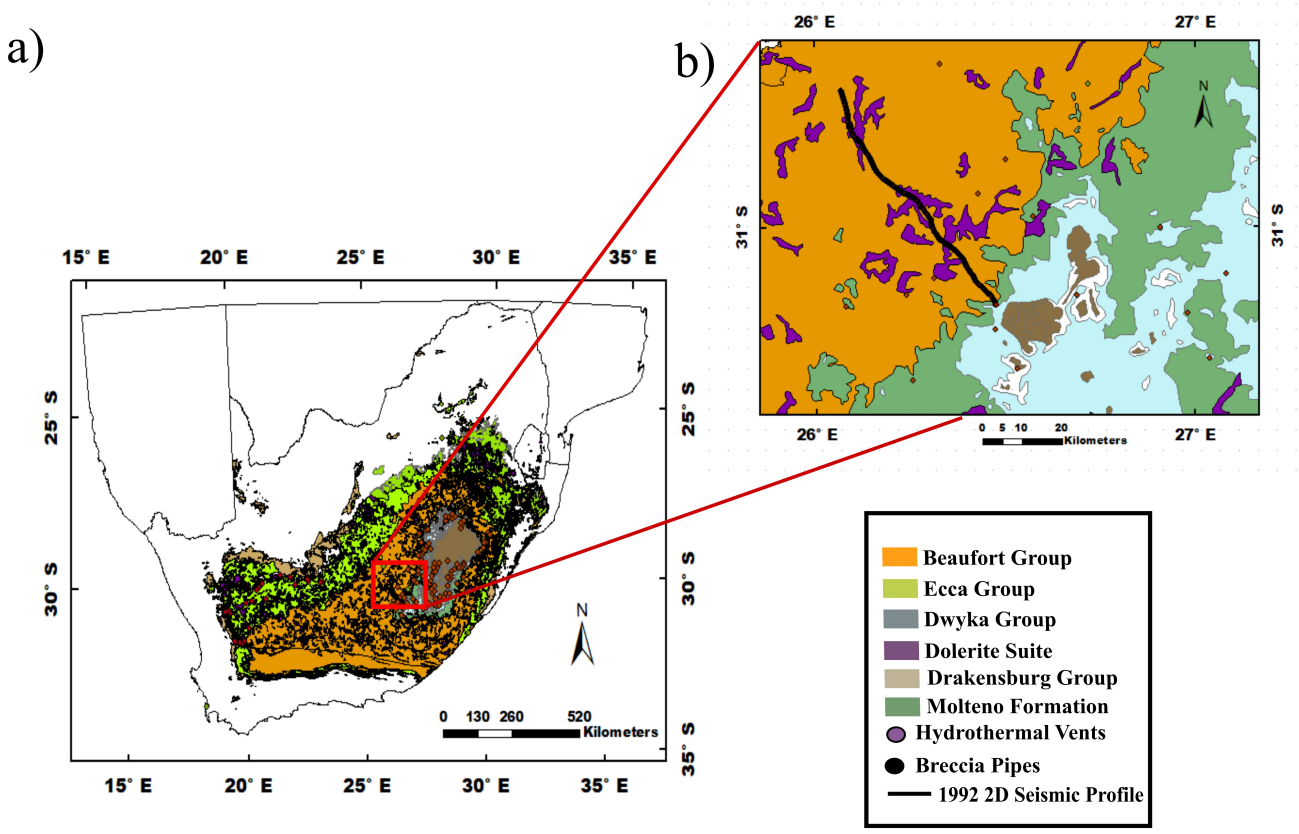

Figure 1.1: (a) South African map showing the extent of the Karoo Basin. The red square bounds the legacy survey line used in this investigation. (b) This image zooms into the local geological setting of the study area.

1.2 Aims and Objectives

The primary aim of this research is to reprocess a legacy seismic profile within the Karoo Basin of South Africa. The processed data will then be used to investigate some geological features like dolerite dykes and sills, the Moho discontinuity, or gas escape features to see if there is improved imaging. The data were acquired in 1992 by Anglo Gold Ashanti.

It is necessary to examine this basin's potential while taking into account the sill and dyke materials that were formed following the basin's sedimentation since it has been recognized as a prospective shale gas resource. Their penetration caused the basin's explosive gas releases, which are visible on the surface as breccia pipes and hydrothermal vents. The primary objective of the acquisition was to investigate the gold-bearing horizons of the Witwatersrand basin below the thick cover. However, nothing was found.

The specific objectives of this research are as follows.

(a) Reprocess the legacy 16s reflection seismic data using modern processing workflows.

(b) Investigate how the new processing algorithms and new velocity model can improve subsurface depth imaging.

(c) Image complex geological structures such as the shale layer, sills, and gas escape structures.

To make the investigation possible, the data are taken through a sequence of standard seismic processing methods using advanced software (Globe Claritas) and a custom Matlab program.

1.3 Project Outline

(a) **Chapter 2** explains the geological background of the Karoo Basin.

(b) **Chapter 3** looks at the theoretical aspects of seismic data acquisition and processing.

(b) **Chapter 4** discusses the methods followed to reprocess the seismic data.

(b) **Chapter 5** focuses on the results and interpretations of the data.

(b) **Chapter 6** outlines the conclusions drawn from the research.

2. Geology of The Karoo Basin

2.1 Overview

The Karoo Basin is a sedimentary basin that evolved between 350 and 200 Ma (Cole, 1992). In lower successions, the basin is made up of the glacial deposits of the Dwyka Group (Carboniferous to Early Permian; 300 - 268 Ma), followed by the Permian (286 -252 Ma) rhythmites and turbidites of the upper and lower Ecca Group, respectively (Cole, 1992; Catuneanu et al., 1998). Fluvial and aeolian deposits of the Beaufort Group and Molteno, Elliot, and Clarens formations make up the upper succession in the basin (Scheiber-Enslin et al., 2021).

The Molteno, Elliot, and Clarens formations were deposited in the late stages of the Permian (252-183 Ma), where the observed geological time range is between 237 and 230 Ma (Cole, 1992; Catuneanu et al., 1998). Moreover, the Elliot, Molteno, and Clarens formations are covered by lavas of the Drakensberg Group (Duncan et al., 1997). The lavas have pillow basalts at their base, and recent dating shows that they were extended between 186 and 184 Ma (Nengovhela et al., 2021). It is also evident that these lavas are cross-cut by a network of dolerite dykes and sills, which have been U-Pb zircon dated. The dating results show that the features were emplaced around 183 Ma (Svensen et al., 2004).

The change from glaciomarine (Dwyka) to marine (Ecca) ecosystems was slow, spanning the time period in which the floating ice was entirely melted, making it difficult to precisely define the Dwyka-Ecca border in the south. The northern Dwyka succession is composed of fluviodeltaic sequences that contain coal due to the gradual deglaciation of the continental regions during the Artinskian, which is overlain in certain places by marine shale from the Pietermaritzburg Formation of the Ecca Group (Smith et al., 1993). A ravinement surface formed during the marine incursion of the Ecca Sea serves as a representation of the abrupt boundary between the Dwyka and Ecca Groups in this instance. The proportion of dropstones in the rock steadily declines upward over the transition period between the Dwyka and Ecca Groups, corresponding to the melting of

the floating ice (Catuneanu et al., 1998).

The rocks that make up the Whitehill Formation are carbonaceous shale formed in deep water, pelagic, and reducing environment, which weathers to a white color. The Collingham Formation is considered to represent a distal underwater fan facies connected to wind-blown interbedded volcanic ash and pelagic sedimentation (Cole, 1992). The lithofacies comprise alternate layers of siltstone and shale with yellowish tuff.

All bounding surfaces are consistent in the southern portion of the basin, including the base and top of the Ecca Group and the boundaries between formations (Svensen et al., 2004). In the distal sector, the base of the Ecca Group is distinctly uncomfortable (ravinement surface), as is the base of the Volkrust Formation in connection to the Ecca Sea's transgression over the nonmarine Vryheid facies. The remaining bounded surfaces (the tops of the Pietermaritzburg and Volkrust formations) are conformable (Visser, 1986; Cole, 1992; Svensen et al., 2004).

Flat sills support sloping sheets that extend outward from the borders of these sills and create large dipping sheets that are more than 150 km long at deeper stratigraphic levels (i.e., within the Ecca and Dwyka Groups, outcropping in the southern half of the basin) (Scheiber-Enslin et al., 2014). At times, the inclined sheets extending from these sills' borders at depth might cut through the strata for as much as 5 km before they outcrop. In the Faroe-Shetland Basin, situated off the coast of Scotland, high-resolution seismic data demonstrate how these sills may join to build a sill network, a phenomenon known as a compound sill (Hansen et al., 2004; Svensen et al., 2004).

Figure 2.1 shows seismic profile RT480 and the geological stratigraphy it crosses. The profile crosses sedimentary rocks belonging to the Beaufort Group. The profile ends towards the southeast, where there is sedimentary strata belonging to the Clarens, Elliot, and Molteno formations. The line stops in a massive circular outcropping of Drakensberg Group pyroclastic debris and lava (15 km in diameter). Dolerite sills and dykes are also visible from the seismic line's path. About 20 km of the seismic line, at least 8 hydrothermal vents have been identified from the outcrop or Google Earth (Svensen et al., 2006).

According to Svensen et al. (2006), breccia pipes are the most common kind of gas escape features in the southwestern Karoo, whereas hydrothermal vents are more common in the eastern Karoo and are dominated by sediments. Hydrothermal vent complexes, kimberlite pipes, and volcanic necks or plugs linked with the Karoo LIP (Large Igneous

Province) may all be found in the eastern Karoo surrounding Lesotho (Scheiber-Enslin et al., 2021). Explosive phreatic processes are attributed to creating these hydrothermal vents. In addition, degassing connected to comparable vents of varying ages in the Cretaceous Voring and more basins in the Norwegian Sea has been related to Eocene global warming (approximately 55 million years ago) (Svensen et al., 2004).

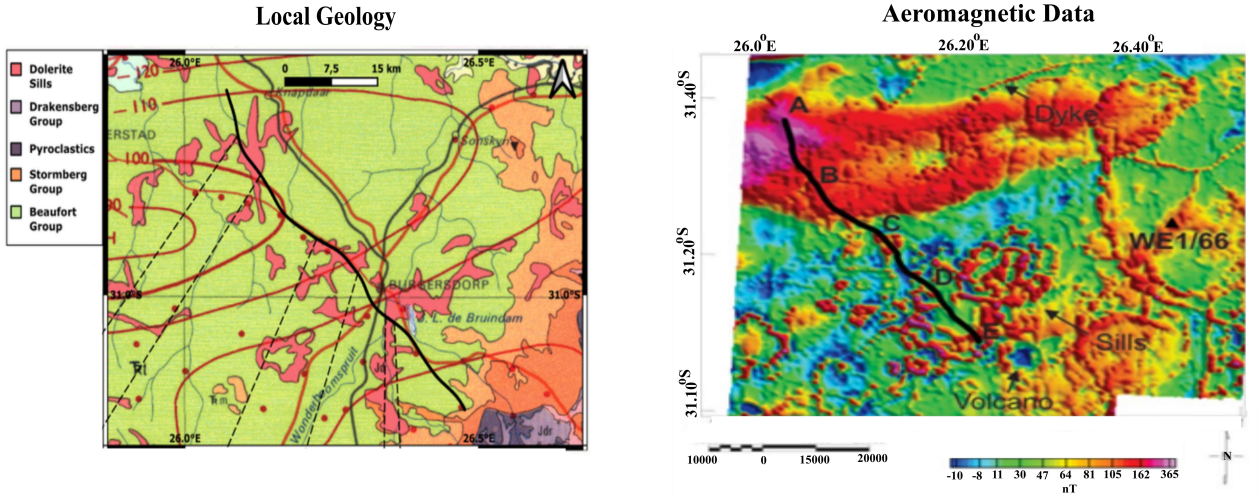

Figure 2.1: A geological map of the study area showing the location of the 2D seismic line (black line) in relation to the Karoo sedimentary rocks. (b) Aeromagnetic data of the survey area (Scheiber-Enslin et al., 2021). The high magnetic responses are most likely caused by the the dolerite outcrops present in the region.

2.2 Exploration Wells in the Karoo Basin

In previous investigations, field research and mapping have provided a large amount of data on the overall stratigraphy as well as the structure of the basin. However, modern subsurface information available is not adequate (Linol et al., 2016). In addition to the multiple seismic lines acquired across the southern part of the basin in the 1960s, there are 19 well logs with depths ranging from 1 to 5.5 km were drilled by the Southern Oil Exploration Corporation (SOEKOR), now called PASA (Petroleum Agency of South Africa) (Winter and Venter, 1970).

The logs demonstrate that the most prominent occurrence of the sills is towards the east, northeast, and western sides of the basin with significant variations (Scheiber-Enslin et al., 2014). The logs show that more than 150 m of sill matter was emplaced in these areas throughout the stratigraphic column (Cawthorn, 2012; Scheiber-Enslin et al., 2021).

Figure 2.2 shows the location and depths of the logs drilled across the basin.

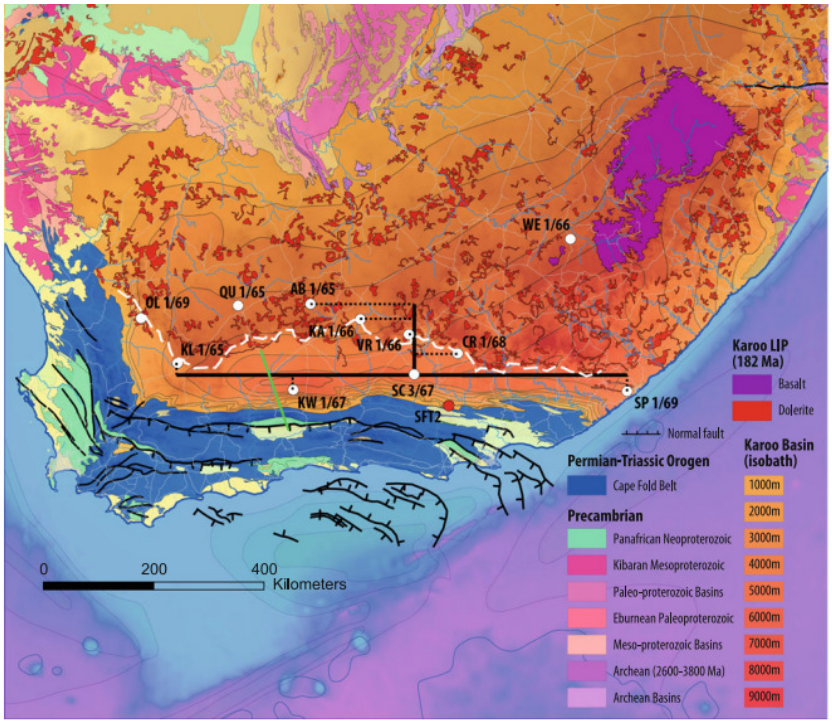

Figure 2.2: The geo-tectonic map of the Cape-Karoo region of southern Africa, with the locations of the examined deep boreholes (shown as white dots) and correlation profiles (shown as black lines). The Great Escarpment is also demarcated by the broken white line that runs around its perimeter. LIP (Large Igneous Province) (Linol et al., 2016).

The dolerite content is limited alongside the southern boundary of the Karoo Basin. The sills at shallower stratigraphic levels are generally saucer-shaped or ring-shaped and are found in the Beaufort Group at high stratigraphic levels (5 - 30 km in diameter and vertical extent of several hundred meters). Deeper sills in the east and west can extend for over 50 km. The well closest to our seismic line RT480 is well WE1/66. It has a depth of 1532 m and is located approximately 40 km away from the center of the seismic line (Scheiber-Enslin et al., 2021).

Table 2.1 shows the petrophysical properties of WE1/166. The depth values are assumed from Rowsell (1976) and have been converted to meters based on British feet. The density values are obtained from the Atlas of the Council for Geoscience Petrophysical Properties. The P-wave velocity values are obtained from a recent KARIN (Karoo Research Initiative) core acquired in the basin (Coetzee, 2018).

Table 2.1: Petrophysical properties of WE 1/66.

Stratigraphy	**Stratigraphic Boundary**	**Simplified Lithology**	**Depth (m)**	**Density Samples**	**Density (kg/m^3)**	**P-wave Velocity (m/s)**
		Dolerite		29	2964	5712
Beaufort Group	Moltano Formation	Sandstone	0	5	2438	4256
	Upper Beaufort	Sandstone	47	223	2478	4956
	Lower Beaufort	Predominantly Silstone	1119	223	2478	4200
Ecca Group	Upper Ecca	Shale	2429	21	2578	5131
	Lower Ecca	Carbonaceous Black Shale	3491	10	2111	4000
Dwyka Group		Tillite	3697	23	6242	5325
Natal Basement		Biotite Gneiss	3732		2700	4600
Total Depth			3785.6			

3. Theoretical Background and Literature Review

3.1 Seismic Technique

The study of naturally occurring earthquakes marked the beginning of seismology. Initially, seismologists were driven by the desire to understand the devastating power of strong earthquakes. However, it was not long before they discovered that the seismic waves generated by these events contained significant information about the Earth's internal composition. Analyzing these seismic waves forms the foundation for our current understanding of the Earth's core, crust, and mantle. Thus, seismology has emerged as a crucial branch of geophysics—the physics of the Earth (Sheriff and Geldart, 1995, p. 3; Evans, 1997, p. 2).

It was also discovered that artificial seismic waves, similar but significantly weaker, could probe the Earth's shallow structures, aiding in the search for minerals, water, and hydrocarbon deposits. Consequently, seismologists working in this area came to be known as exploration geophysicists, reflecting the growth of the seismic exploration industry (Sheriff and Geldart, 1995, p. 3; Evans, 1997, p. 2). With the use of advanced seismic technology, it has become feasible to identify sites designated for waste disposal, evaluate the stability of the soil beneath planned industrial undertakings, and conduct archaeological research.

The foundation for seismic exploration is straightforward. Sound waves, which are also referred to as acoustic waves, generate artificial seismic waves that have a frequency range of approximately 5 Hz to slightly above 100 Hz. Echoes (or reflections) flow outwards onto the surface when these sound waves descend into the Earth and interact with changes in the geological layers (Yilmaz, 2001, p. 26; Rost and Thomas, 2002). The modifiable factors, particularly velocity, density, and elastic moduli, might result in a contrast in the geophysical properties, which produces a geophysical anomaly that can be measured

when surveying takes place. Refraction and reflection seismic are the two distinct survey experiments used in practice to describe seismic procedures. Refraction seismic is a method guided by the principles of refraction seismology. In contrast, reflection seismic is a method that is governed by the principles of reflection seismology (Evans, 1997, p. 2, Sheriff, 2002, p. 116).

Reflection seismology primarily focuses on understanding intricate subsurface structures using variations in elastic properties across geological formations separated by boundaries. The study is primarily focused on the reflection of ground motion off geological limits in the subsurface, and the foundation of the reflection experiments is established by the duration and energy of the arrivals following the initial ground motion (Telford et al., 1990, p. 138). The analysis of reflection seismic data, with a focus on the amplitude and shape of the ground motion, may also provide information about the subsurface (Telford et al., 1990, p. 138; Sheriff and Geldart, 1995, p. 14).

On the other hand, refraction seismology operates in a method that ignores all subsequent ground movements and bases its refraction tests on the arrival times of the initial ground motion produced by a seismic source (Telford et al., 1990, p. 209). Because of this, seismic data from refraction tests are produced in the form of a series of durations versus distances, which may be used to calculate the depths of subsurface interfaces and the speeds at which motion spreads across the layers of the subsurface.

Land Seismic Data Acquisition

Figure 3.1 shows a common method of conducting a seismic survey that involves generating a seismic wave by detonating an energy source on the surface of the desired location, which results in a shock wave traveling down into the underlying rock layers (Telford et al., 1990, p. 186). Some of the energy from the shock wave is reflected back to the surface of the Earth due to acoustic impedance contrast between rock boundaries.

The geophones convert ground movement or vibration into voltage, by producing an electrical current when the ground vibrates due to seismic propagation. In the past, wires carried this signal to a recording truck, which is converted to digital form and written into a hard disk or an advanced magnetic tape. The information can then be transferred to a computer so that the geophysicists can process its content (Evans, 1997, p. 48).

However, the acquisition of seismic data has evolved drastically over the past years. It is now possible to collect and store seismic data remotely without the use of wired connections (Yin et al., 2020). One way to accomplish this is by arranging a group of geophones in a specific geometric formation and using them to conduct a seismic survey. Modern electronic advancements have led to the development of a single seismic recording equipment known as a "node" that is fully cable-free (Xue et al., 2016; Makama et al., 2021).

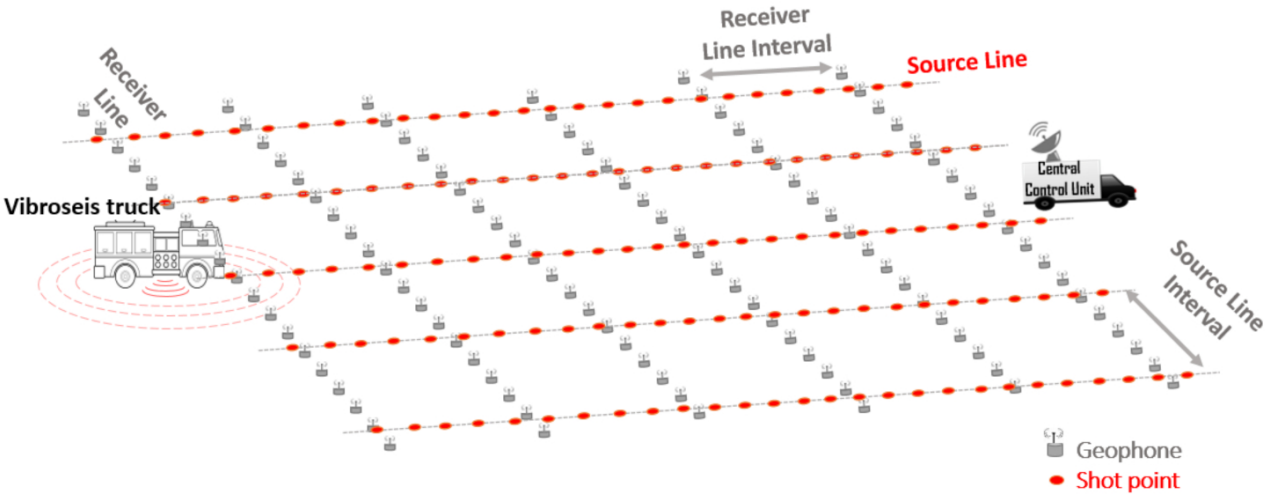

Figure 3.1: Seismic design showing how a wireless or nodal system can be used to acquire the land seismic data (Makama et al., 2021).

Shot locations refer to the sites where the energy sources are set off. In the conventional approach, the energy-receiving geophones are set up in a row at succeeding locations, and electrical cables connect the geophones to the recording truck. The line foreman and the recording truck operator, who serves as the observer, plan the staff's installation and the repossession of the receivers. Each day, a seismic group or team led by a party manager records seismic profiles covering several kilometers or miles in length.

Before the recording process begins, a team consisting of a surveyor and workers is employed to survey the line and determine the precise position of each station. The survey team then places wooden pegs at these stations to indicate the location of the seismic line or seismic segment that is to be captured. If there is a need for shot holes, it may be necessary to have a team of people who specialize in drilling (Evans, 1997, p. 42 - 43; Schmelzbach et al., 2005).

The electrical output signal from a geophone is represented by each trace in a shot

record, which is a visual representation of the data that are received (Makama et al., 2021). A land shot record is shown with 154 channels (Figure 3.2 (a)). The frequency spectrum graph of the short record is shown in Figure 3.2 (b). The records are stored in the chronological sequence in which they were recorded. When looking at a single shot record, it can be observed that the record's horizontal axis shows traces from all channels from that particular shot location and its vertical axis shows two-way traveltime. The term "seismic camera" originates from the early days of seismic technology when images were recorded on film, developed in a darkroom, and dried like typical photographs, resulting in the display that is observed today (Evans, 1997, p. 48).

These seismic shot records may be used to determine the speed of propagation into the ground, as well as the presence (or absence) of other seismic phenomena such as noise, reflection, and refraction. The classification of the type of rock present is determined by the velocity of sound within a layer of rock. To determine the speed of a straight movement, you can divide the distance covered by the time taken to cover that distance. Since events of reflection don't move in a straight line, the connection between their velocities, times, and offsets is more convoluted (Malehmir et al., 2018). The procedures followed to plan and implement a seismic survey will be discussed in later sections.

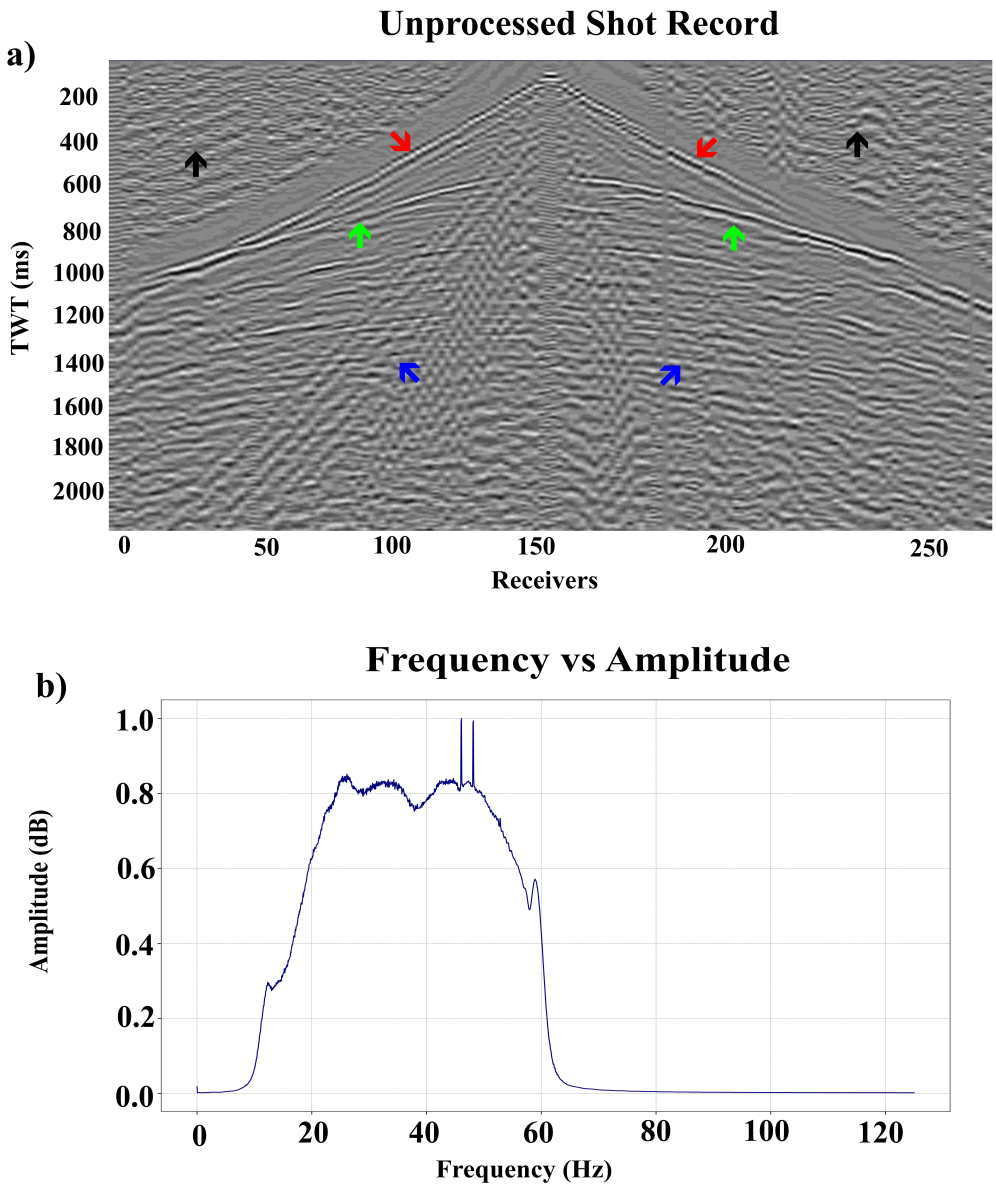

Figure 3.2: (a) Seismic shot record taken from the data reprocessed in this study. One can observe some of the most common types of seismic waves such as primary waves (red arrows), ground rolls (blue arrows), and hyperbolic reflections (green arrows). This shot record has high-frequency signals caused by electrical noise (black arrows). (b) Frequency spectrum graph of the shot record. The spikes present approximately between 45 Hz and 50 Hz are most likely caused by background noise in the shot record as well as electrical noise such as power line signals.

3.2 Seismic Prospecting

3.2.1 Different Types of Seismic Waves

Assuming the Earth has the elastic characteristics of a solid is a good starting point for describing how seismic waves travel through the Earth (Kiran, 2005). Since the crust (the planet's outermost layer) is elastic everywhere except the immediate location of the shot, this kind of wave transmission is called elastic propagation. A wide variety of wave actions may occur in an elastic solid. The movements of the solid's constituent particles during the passage of a seismic wave are utilized to classify the different behaviors exhibited by the wave's motion (Al-Sadi, 1980, p. 56).

Compressional Waves (P-waves)

When a seismic source is shot on a surface, a compressional force is generated and causes a reduction in the volume of the material or surface where the force is exerted. The elastic property of the rocks then causes an expansion of a rebound, accompanied by a dilation force, as depicted in Figure 3.3 (a). The resulting compressional wave or P-wave forms part of the response of the medium (Ellis and Stöckhert, 2004). The direction of the wave propagation is in the same direction of motion of all particles in the medium. Additionally, the velocity of this wave is given as a function of the density and rigidity of the medium. The velocity can be between 2500 and 7000 m/s for dense rocks and 300 to 500 m/s for spongy sand rocks (Kiran, 2005). The velocity of compressional waves is given by Equation 3.1:

$$v_p = \sqrt{\frac{\lambda + 2\mu}{\rho}} \tag{3.1}$$

The medium through which a wave travels is characterized by its density ρ, shear modulus represented by μ, and the first Lame parameter represented by λ.

Shear Waves / Secondary waves (S-waves)

This stress occurs when a lateral force is applied to a material. The resulting wave—referred to as a shear wave—propagates perpendicular to the applied force, as depicted in Figure 3.3 (b). In a shear wave, particle motion is orthogonal to the wave's direction of travel. The shear wave's velocity is determined by the material's resistance to shear stress, and it is typically about half the velocity of compressional waves in the same medium. Liquids like water cannot support shear waves, as they do not sustain shear strain or stress (Al-Sadi, 1980, p. 57; Onajite, 2013). The velocity of shear waves is given by Equation 3.2, where μ is the shear modulus and ρ is the density of the medium.

$$V_s = \sqrt{\frac{\mu}{\rho}} \tag{3.2}$$

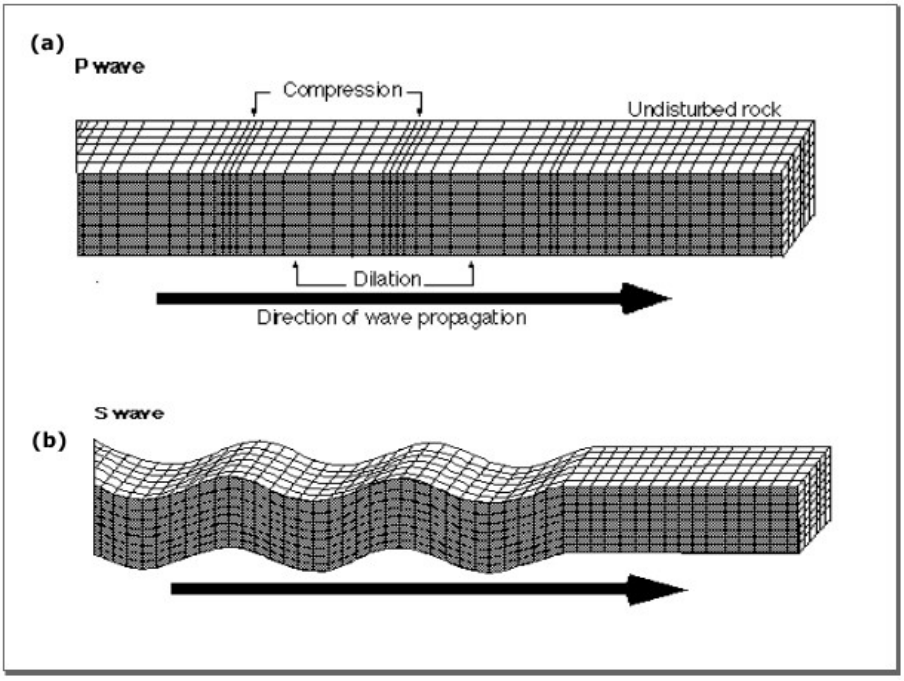

Figure 3.3: (a) General trend for the propagation of compressional waves (P-waves) in a solid medium. (b) General propagation of shear waves (S-waves) in a solid medium (Bolt, 1978).

Love Waves

Love waves are surface waves with a lateral motion that is at right angles to the direction of travel without observed vertical motion (Al-Sadi, 1980, p. 59; Kiran, 2005). Several noisy signals can appear throughout the seismic data if love waves undergo mode conversion, resulting in obscured reflected energy content. Figure 3.4 (a) gives a visual representation of Love wave propagation.

Raleigh Waves

These waves represent a kind of seismic surface waves that propagate along the surface of a semi-infinite medium. Figure 3.4 (b) shows an example of a secondary wave propagation. Rayleigh waves naturally have low frequency and propagate with a retrograde elliptical motion away from the shot position. When these waves reach higher depths, their particle motion causes a reduction in amplitude, which leads to a reversed direction in due course. These waves are commonly known as ground rolls because the movement of the ground looks like a rolling motion (Al-Sadi, 1980, p. 58).

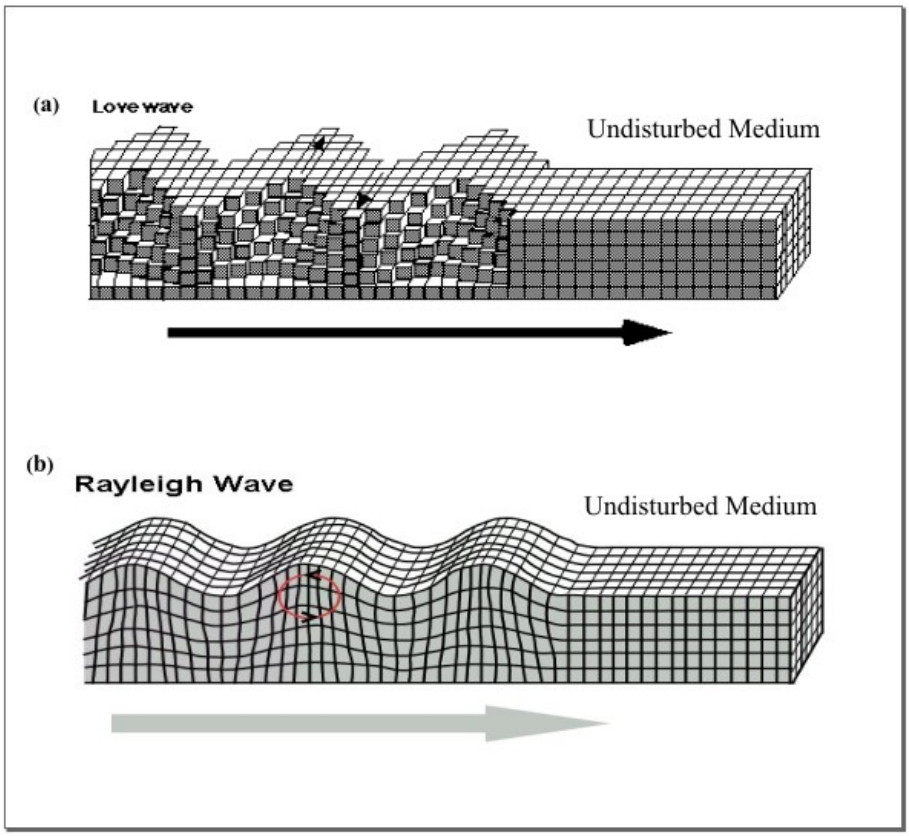

Figure 3.4: (a) Propagation of Love waves. The waves propagate in the same direction as the motion of the particles that make up the medium. (b) Propagation of Raleigh Waves (also known as ground rolls.). These waves propagate at a right angle to the direction of motion of the particles that make up the medium (Bolt, 1978).

Air waves

Air waves, also known as air blasts, are generated when the source is activated on land, which sets up an air-coupled wave - a secondary wavefront in the surface layer. This wave mostly propagates slower than a compressional wave by about 350 m/s, and its speed depends predominantly on humidity and temperature (Al-Sadi, 1980, p. 57; Sheriff and Geldart, 1995, p. 53; Kiran, 2005). Equations 3.3 and 3.4 demonstrate the velocity (v) of airwave:

$$v = 1051 + 1.1Fft/sec \tag{3.3}$$

where F = Fahrenheit temperature

$$v = 331.5 + 0.607Cm/sec \tag{3.4}$$

where C = Celsius temperature.

Mode-Converted Waves

When seismic energy encounters a geological boundary, some of the energy is reflected back to the surface, and the remainder is transmitted through. Depending on the elastic properties of the boundary, the incident wave whether primary or secondary may convert to the other type of waves or result in a mix of different types of waves. These conversion processes can sometimes diminish the signal-to-noise ratio, posing challenges in seismic data processing (Sheriff and Geldart, 1995, p. 52; Kiran, 2005).

Direct and Head Waves

The direct or head wave is observed as the growing energy wave propagating along the surface away from the source position. It possesses the same velocity as the stratigraphic layer through which it propagates. These energy fields are parts of the primary wavefront that are transferred down to the bottom of the weathering layer and are refracted along the base of the layer (Sheriff and Geldart, 1995, p. 50). They come back to the surface as refracted waves. In some cases, the transmission velocity in the surface layer is lower than the velocity of the refracted energy. Before the direct waves arrive in this instance, refracted head waves appear in the mid-to-far offset traces (Al-Sadi, 1980, p.59).

Guided Waves

A wave propagating along a layer with extreme velocity or density difference at its upper and lower limits can undergo internal reflection, meaning it stays within the layer, bouncing between the layer's upper and lower interface. This kind of wave is called a guided wave and mostly has a vertical motion of particles in the medium. These waves appear as short waves with a recurring pattern on shot records (Kiran, 2005).

3.2.2 Properties of Seismic Events

Reflections

In seismic terminology, "reflection" refers to an occurrence where a wave generated by a seismic source rebounds off a surface with a contrasting acoustic impedance, such as a reflector interface or a layer with multiple contrasts, beneath the Earth's surface (McQuillin et al., 1984), as shown in Figure 3.5. The characteristics of the acoustic properties on either side of a discontinuity in the reflector medium determine the polarity and amplitude of reflections (Malehmir et al., 2018). The product of velocity and density gives acoustic impedance. Moreover, the relation amongst amplitude of the incident ray A_i, reflected amplitude A_r, and reflection coefficient R_c is given by Equation 3.5 (Onajite, 2013).

$$A_r = R_c A_i \tag{3.5}$$

Equation 3.6 is an expression for the coefficient of reflection where p_1, p_2 represent the density values of the two layers and v_1, v_2 represent the velocities (primary or secondary wave velocities) of the respective layers.

$$R_c = \frac{(p_2 v_2 - p_1 v_1)}{(p_2 v_2 + p_1 v_1)} \tag{3.6}$$

When velocity is constant, it means that reflection can be caused by density contrast. This means that any sudden difference in acoustic impedance prompts reflection. All non-reflected energy gets transmitted to the next medium. When the reflection coefficient R_c is large, less transmission happens, leading to a reduction in the signal-to-noise ratio below the interface (Kiran, 2005).

Refractions

Refraction is the phenomenon where the direction of a seismic ray alters as it passes through a medium with differing velocity, as illustrated in Figure 3.5. This is explained by Snell's law of refraction, which states that the ratio of the sines of the angles of incidence and refraction is equal to the ratio of the seismic wave velocities in the two media, or alternatively, their refractive indices. Snell's law applies to all possible angles of incidence and refraction for any given pair of media (Kiran, 2005; Born and Wolf, 2013). Equation 3.7 describes this process.

$$Sin(\frac{i}{v_1}) = Sin(\frac{r}{v_2}) \tag{3.7}$$

Where i is the angle of incidence, v_1 is the velocity of the incidence layer, r is the angle of refraction, and v_2 is the velocity of the refracting layer.

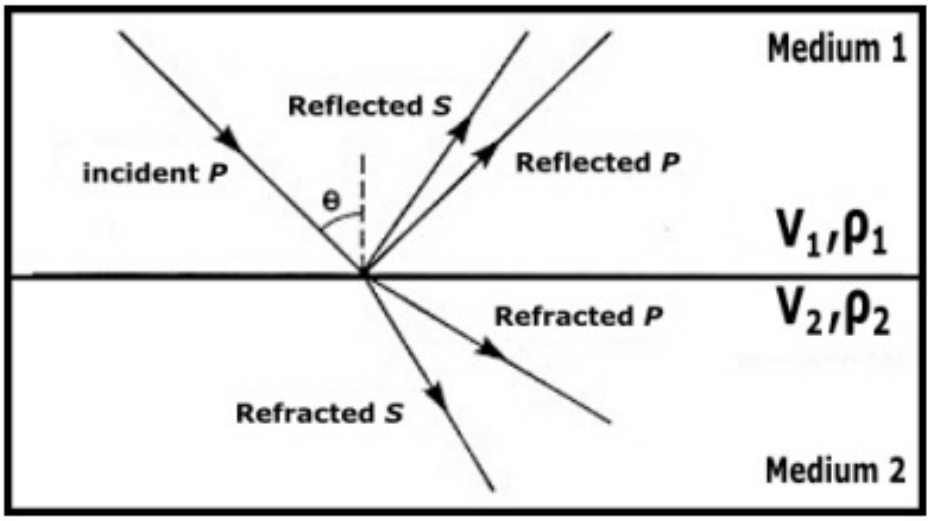

Figure 3.5: The rays produced when a P-ray makes an oblique impact on a geological boundary that separates two media with distinct seismic velocity and densities. In this context, P denotes primary waves, and S signifies secondary waves. Additionally, V is the velocity of either primary or secondary waves, and ρ indicates the density of the respective layer (Kiran, 2005).

Multiples

A seismic wave that has been reflected several times is known as a multiple, i.e., more than once. The significant difference between short-path and long-path multiples is that short-path multiples arrive soon after the primary waves and change their wave shape, whereas long-path multiples arrive as a unique event (Makama et al., 2021).

3.2.3 Seismic Noise

Incoherent Noise

This form of high-frequency noise is mostly referred to as random noise. It is unpredictable and has specific statistical properties. The causes of incoherent noise include wave scattering by asymmetric near-surface features and large structures such as boulders. Small-scale faults also contribute to the introduction of scattering (Kiran, 2005).

Coherent Noise

Coherent noise consists of surface waves, refractions introduced by high-velocity media, reflections from near-surface geological features such as buried stream channels and faults, noise introduced by external sources such as moving vehicles or mine activities, multiples, and other related sources. Most of these propagate horizontally, and noise from moving vehicles is repeatable on consecutive shots. Coherent noise can be further divided into

energy that reaches the spared almost vertically and one that propagates horizontally (Sheriff and Geldart, 1995, p. 253; Kiran, 2005).

3.3 Field Equipment for Seismic Exploration

3.3.1 Seismic Sources

When conducting seismic surveys, choosing an energy source suitable for the target is one of the significant decisions geophysicists make. This is so because the signal-to-noise ration (S/N) and resolution are influenced by the characteristics of the source (Sheriff and Geldart, 1995, 198). There are referential criteria that can be used when selecting a source. Firstly, knowing the objectives of exploration is crucial. One must select a source with enough energy to cover the horizons of the target. Secondly, it is vital to know the bandwidth for the resolution desired. This means deciding if high reflection resolutions are needed for subtle features and picking a source that generates a vast range of frequencies (Al-Sadi, 1980, p. 149).

In the case of shallow targets, the source may have enough frequency bandwidth and energy. When investigating deeper events, a long travel path towards a deep reflector demands one to select a source with adequate energy and high frequencies to sustain a vast bandwidth of reflection (Kiran, 2005). Moreover, understanding the signal-to-noise ratio (S/N) characteristics is crucial because there are different noise problems in different areas. They also have the potential to influence the source selection process. The environment is also a contributing factor since geophysicists must follow special safety precautions if the area is populated. Lastly, source selection also depends on cost and availability since the arrival time of the crew is essential. There are two categories of land seismic energy sources, explosive and non-explosive seismic energy sources (Evans, 1997, p. 31).

3.3.2 Vibroseis

In 1966, Conoco Inc used a particular vehicle called a vibrator to conduct the first experiments using the vibroseis method. Mechanically, the vibrator is a tool that rides on a vehicle. To create a source array, a number of trucks can be lined together in a row (Evans, 1997, p. 141). The average vibratory truck is as big as a trash truck and may weigh up to 50 tons. In addition to being mobile on public highways, these vehicles often have independent wheel drive, allowing for navigation over almost any terrain. Vibroseis is widely used because of the low operational cost of vibrators compared to other strong energy sources. It is true that the Gas Exploder, sometimes known as a gas cannon, is

the cheapest option, but its output is far weaker than that of a vibrator (Chapman et al., 1981). Figure 3.6 portrays a typical vibroseis truck used in seismic exploration projects.



Figure 3.6: An example of the vibroseis truck in the field (Fathi et al., 2016).

According to Chapman et al. (1981), as the demand for hydrocarbons continued to rise and the availability of massive reservoirs declined, more attention had to be paid to the search and development of stratigraphic reservoirs. Exploring these reservoirs effectively demands pushing current exploration methods to their resolution limits. The field of reflection seismology may benefit significantly from this. To characterize stratigraphic reservoirs with greater precision and better resolution, the performance of the whole seismic system must be evaluated and enhanced wherever limitations occur. Basic restrictions in data collecting, processing, and interpretation could exist, necessitating development in all three areas (Kiran, 2005).

A vibrator's base plate is powered by a continuous, sinusoidal-like signal with varying frequencies. The signal's frequency at any given moment is included within the seismic range. For this reason, the driving signal is sometimes referred to as a "sweep" since its changing frequency moves throughout the seismic spectrum. An upsweep is a frequency sweep that moves from low to high frequencies. A down sweep refers to a frequency sweep that goes from high frequency to low frequency (Fathi et al., 2016).

In order to shift the base plate at the correct frequency, a driving force is required.

This plate is propelled by hydraulic pistons that apply a substantial load known as the reaction mass (Chapman et al., 1981). A sweep generator regulates the motion of the hydraulic pistons. The vibrator truck serves as the mounting point for the whole hydraulic setup, the reaction mass, and the base plate. To guarantee that the signal being delivered into the ground is the intended sweep signal, a sensor such as a receiver is put on the base plate. An electrical output signal is generated by this sensor and may be compared to the intended sweep signal. This electrical feedback loop maintains the transmitted signal the same as the sweep signal (Evans, 1997, p. 143).

The correlation procedure is used to reassemble the reflection series from the geophones' recorded signal. As soon as the recording begins, a pilot trace is saved in the electronic correlator unit of the recording truck (Chapman et al., 1981). When a signal is received, it is recorded in a memory device and compared to the pilot's trace. The correlated trace is the recorded result of the correlation procedure. Each of these traces is a piece of the associated field record that may be thought of as an analog to a dynamite shot gather. The sweep time is how long the vibrator sweeps at a given point. The receiver's output is recorded in the memory for the duration of the sweep and any additional time that must elapse to achieve the specified record length (Fathi et al., 2016).

3.3.3 Seismic Receivers

Geophones

Modern-day seismic receivers operate using the rules of Faraday's law of electromagnetism (Ben-Menahem, 2012). The two kinds of extensively utilized geophones are the moving magnet and moving coil geophones. The requisite components to construct seismic geophones are a conductor, a permanent magnet, and a spring that is used to position the permanent magnet in the electric field for the case of a moving magnet geophone or the conductor in the magnetic field for the case of a moving coil geophone. Figure 3.7 (a) shows an example of a geophone while Figure 3.7 (b) shows its internal components (Kiran, 2005).

The conductor is normally a copper wire that has been wrapped into a coil with a cylindrical shape. It is alternatively referred to as the element. The motion of the coil or the conductor through the electrical or magnetic field leads to the induction of electromotive force (EMF), as stated by Faraday's law. Therefore these kinds of receivers are called velocity geophones (Yin et al., 2020). Damping is often used on geophones in order to reduce oscillations, which might ultimately result in a loss of resolution. When first developed, this function was accomplished by submerging the moving portion in oil. Eddy

currents are often used these days in order to dampen geophones. In most circumstances, the level of damping is controlled by an appropriate resistor shunt connected across the geophone terminal (Al-Sadi, 1980, p. 152).

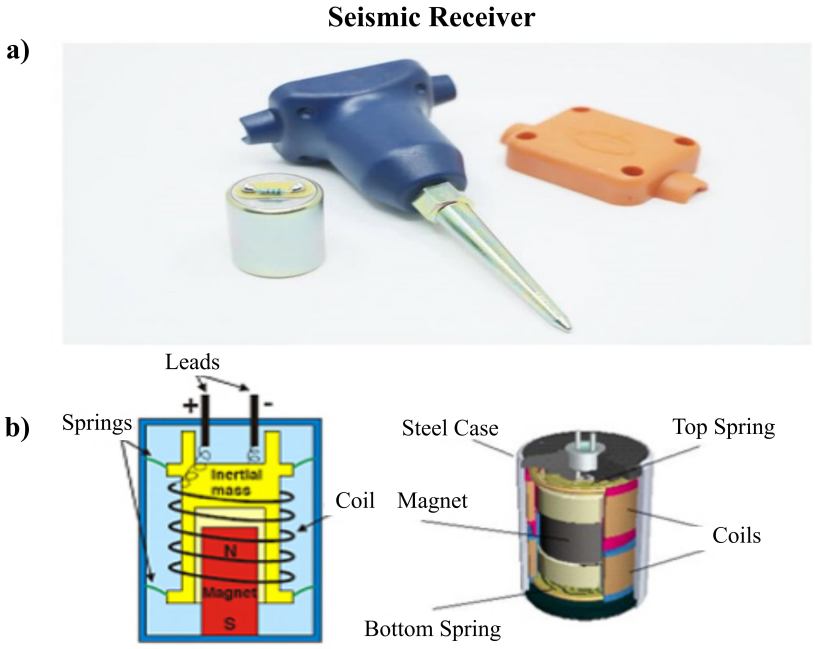

Figure 3.7: An example of a geophone (a) and its internal components (b) (Spain et al., 1991).

Nodes

According to Makama et al. (2021), a node refers to a self-contained equipment that comes with various components such as batteries, an analog-to-digital converter (ADC), a processing unit, filters, memory, a clock for accurate timing, transceivers, an internal geophone sensor (GP), and an external port for linking to a group of geophones (Figure 3.8). Once the survey is set up using the nodes and geophones, the source is used to produce vibrations at each shot location. This energy signal is then sensed by the geophones and transmitted through an amplifier and ADC for digitization (Spain et al., 1991). The stored data in each node can be harvested after the survey using specialized software so that it can be processed for interpretation.

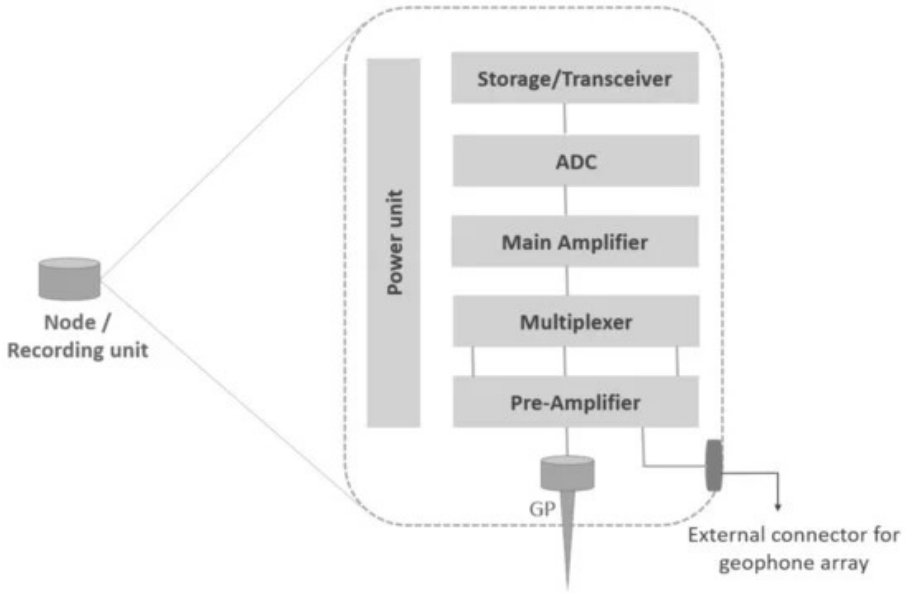

Figure 3.8: Internal components of a node and the way in which the connections are configured electrically (Makama et al., 2021).

3.4 Two Dimensional Survey Design

When planning a seismic survey, the most crucial principle to keep in mind is how can the desired target be imaged in the most effective way for both time and financial cost. The starting survey design factors include the variables of resolution, like the amount of wave frequency needed to map the target. Moreover, it is crucial to determine other horizon-related information to account for interpretations. Some of the parameters required for a successful survey are the near-surface layer velocities, the shallow layer's velocity, the target layer, the group interval, the Frenzel Zone, far offset, recording length, and group interval. These parameters are discussed in detail below (Sheriff and Geldart, 1995, p. 191; Kiran, 2005).

3.4.1 The Near-surface Layer

The speed of this particular layer is crucial in determining offsets and understanding the effects of ground roll (Sheriff and Geldart, 1995, p. 193). The weathering layer mostly has low velocity, mainly because of its exposure leading to erosion. This layer can be significantly complex, and its different layers can have distinct velocities (Kiran, 2005). The maximum dip and velocity of all layers are initial parameters; more information can be derived from existing seismic data or well logs from the area.

3.4.2 The Shallow Layer

The shallow layer is an important layer that can aid interpretation. The velocity of the layer, v_s, and the approximate arrival time are the desired parameters as they allow us to compute the depth of the layer, Z_s using a distance formula as follows. In Equation 3.8, t, is the two-way travel time to the shallow layer (Al-Sadi, 1980, p. 138; Kiran, 2005). Moreover, it provides information required to determine near offset, i.e., $X_{near} < Z_s$.

$$Z_s = 0.5(tv_s) \tag{3.8}$$

3.4.3 The Target Layer

This is the layer that the survey seeks to investigate primarily. Adequate knowledge of geological features such as dip and thickness of this layer is needed to determine the required frequency range for imaging this horizon (Sheriff, 2002, p. 187; Kiran, 2005). The requirements of this layer must be prioritised when conflicts between parameters arise as it is safer to compromise them over the target.

3.4.4 Group Interval

This is a sampling interval that is used on the surface. It represents the distance between receivers on the ground, and it is determined after careful consideration of one that prevents unwanted effects of aliasing (Al-Sadi, 1980, p. 140). It is given by Equation 3.9, where v_{min} is the minimum velocity, F_{max} represents the expected maximum frequency, and θ represents the angle of the maximum dip of the target horizon in degrees.

$$G = \frac{1}{2}(\frac{v_{min}}{F_{max}})Sin\theta \tag{3.9}$$

3.4.5 The Fresnel Zone

According to Kiran (2005), the Fresnel zone is the smallest section of a reflector that makes up a clear image of an individual event that is elliptical with offset and circular at zero offsets (Figure 3.9). The radius of this zone is determined based on the horizontal distance covered by a seismic wave after traveling a quarter of its wavelength from the reflector. This distance is calculated using Equation 3.10, where λ represents the wavelength, v_θ is the wave-front velocity or phase velocity, and θ is the phase angle (Xu and Stovas, 2018).

$$\lambda = v\theta f \tag{3.10}$$

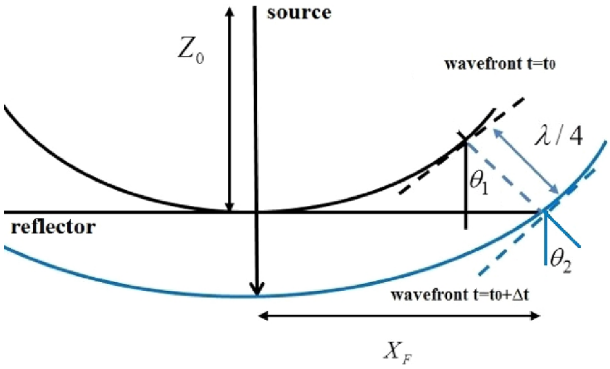

Figure 3.9: The Fresnel zone within a medium that is not uniform in all directions (anisotropic medium). The phase angles θ_1 and θ_2 are measured at specific points on wavefronts occurring at two different times: $t = t0$ and $t = t_0 + \Delta t$ (Xu and Stovas, 2018).

3.4.6 The Far Offset

This parameter has to be calculated in advance for the target and deep horizon, in that order. It is a function of the depth derived using the velocity field (Kiran, 2005). Upon computing the maximum offset, the velocity of the layer on the surface is involved. Once this is computed with the help of group interval, other parameters can be analyzed within the scope of equipment used. Equation 3.11 can be used to calculate the maximum offset, where Z represents the depth of the horizon, v_s represents the velocity of the surface layer, and v is the average velocity of seismic waves to reach the target (Yin et al., 2020).

$$H_{max} = (\frac{1}{2})(Z)(\frac{v + v_s}{v - v_s})^{0.5} \tag{3.11}$$

The above equation can be modified for a dipping reflector by extending H_{mas} using Equation 3.12, where Z represents the depth of the dipping horizon and θ is the dip angle of the horizon under consideration (Kiran, 2005).

$$dx = Ztan(\theta) \tag{3.12}$$

3.4.7 The Recording Length

The length of recording is expressed as a function of the velocity and depth of the deepest horizon and is determined as part of the survey design (Sheriff and Geldart, 1995, p. 186; Kiran, 2005). It can be determined using Equation 3.13. The parameter T_d is the

maximum offset two-way travel time of the deepest horizon of interest, T_r is the desired record length, and L is the length of the most extended processing filter.

$$T_r = T_d + 2L \tag{3.13}$$

The filter length is usually sufficient at 200 milliseconds. The additional time required for recording is weighed against any potential advantages from data from very deep horizons. When the source is vibratory in nature, the signal duration becomes more significant (Kiran, 2005). Migration should also be taken into consideration.

3.4.8 The Sampling Rate

Depending on the level of resolution required, the sample rate in time ranges from 2 to 4 ms, which is more or less normal (Sheriff and Geldart, 1995, p. 188). Equation 3.14 allows us to estimate this parameter. Most seismic surveys have a sampling rate of 2 ms.

$$SamplingRate = \frac{0.5}{maximumexpectedfrequency} \tag{3.14}$$

3.4.9 The Group Interval

The group interval achievable with a certain recording device is determined by Equation 3.15, where H_{max} is the far offset, H_{min} is the near offset, and N.C. is the total number of available channels for the recording process (Kiran, 2005).

$$GroupInterval = \frac{H_{max} - H_{min}}{NC - 1} \tag{3.15}$$

3.4.10 The Fold Coverage

Each source location contributes to a specific extent of subsurface coverage. For uniform geological layers, the point being sampled, commonly referred to as the midpoint, is equidistant from the source and receiver. The interval at which the subsurface is sampled is half the distance of the coverage interval on the surface. The term 'fold' describes how often a particular subsurface point, known as the Common Midpoint (CMP), is surveyed by different combinations of source and receiver positions (Yilmaz, 2001, p. 42). This parameter is given by Equation 3.16, where S is the number of group interval units inside the source spacing and NC is the number of accessible channels.

$$F_c = \frac{NC}{2S} \tag{3.16}$$

3.4.11 Interval of the Source

Source interval refers to the distance between multiple source locations. It is determined by the required fold coverage and the available channel count. The expression Equation 3.17 for this parameter is as follows, where F represents the fold and N.C. is the number of accessible channels (Xue et al., 2016).

$$S_{interval} = \frac{NC}{2F} \tag{3.17}$$

3.4.12 The Position and Orientation of Line(s)

The geometry of the seismic survey is not independent of its primary objective. Position, direction, and extent of the seismic profiles are crucial survey design concerns (Evans, 1997, p. 187). Firstly, when feasible, the lines must be orthogonal to the fault planes because the fault plane is most clearly defined on the seismogram when the lines are orthogonal to it. Secondly, relationships between lines are crucial to the interpretation of the data. In cases when there is already seismic data in the area, additional lines are designed so that they may be tied in. Being connected to a well log is a great asset. If the line can be brought closer to the well, then the seismic data can be more directly linked to the well log. Moreover, lines should be designed to reduce height and topographical concerns where doing so does not conflict with other demands (Chapman et al., 1981; Kiran, 2005).

3.5 Theoretical Aspects of Processing Seismic Data

3.5.1 Demultiplexing

Multiplexed data formats are used to capture information from the field. As seen in Figure 3.10, the data must first be demultiplexed. Demultiplexing, from a mathematical perspective, is the process of transposing a large matrix such that the columns of the resultant matrix may be interpreted as seismic traces collected at various offsets using a single shot point (Yilmaz, 2001, p. 43). The data are transformed at this point into a format that can be easily utilized for the rest of the processing activities. The type of format used is dependent on the specific firm and its processing system. SEG-Y, created by the Society of Exploration Geophysicists, is a standard format for exchanging data in seismic exploration and is used in this study (Kiran, 2005).

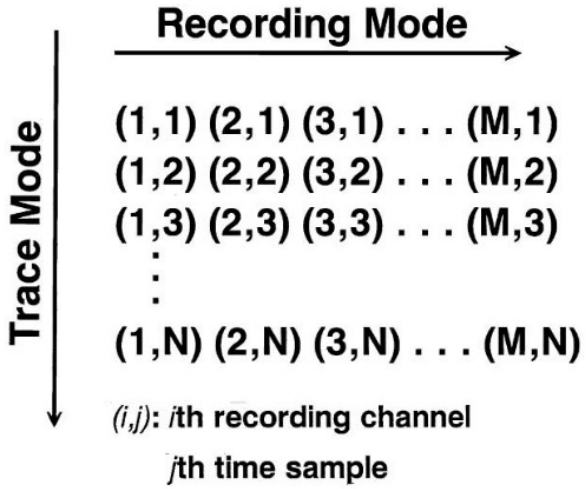

Figure 3.10: To capture seismic data, channels are sampled simultaneously through demultiplexing. In this case, the data are organized into columns of samples, with one channel's samples appearing first. The samples from the subsequent channels M and N represent the recording channel and the time sample, respectively (Yilmaz, 2001, p. 43).

3.5.2 Preprocessing

In this phase, a procedure known as "data cleaning" is used to detect and fix any incorrect information in the raw data (data editing) (Al-Sadi, 1980, p. 162). At this point, the original amplitude and waveform of the signal are both recovered. In the preconditioning phase, trace editing and gain applications are used to clean up the data. The preprocessed data are then fed into the subsequent stages for further processing (Yilmaz, 2001, p. 40).

3.5.3 Creating CDPs - Crooked Line Binning

A CMP (Common Midpoint) or CDP (Common Depth Point) gather comprises seismic traces that have the same midpoint or depth point. While "CDP" and "CMP" are often used interchangeably, their application depends on the orientation of the reflectors. In conditions where reflectors lay flat and seismic velocities are uniform in every direction, CDP and CMP gathers are effectively the same. However, in the presence of angled subsurface reflectors, the gathers differ, necessitating the exclusive use of "CMP gather" in such scenarios (Yilmaz, 2001, p. 45). Figure 3.11 illustrates the difference between CMP and CDP for the horizontal (Figure 3.11 (a)) and dipping (Figure 3.11 (b)) reflectors.

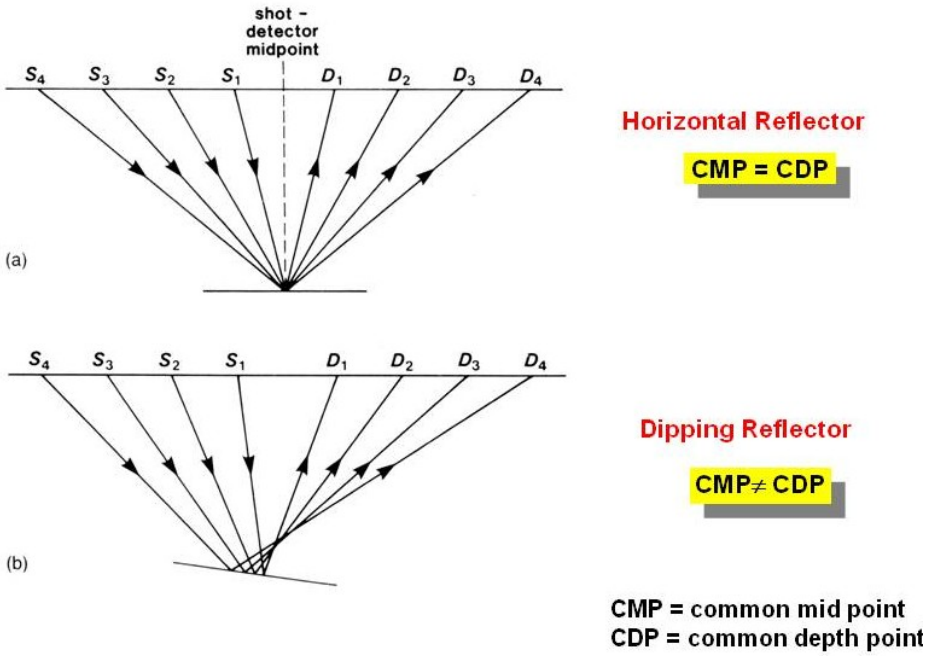

Figure 3.11: (a) These are the paths of rays linked with a horizontally level reflector that goes from the location of the shot (S) to multiple receivers (D). (b) Shows a possible common depth point (CDP) arrangement for a dipping reflector as seismic waves propagate from shot to receiver locations (Xue et al., 2016).

3.5.4 Floating Datum Static Corrections - Concept

According to Yilmaz (2001, p. 255), when processing data for an area with difficult terrain, one may want to use a floating datum instead of a fixed datum plane since the changes might be significant. After processing, the floating datum may be transformed into a fixed datum plane, which is a smoothed representation of the original terrain. In addition, the highest point of the survey is often used as the starting point for the fixed datum, since this is where the "time zero" on the final seismic sections will be located (Nguyen et al., 2015). The static time shifts $\delta\tau_{ij}$ to apply for a given source-receiver pair are given by Equation 3.18.

$$\delta\tau_{ij} = (z_j + z_i)(\frac{1}{v_b} - \frac{1}{v_w}) - \frac{1}{v_b}(E_{Tj} - E_{FDj} + E_{Ti} - E_{FDi}) \tag{3.18}$$

In this equation, E_{Tj} and E_{Ti} denote the elevations of the shot and receiver relative

to the actual topography, while z_j and z_i correspond to the weathering layer thicknesses at the shot and receiver points, measured from the floating datum. Additionally, E_{FDj} and E_{FDi} refer to the shot and receiver altitudes, respectively, defined with respect to the floating datum. To ensure the reflection times retain their hyperbolic shape, shots and receivers are repositioned to a floating datum that mimics the surface's topography instead of a flat datum. This adjustment allows for the CMP gather to be conducted along a datum that is locally level and approximates flatness within the spread's length (Yilmaz, 2001, p. 257; Onajite, 2013).

Seismic data frequently come with various topographical difficulties and need changes. By using elevation profile smoothing as a stand-in for the original topographic surface, floating datum static corrections can correct seismic data for topographic inaccuracies (Kiran, 2005). This datum is used to make a series of static shifts in the data, which are tracked by the surface's coordinates. To account for the potential errors introduced by variations in shot and receiver elevations, a datum correction was utilized.

3.5.5 Geometric Spreading

In wave propagation principles, the region that the wave energy covers expands as the wave travels away from the source, resulting in a reduction in wave intensity. This is known as "geometric spreading," which is frequency-independent and has a significant impact on wave propagation circumstances (Figure 3.12). Geometric spreading correction is applied to account for this loss when processing the seismic data.

The correction is a gain control method that is applied early in processing to compensate for wavefront divergence, a phenomenon that normally occurs when wavefront lose energy as they propagate through the rock medium (Al-Sadi, 1980, p. 65; Yilmaz, 2001, p. 61; Onajite, 2013). Shot records from the field represent a wavefield that is created by a sole shot. The shot is conceptually thought of as a point that creates a spherical wavefield. Divergence is a problem because according to Yilmaz (2001, p. 59), there are two effects that Earth has on wavefields that are propagating:

(a) Energy density decays and the decay of a homogeneous medium is proportionately given by $\frac{1}{r^2}$ where r represents the radius of the wavefront.

(b) As a signal travels from its source, its frequency content changes with time. The absorption of higher frequencies occurs more quickly than that of lower ones. This is because rocks naturally absorb sound.

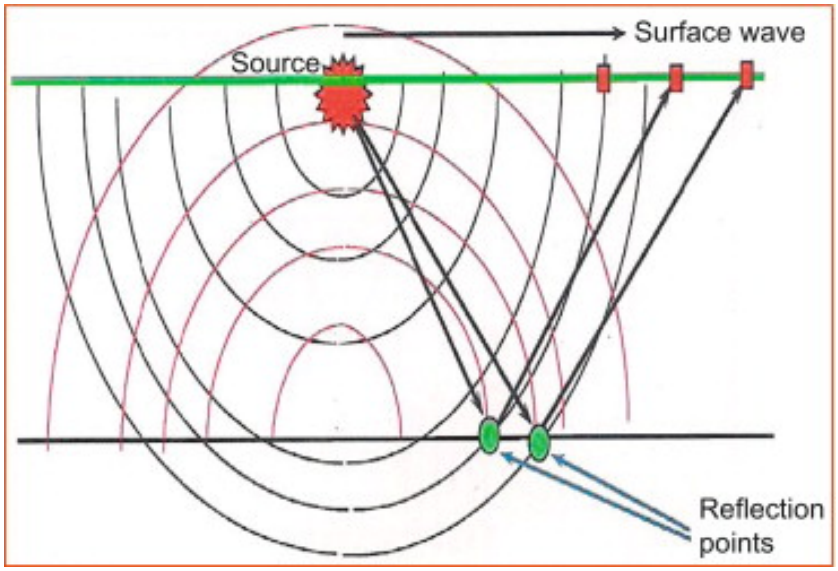

Figure 3.12: A schematic representation of geometric spreading of wavefronts. The frequency of the waves is reduced as the distance from the source increases and their respective wavelengths increase, therefore the geometric spreading correction must be applied to the data (Onajite, 2013).

3.5.6 Automatic Gain Control

The utilization of Automatic Gain Control (AGC) is instrumental in enhancing the clarity of seismic data, particularly when it has been compromised by factors such as attenuation or the effects of spherical spreading that lead to the reduction in amplitude. AGC can be incorporated at various points during the processing stages. Among the AGC techniques, the instantaneous variant is notably widespread. It begins by selecting a time gate, followed by computing the average absolute amplitude across the seismic trace (Wang et al., 2016).

Subsequently, a gain function is determined by calculating the ratio of the desired root-mean-squared (RMS) amplitude to the previously calculated average value. Unlike the RMS amplitude method of AGC, this particular value is assigned to each time sample within the time gate, for instance, to the nth sample in the trace. The process then moves the time gate forward by one sample and computes the value of the gain function for the subsequent $(n + 1)$ th sample, and this sequence continues. It is important to note that this method for defining the gain function obviates the need for interpolation (Yilmaz, 2001, p. 60; Onajite, 2013).

As a result, the central gate's scaling function g(t) can be defined as shown in (Equation

3.19), where N is the number of samples and x_i is the amplitude of the trace (Yilmaz, 2001, p. 89).

$$g(t) = \frac{DesiredRms}{\frac{1}{N}\sum_{i=1}^{N}|x_i|} \tag{3.19}$$

3.5.7 RMS Amplitude AGC

Another form of AGC is the RMS (Root Mean Square) amplitude automatic gain control function and it is determined by the root-mean-square amplitude of the input trace inside a certain time gate (Al-Sadi, 1980, p. 128). Equation 3.20 describes how to calculate this gain function. Each segment of the input seismic trace is split into gates that operate at a constant rate. To begin, the amplitude of every sample in a gate is squared. The second step is to get the average of these numbers and square it (Yilmaz, 2001, p. 86).

$$g(t) = \frac{DesiredRms}{\sqrt{\frac{1}{N}\sum_{n=1}^{N}x_i^2}} \tag{3.20}$$

Where N is the number of samples within the gate and x_i is the amplitude of a trace. In most cases, one can establish a baseline gate length at the trace's initial depth. A fixed gate length may be used, or the gate length can be systematically raised along the trace. In order to determine the value of the gain function at each gate center, one can use the formula given above. The g(t) function is interpolated between the gate midpoints. To reiterate, the time gates that were provided will not move along the trace; they will remain in place t (Yilmaz, 2001, p. 86; Wang et al., 2016). A balance module ensures that all trace amplitudes within the dataset have the same overall RMS amplitude level, allowing for a more straightforward comparison of findings. This method was not relied on in this research.

3.5.8 Noise Suppression

With pre-processing, three main goals need to be achieved: adjust for acquisition-related effects, smooth the data by getting rid of random noise, and get rid of any extraneous coherent energy that isn't being reflected (Sheriff and Geldart, 1995, p. 280). As a result, a lot clearer picture of the subsurface is obtained due to the improved ability to locate important seismic reflectors. Since the velocity fluctuations close to the surface are fixed, the indirect and refracted signals are now redundant. The intensity of these events might cause artifacts when using certain signal processing methods, hence first

break muting is usually conducted to get rid of the variations. Noise and interference may be reduced and the reflected signal improved by the use of digital filters. Numerous distinct varieties of filters are now in use. The frequency-wavenumber filter, often known as the F-k filter, is a popular filter that categorizes events according to their apparent frequencies. Seismic signal augmentation is greatly aided by the use of frequency filters and F-K filters (Yilmaz, 2001, p. 30).

Frequency-Wavenumber Filtering

Yilmaz (2001, p. 35) explains that dips in the $f-k$ (frequency-wavenumber) domain allow us to distinguish between linear events that are coherent in the $t-x$ (time-distance) domain. This permits us to filter out potentially unwanted energies. More specifically, fundamental reflections are often obscured in recorded data by coherent linear noise such as ground roll, guided waves, and side-scattered energy. The unwanted energy in this spectrum is pushed out by a fan, which effectively eliminates these energy types (Kiran, 2005). A reversal of the mapping to the $t-x$ domain follows.

The filtered record that is produced contains just the backscattered portion of the ground-roll energy. Implementations of $f-k$ dip filtering range from simple definitions of $f-k$ domain rejecting fans to more complex procedures. There are many noise reduction strategies at our disposal. This research uses the f-k domain filter that is included as a Claritas process module to handle the seismic line data. The f-k domain filter provides certain benefits over the traditional f-k dip filter, including the ability to fine-tune the filter's frequency and wavenumber of interest (Yilmaz, 2001, p. 41). $f-k$ filtering is done as follows:

(a) To begin, a 2-D Fourier transform was applied to a CDP (common depth point) sorted shot record.

(b) Following this, a 2-dimensional reject zone is established in the $f-k$ domain by turning off the $f-k$ filter's specter of phase and amplitude in that region.

(c) The 2-D $f-k$ filter is then applied by multiplying the input data set's magnitude spectrum by the filter's own.

(d) Finally, the filtered data are subjected to a 2-D inverse Fourier transform.

3.5.9 Pre-stack Deconvolution

Deconvolution is a technique that is carried out along the time axis to improve the temporal resolution of seismic wave traces (Yilmaz, 2001, p. 160). To accomplish this, the fundamental seismic wavelet is condensed into a nearly singular point while reducing any lingering echoes present in the field data (Mendel, 2013). The second use of deconvolution involves altering the form of the seismic wavelet by whitening it to give it more frequencies and a more distinct pulse (Al-Sadi, 1980; Idier and Goussard, 1993).

The difficulty with this approach is that the precision of the output data may not be obvious in some circumstances unless it is adequately contrasted with the input data. Deconvolution is usually applied pre-stack. However, it is a common practice to apply deconvolution to data that is already stacked. Deconvolution can eliminate a good portion of the multiple energy from a segment, in addition to wavelet compression (Idier and Goussard, 1993).

Moreover, predictive deconvolution is the utilization of knowledge from the early section of a seismic trace to forecast and deconvolve the later stages of that trace. The occurrence of reverberation and multiples are two examples of predictable recurrent noise (Egbai et al., 2012). Prediction error refers to the discrepancy between the expected and observed values and is affected by the introduction of new data points like primary reflections. One such use of predictive deconvolution is trying to forecast a trace based on nearby traces. This is an effort to suppress multiples that originate from reflectors on or very close to the Earth's surface (Yilmaz, 2001, p. 170; Egbai et al., 2012).

When applying deconvolution to seismic data, one may start by looking at reverberations in the data by adding an autocorrelation display on each shot gather. This autocorrelation function may be considered a special case of cross-correlations. This means that given two functions $f(t)$ and $g(t)$ and making them be equal to each other, the cross-correlation function $\psi(\tau)$ can be simplified to produce the auto-correlation function $\psi_{ff}(\tau)$ as follows Equations 3.21 and 3.22 (Yilmaz, 2001, p. 171).

$$\psi_{ff}(\tau) = \int_{-\infty}^{\infty} f(t)f(t+\tau)dt \tag{3.21}$$

(For continuous functions)

$$[\psi_{ff}]_j = \sum_{i=-\infty}^{\infty} f_i f_{i+j} \tag{3.22}$$

(For discrete functions.)

In addition to auto-correlation and predictive functions, one filter that is crucial is the optimum wiener filter, which aims to produce an estimate of the desired signal by linear time-invariant filtering of the observed noisy signal. The filter is designed in the frequency domain and is optimum in the mean square error sense, meaning it minimizes the average of the squared differences between the estimated and true signals (Zhou, 2014, p. 152).

When deriving the mathematical expression for the Wiener filter, we consider a noisy signal $x(n)$, where n represents a discrete-time signal (an integer that represents the index of the sequence of trace samples in the signal). The optimum Wiener filter $W(f)$, where f stands for the frequency, is designed to estimate the desired signal $d(n)$. The expression for filters in the frequency domain is given by Equation 3.23, where $P_{dx}(f)$ is the cross power spectral density between the desired signal and the noisy signal while $P_x(f)$ is the power spectral density of the noisy signal.

$$W(f) = \frac{P_{dx}(f)}{P_x(f)} \tag{3.23}$$

3.5.10 Velocity Analysis

An ultrasonic log is a direct measurement of the velocity that seismic waves travel in the Earth as a function of depth, whereas seismic data provide an indirect estimate of velocity. Calculating velocities calls for the information supplied by common midpoint (CMP) recording, which is recorded at non-zero offsets. The estimated velocities can be employed to correct the travel times of reflections for non-zero offset and to combine the recorded data volume in midpoint-offset-time coordinates (Landa et al., 2008). A hyperbolic curve represents the reflection traveltime as a function of offset for a horizontal layer with a uniform velocity (Yilmaz, 2001, p. 93).

Normal moveout (NMO) is the basis for computing velocities of seismic data and it is the time difference between the travel time at a particular offset and the travel time with zero offset. The typical moveout velocity is the speed at which normal moveout must be compensated for. If one considers a basic Earth model that has only one horizontal reflector, then the NMO (normal moveout) velocity is equivalent to the speed of the medium located above the reflector. Moreover, if a model has a dipping reflector, the NMO velocity can be obtained by dividing the velocity of the medium by the cosine of the angle at which the reflector is dipping (Fomel et al., 2007).

3.5.11 Correcting Normal Moveout Velocity for a Flat Reflector

It is necessary to correct the reflection transit durations for NMO before summing up the traces in the CMP collected through the offset axis. There are several factors that influence the normal moveout correction when processing seismic data, including the reflector's dip, azimuth of the source and receiver relative to the direction of the true-dip, offset, the zero offset two-way travel time related to the reflection event, and the complexity of the near-surface and the medium over the reflector (Yilmaz, 2001, p. 94). Figure 3.13 depicts a medium with a single flat reflector.

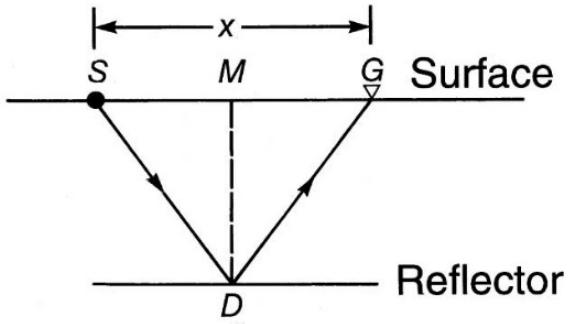

Figure 3.13: Normal moveout (NMO) diagram of a flat/horizontal reflector. Here, S is the seismic source, G is the seismic receiver, M is the halfway between the seismic source and receiver, and D is the point at which the incident seismic ray is reflected (Yilmaz, 2001, p. 280).

The arrival time of reflections at a receiver located at a certain distance from the shot point is subtracted from the arrival time at a receiver located at the shot site to calculate NMO. An increasing offset causes the seismic wavelet to arrive late at the receiver antenna. This is not attributable to underlying irregularities, but rather to the longer path taken by the seismic wavelet (Fomel et al., 2007). Therefore, an offset-specific temporal correlation is required. With perfect timing, the CDP gather's mostly reflected signals would be aligned in a straight line, and this is what the NMO correction is designed to do. Equation 3.24 represents the traveltime equation as a function of offset and is used when applying NMO on seismic data (Al-Sadi, 1980, p. 136).

$$t^2 = t_0^2 + \frac{x^2}{v^2} \tag{3.24}$$

In the above equation, x represents the displacement (offset) between the source and receiver locations, v represents the medium velocity above the reflecting interface, and t_0

represents twice the transit time down the vertical route MD. One must understand that the midpoint M corresponds with the vertical projection of depth point D to the surface along the normal to the reflector. Only with a horizontal reflector does this occur (Fomel et al., 2007).

During the process of applying NMO, the trace goes through a tiny non-linear stretch that is referred to as the NMO stretch. Because of the NMO correction, a frequency distortion occurs, and it happens most noticeably for shallow events and at large offsets. The maximum stretch that is allowed is 10 percent, and any signals that are detected in areas where there is a greater stretch than that will be muted (Kiran, 2005). The stretch is quantified using the Equation 3.25, where f is the prominent frequency, Δf is the change in frequency and $\Delta t_{NMO} = t - t_0$

$$\frac{\Delta f}{f} = \frac{\Delta t_{NMO}}{t_0} \tag{3.25}$$

3.5.12 Correcting Velocity for Dipping Reflectors

If the reflector of concern is dipping, in addition to the NMO adjustment, an additional correction that takes into account the angle of the reflector must be performed. Figure 3.14 illustrates a material that contains only one reflector that is partially submerged.

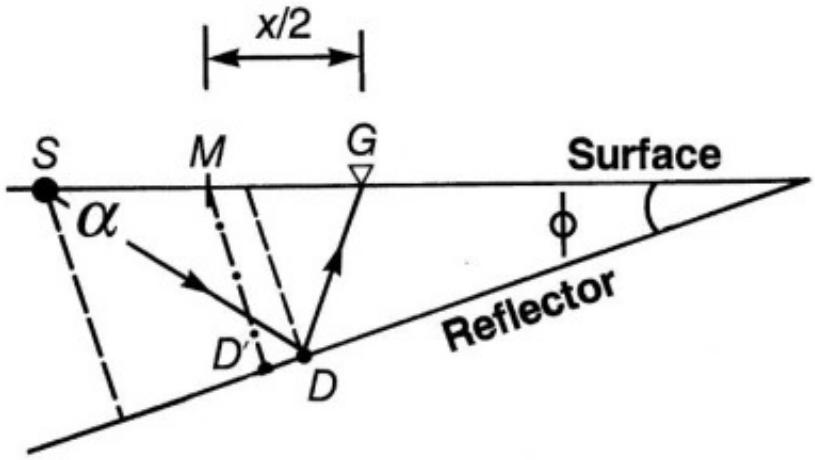

Figure 3.14: Normal moveout (NMO) geometry for a single dipping reflector. This figure shows the source (S), the receiver (G), the distance between the source and the receiver (x), the midpoint between the source and receiver (M), the angle of incidence (α), the dip angle (ϕ), and point of reflection (D) (Yilmaz, 2001, p. 287).

When calculating the time it takes for a seismic wave to travel from the source location (S) to the reflector at depth point (D) and then back to the receiver position (G) one needs to consider that the midpoint (M) of the dipping reflector is no longer a vertical projection

of the depth point to the surface in this configuration. According to Levin (1971), this dipping geometry can be used to derive a two-dimensional traveltime equation and it is expressed as follows, where the two-way travel time t is associated with the nonzero offset ray path SDG that goes from the source (S) to the reflection point D to the receiver G, the two-way zero offset time t_0 that is associated with the normal-incidence ray path M-D that passes through the midpoint (M) and the angle that exists between the normal to the dipping reflector and the direction of the line of recording (α).

$$t^2 = t_0^2 + \frac{x^2 sin^2\alpha}{v^2} \tag{3.26}$$

The moveout velocity can then be given by:

$$v_{nmo} = \frac{v}{sin\alpha} \tag{3.27}$$

For the geometry of the dipping reflector depicted above, where ϕ is the dip angle of the reflector, it must be noted that:

$$sin\alpha = cos\phi \tag{3.28}$$

This implies that Equations 3.26 and 3.28 can be written in terms of ϕ, to get:

$$t^2 = t_0^2 + \frac{x^2 cos^2\phi}{v^2} \tag{3.29}$$

and

$$v_{nmo} = \frac{v}{cos\phi} \tag{3.30}$$

Conclusively, the dip angle affects how the NMO velocity is calculated for a reflector that is sinking. When the dip angle is increased, the moveout velocity also increases, which results in a reduced moveout distance (Yilmaz, 2001, p. 286). When considering a dip of 15 degrees, there is a discrepancy of 4 percent between the moveout velocity v_{nmo} and the medium velocity, v. At a dip of 30 degrees, the difference is fifty percent, and

it quickly becomes larger as the angle of the dip rises. A further observation that goes along with this finding is that a horizontal layer that is moving at a high velocity can produce the same moveout as a dipping layer that is moving at a low velocity (Kiran, 2005).

3.5.13 Migration

Migration is the third principal process when processing seismic data. A typical practice is to enhance the horizontal detail by collapsing diffractions and relocating dipping features to their presumed true depths (Yilmaz, 2001, p. 463). This is usually carried out on the stacked section, which is believed to be comparable to a zero offset section. Migration is an imaging process and the fact that it is based on the wave equation makes it a deterministic process.

Chen et al. (2015) illustrate that the output received after the migration is usually self-evident, i.e., it is obvious whether or not the input was correctly migrated. When the outcome is not obvious, the precariousness is frequently attributed to a lack of precision in the velocity information provided as input to the processing modules. Other elements influencing migration results include migration strategies such as depth or time, pre- or post-stack, algorithms, and associated parameters.

Seismic energy undergoes one of three processes when it reaches an interface between two types of rock with different acoustic impedances: it is either refracted, reflected upward to the surface, or absorbed by the medium (Hale, 1992). When the reflected energy reaches the surface, it is picked up by geophones that have been positioned a certain distance away from the point where the waves originate. A geophysicist analyzing the energy detected by a geophone is cognizant of the duration it takes for the waves to travel as well as the separation between the transmitter and the receiver. However, they lack knowledge regarding the depth of the reflecting surface (Chen et al., 2015).

The mathematical relationship $d = \frac{v.t}{2}$, where d is the distance, v is the seismic velocity and t is the time it takes seismic waves to travel from the source to the receiver can be used by a geophysicist with the objective to locate a reflection occurrence in the most uncomplicated geological scenario, where there is only one level horizontal surface to reflect off, a uniform velocity, and both the source and receiver are positioned at the identical spot (Stolt, 1978). The distance is halved in the mathematical relationship because it can be assumed that the time it takes to get to the reflector from the source is just one-half of the total travel time; the time it takes to go back to the receiver is the

other half (Chen et al., 2015; Xue et al., 2016).

Assuming a horizontal reflector in a simple scenario, it can be considered safe to presume that the reflection is positioned vertically beneath the location where both the source and receiver are located (Figure 3.15). If a reflector is dipping, the first reflection will come from a higher point in the direction of the dip (Figure 3.16). The situation is more complicated and as a result, the travel-time plot will show a decreased dip, which is characterized by the "migrator's equation", i.e., $tan\xi_a = sin\xi$ where ξ_a is the apparent dip and ξ is the true dip.

Moreover, geophysicists rely heavily on zero offset data since they make the migration procedure much more straightforward and allow for the data to be represented by spherical surfaces. When data are collected at non-zero offsets, the sphere transforms into an ellipsoid, which is a shape that is far more difficult to describe (both geometrically, as well as computationally) (Stolt, 1978; Xue et al., 2016). The issue resulted in finding a solitary numerical value that actually denotes a semi-spherical range of lengths between the origin and the recipient, within which the reflection could have originated.

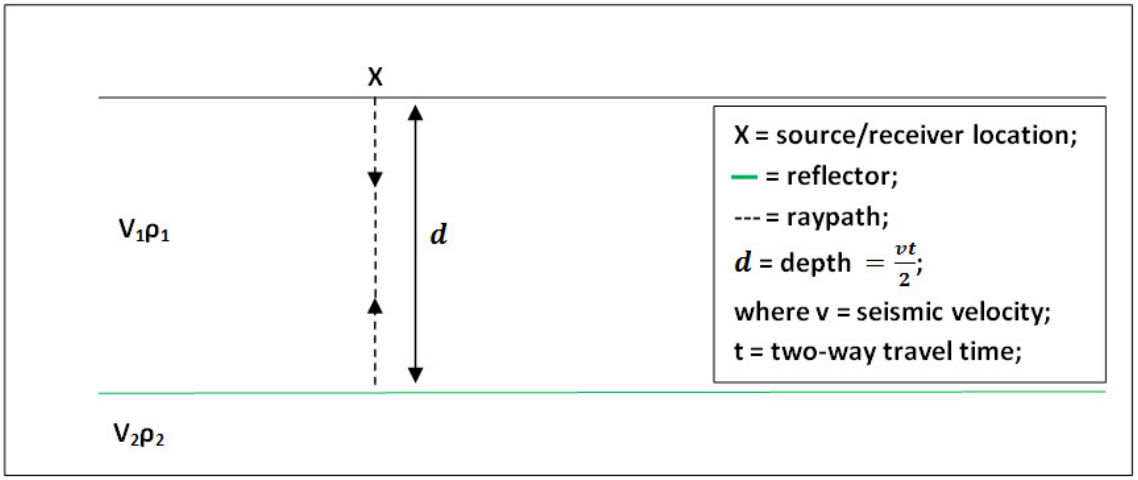

Figure 3.15: The ray path for a reflection with zero offset off of a horizontal reflector. Here, the velocity of a layer is given by V and the density of a layer is given by ρ (Xue et al., 2016).

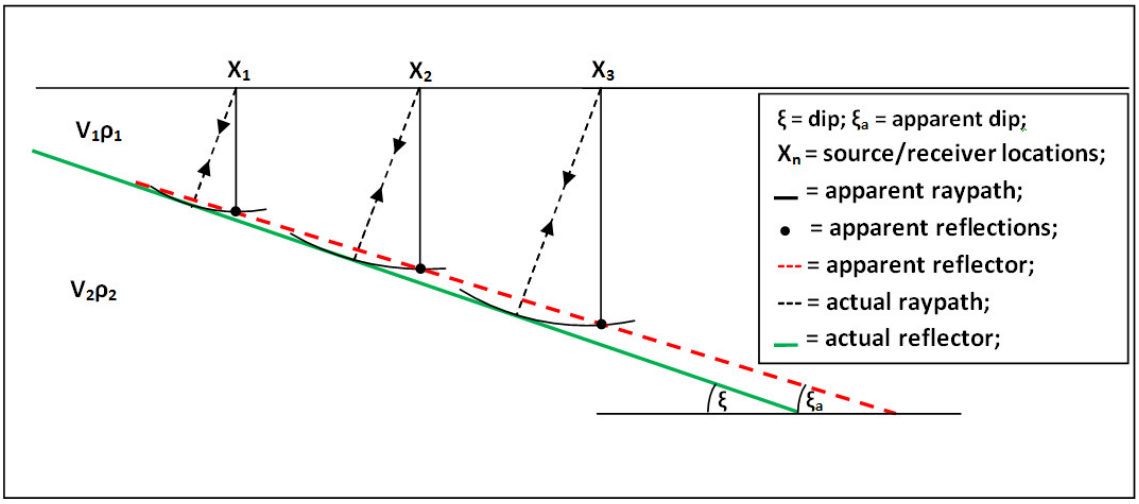

Figure 3.16: The ray path for a reflection with zero offsets from a dipping reflector, as well as the subsequent apparent dip (Xue et al., 2016).

According to the concepts of geophysics, a region is considered to have complicated geology if there is a significant contrast in the lateral and/or vertical velocity of the rock. The following are some examples of what a geophysicist might regard to be complicated geological features: faulting, folding, salt bodies, fractures, and unconformities. In these kinds of circumstances, a method of migration known as pre-stack migration is used (Sheriff and Geldart, 1995; Yilmaz, 2001). Pre-stack migration is better at accounting for changes in velocity than post-stack migration, which results in an overall enhancement.

Time migration and depth migration are the two primary types of migration algorithms that geophysicists can use. The geophysicist's budget, the time constraints, and the subsurface geology all play a role in which type of migration algorithm they choose to use (Sheriff and Geldart, 1995, p. 334; Yilmaz, 2001, p. 470; Chen et al., 2015). Time migration is a sort of migration that is based on the premise that there are only slight fluctuations in lateral velocity, and this assumption is invalidated in the presence of the most intriguing and complicated subsurface structures. It is performed on seismic data stored in time. Stolt migration, Gazdag migration, and finite-difference migration are only a few of the temporal migration methods that are often utilized (Bonomi and Cabitza, 1994; Onajite, 2013).

On the other hand, the depth migration algorithm is used for seismic data that are represented in depth. These depths must first be computed using seismic data that are represented in time. As a result, using this approach necessitates the construction of a seismic velocity model, which is a time-consuming and iterative process. This implies that the method requires a significant amount of resources. The fact that this migration

approach may be effectively used in regions with lateral velocity changes, which typically are the regions that tend to be of interest to petroleum geologists, is the key benefit that this method offers.

The Kirchhoff migration, the reverse time migration (RTM), the Gaussian beam migration, and the wave-equation migration algorithms are only a few of the common depth migration algorithms (Bonomi and Cabitza, 1994; Onajite, 2013). In the context of this study, especially pertaining to hard rock seismic, Kirchhoff seismic migration is particularly relevant. Its ability to image beneath complex overburdens makes it especially suitable for hard rock terrains. While other methods have their merits, the emphasis on Kirchhoff is driven by its specific relevance to hard rock seismic investigations.

3.5.14 Migration Algorithm: Kirchhoff Migration

Kirchhoff migration is identified as migration by integrating, summing, and weighing the energy input across diffraction curves, then positioning the findings at the crests of the diffraction curves (Sheriff, 2002, p. 475). The Kirchhoff migration method is effective at correcting dip angles of up to 90 degrees; however, it is unable to deal with significant changes in lateral velocity. The Kirchhoff equation is an integral version of the wave equation. It expresses the wave function ψ at the point P in terms of the sum (integral) of contributions from a surface encompassing the given point and its normal derivative. Equation 3.31 is the wave equation derived by assuming a 2D acoustic and constant density,

$$\frac{\delta^2\psi}{\delta x^2} + \frac{\delta^2\psi}{\delta z^2} + \frac{1}{V^2}\frac{\delta^2\psi}{\delta t^2} \tag{3.31}$$

where $\psi = \psi(x, z, t)$ represents the pressure of the wavefield, x denotes the horizontal distance, z denotes the depth and t represents time (Hale, 1992). Equation 3.32 can be used to express the Kirchhoff integral as follows.

$$\psi(x, z, t) = \frac{z}{\pi}\int \frac{1}{r^3} - (\frac{2}{Vr^2})(\frac{\delta}{\delta t})\psi(x\prime, 0, t+\tau)\, dx\prime \tag{3.32}$$

where $x\prime$ is the horizontal location of the recorded data on the surface, $\tau = \frac{2r}{V}$ denotes the two-way traveltime, V denotes the velocity and r denotes the distance from $x\prime$ to x (Hale, 1992). Moreover, important factors of the Kirchhoff migration include the width of the aperture as well as the dip to migrate seismic events (Yilmaz, 2001, p. 481). It was

intended for the dip migration aperture (margin) to be able to offer full-fold coverage of the subsurface target region following migration.

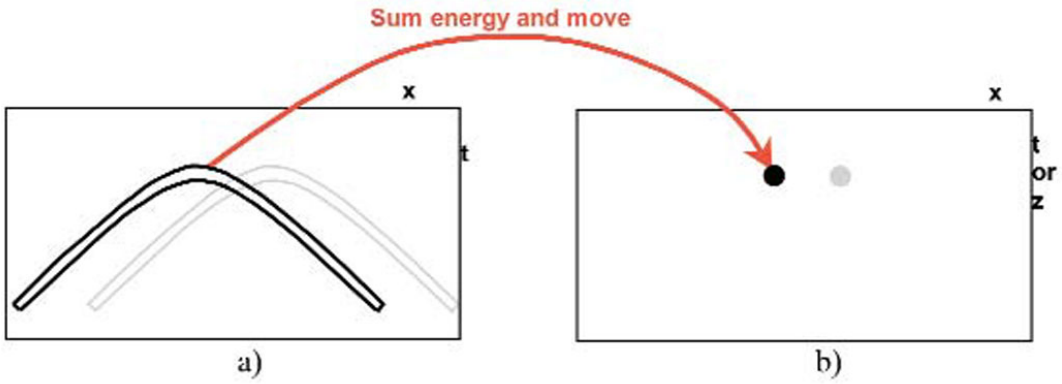

Figure 3.17: The diagram shows how Kirchhoff migration sums an input of diffraction energy (a) summed and at the point of scatter and (b) the migrated section (Baker and Copson, 2003).

4. Methodology

4.1 Acquisition of Profile RT480

The data were acquired in 1992 by AngloGold Ashanti Ltd using a Vibroseis truck and were granted to the Seismic Research Centre of the University of the Witwatersrand. A detailed synopsis of the survey acquisition parameters is presented in Table 4.1 (Scheiber-Enslin et al., 2014). Four vibroseis trucks were utilized at every shot point position during the acquisition. The general trend of the survey line was South East (SE) to North West (NW), and it was designed with a recording length of 16 s and a sweep length of 26 s where the trucks were arranged in a linear array configuration, each running a linear sweep of 10 to 60 Hz.

Both receiver and shot spacing was set to 50 m. This profile has a total of 670 shots with a 50 m spacing amongst the receivers and a nominal fold of 48. The geometry of the survey followed a split spread with 60 geophones, one on each side of the shot that was also spaced at 50 m. The data were recorded using the Sercel SN 368 recording system and were initially stored in SEG-D format and then converted to an SEG-Y format at later stages (Scheiber-Enslin et al., 2014). Moreover, the post-correlated shot-gather data were obtained along with the observer's investigation logs.

The received dataset was in a format incompatible with modern data processing tools. Elevations were not included in the seismic line's original coordinates; thus, the first step was to use the USGS Shuttle Radar Topography Mission (SRTM) to assign elevations to the extracted Eastings and Northings. Following this, a tailored Matlab program was utilized to assign peg numbers to every receiver location and merge the geometry data with revised coordinates into the SEG-Y data headers. All traces were placed in 25 m wide bins based on their median values (Table 4.1).

Table 4.1: Details of the acquisition parameters for profile RT480.

Survey Parameters
Type of Survey : 2D crooked line **Year**: 1992 **Profile length** : 65 km **Trend** : SE-NW **Split spread** : 3700-50-X-50-3700 (m) **Nominal fold** : 48
Recording System
Recording device : Sercel SN 368 **Sampling rate** : 2 ms **Record length** : 16 s **Sweep length** : 26 s **Sweep frequencies** : 10-60 Hz linear
Source Information
Source spacing : 50 m **Source type**: 4 Pelton MK II Vibrators in a line
Receiver Information
Receiver Spacing : 50 m **Geophone Type** : 10 Hz (SM4U)

4.2 Processing Profile RT480

4.2.1 High-level Overview

Conventional seismic processing is a series of statistical and mathematical processes performed on the acquired raw data so that important geological information can be extracted (Al-Sadi, 1980, p. 125). The processing steps represent an input and output system where the raw data represent the input and the resulting stack represents the output. The two main components in the processing sequence are computer hardware and software systems. The processes through which the data are taken ensure that the data are formatted correctly, noise interfaces are removed, amplitude recovery is applied and other relevant corrections are implemented (Al-Sadi, 1980, p. 126; Yilmaz, 2001, p. 92).

The procedure is not rigid. Seismic data processing varies from one processing center to another, and even within a given center, there may be slight variations in the finer

points of the procedure (Hatton et al., 1986). Yet, all processing operations tend to adhere to a universal format for the fundamental stages involved. The processing sequence is broken down into three distinct phases for the sake of clarity in the discussion: Data reorganization, pre-processing, pre-stack processing, and post-stack processing (Nguyen et al., 2015).

The seismic shot records and the supplemental "statistics" data are the two primary types of raw data given by the field team and used as processing input (normally recorded on CDs or magnetic tapes or harvested from nodes). The observer's report is part of the shooting statistics and includes in-depth descriptions and comments on all of the recorded shots. The shooting geometry and, usually, the field statics calculated with respect to a specific datum level are included in the report as well. These crucial processing techniques that were used to process profile RT480 are discussed below. The Globe Claritas software was utilized to implement the procedures.

4.2.2 Building the Geometry from SPS Data

The SEG standard for survey data files is called SPS (shell processing support), originally invented by Shell. This standard describes survey lines with three ASCII files, i.e., a shots file containing the X, Y, Z coordinates of each shot location with a (.s) extension, a receivers file containing the X, Y, Z coordinates of each receiver location with a (.r) extension and lastly, a relations file that maps the channel number and SHOT ID to the location of shot and receiver. All of the seismic traces' location data are compiled into a geometry database and then merged into the headers of all traces (Al-Sadi, 1980, p. 126; Yilmaz, 2001, p. 66).

In this step, several parameters such as input files, survey type, and position tolerance were retrieved to set up the survey information from SPS files. A job file was executed to run so that the application scans through the SPS data and provide a summary of anomalies detected in the file as well as what has been located. Once this job is executed, a map loads with the survey data superimposed on it. Each individual shot or receiver position is referred to as a "survey peg". Figure 4.1 shows some of the shot and receiver peg locations color-coded by elevation.

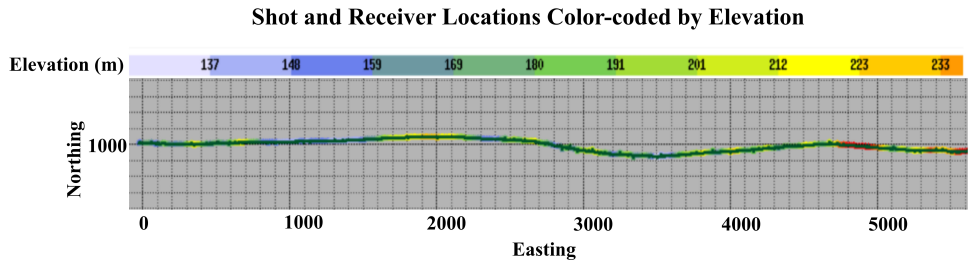

Figure 4.1: The initial map of the seismic profile with the survey pegs color-coded with the respective values of shot elevations.

4.2.3 CDP Sorting

Gathers of traces that share a common depth point (CDP) are a necessary step in processing seismic data. To do this, a grid of CDP "bins" were established along the profile, and then group traces were grouped into a bin based on whether or not the middle position connecting the shot location and the receiver location is inside the bin's boundaries. By establishing a series of "hitpoints," a trajectory for the CDP bins to follow was set; these bins were then moved along the best-fit spline curve between the defined points. When the SPS data are imported, the CDP data are added to the geometry database as displayed in (Figure 4.2).

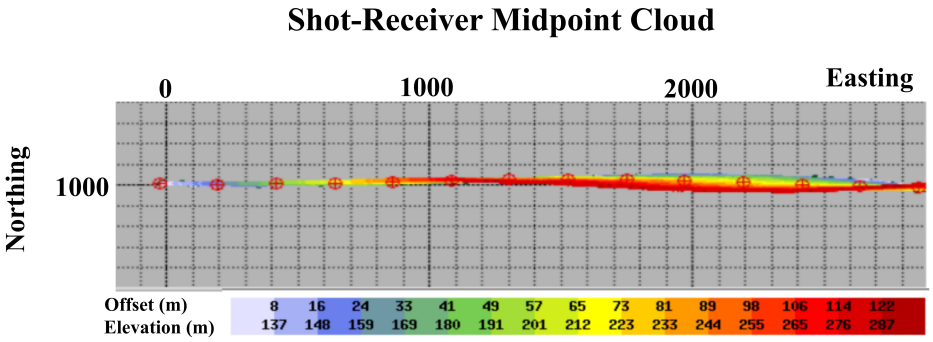

Figure 4.2: The midpoints of shot-receiver pairs, color-coded by offset and elevations. The common depth point (CDP) bins were assigned throughout the center of the profile. The red circles on the cloud represent automatically generated hitpoints that enable one to define a path for the CDP bins to follow along the seismic profile.

4.2.4 Floating Datum Static Corrections

Time shifts based on a set velocity called the replacement velocity are used to rectify the data as if the shots and receivers were on the fixed plane (Sheriff and Geldart, 1995, p.

305; Yilmaz, 2001, p. 381). For this case, a replacement velocity value of 3600 m/s was used. The fixed datum becomes "time zero" on the final seismic section and it is often positioned at a height that is higher than the highest elevation measured during the survey. In addition to this, the floating datum is stored as static shifts that are related to the CDP number of the traces. Because the processing software enables the ability to do so, a quality control display of the floating datum was obtained. This allows one to verify the degree of smoothness. Figure 4.3 shows the obtained smooth profile for the seismic data.

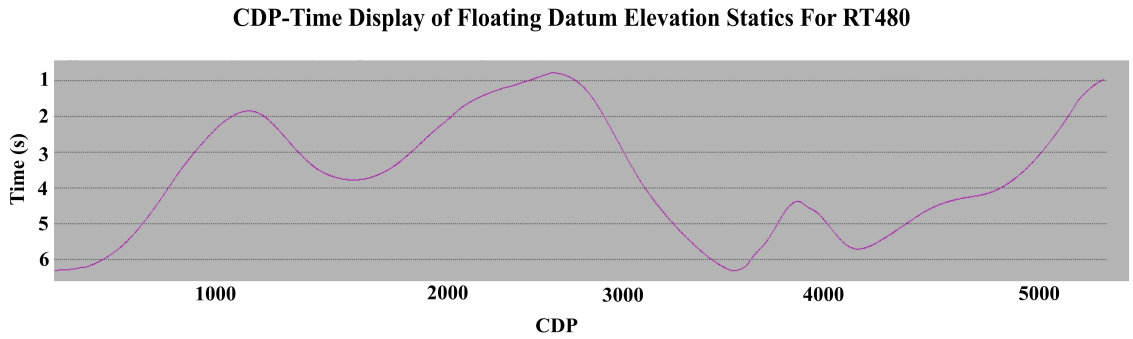

Figure 4.3: Common Depth Point (CDP) - Time display of floating datum elevation statics for the profile. This correction helps reduce undesired seismic velocity variations across the profile and it was performed during the geometry setup process.

4.2.5 Merging Trace Headers and Geometry

Seismic data are stored in file formats. This means that a version of the raw input data with the geometry information blended into the trace headers had to be constructed, where initially there was only a file number (SHOT ID) and trace inside that file (CHANNEL) declared. After merging the geometry the rest of the headers become configured and embedded into the seismic data. The headers are stored in a file with (.ahl) extension and it includes the shot and receiver heights and positions as well as peg numbers assigned to each shot and receiver. Peg numbers were created and assigned using a custom Matlab code. The merging was then performed using a processing flow. Figure 4.4 below shows the two-dimensional image obtained after merging the trace headers into the seismic data.

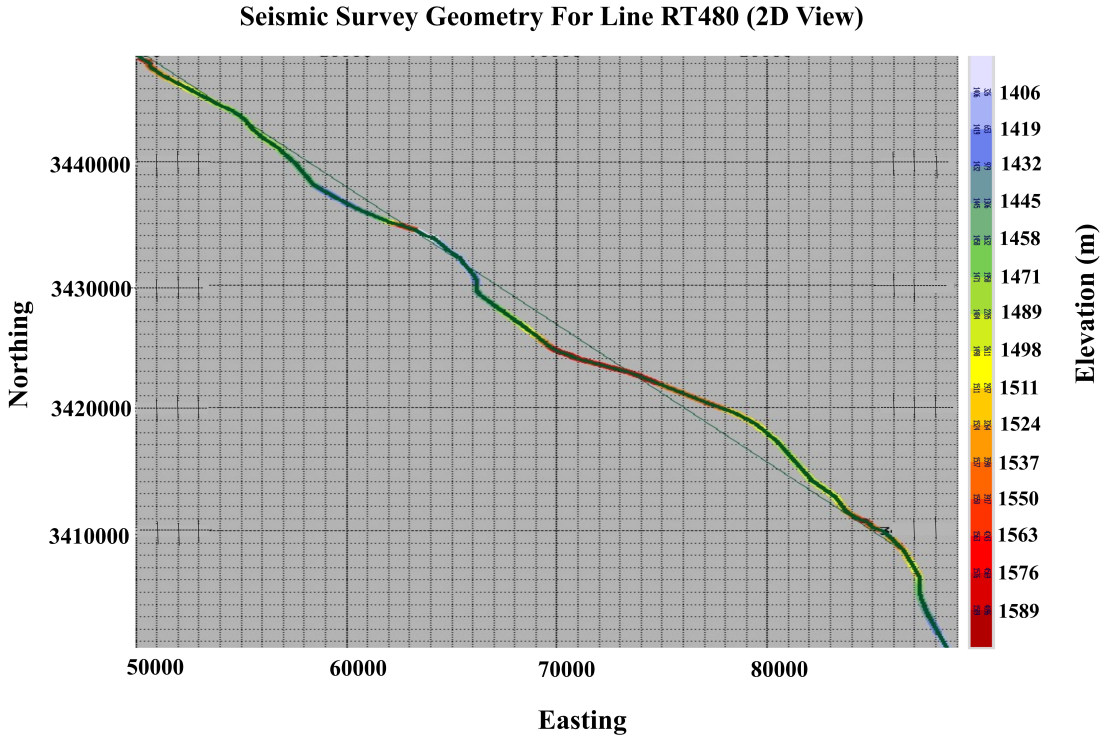

Figure 4.4: Two-dimensional view of the seismic line after geometry setup. At this stage, the geometry data were generated from the standard point source (SPS) database and were merged with the data across the common depth point (CDP) intervals.

4.2.6 Verifying Correctness of Geometry

The correctness of the geometry was verified by checking if height and near-surface velocities were accounted for in such a way that the pattern in the seismic data matches the pattern in the offset. Geometry quality control (QC) was checked to verify the correctness of the geometry. The most important thing was to have the trace with the shortest "first arrivals" duration be the one closest to zero offset.

Normally, the seismic data and survey results wouldn't agree if the first arrival times of the shot record didn't coincide with the peak close to the smallest offsets. Any discrepancy could be due to the "relations" SPS file, which maps the survey pegs to the file and channel numbers. This is a common source of errors that can be traced back to the original cause with little effort. Figure 4.5 (a) shows how the correctness of the geometry for seismic data can be verified while Figure 4.5 (b) shows the frequency spectrum of the shot gather under consideration.

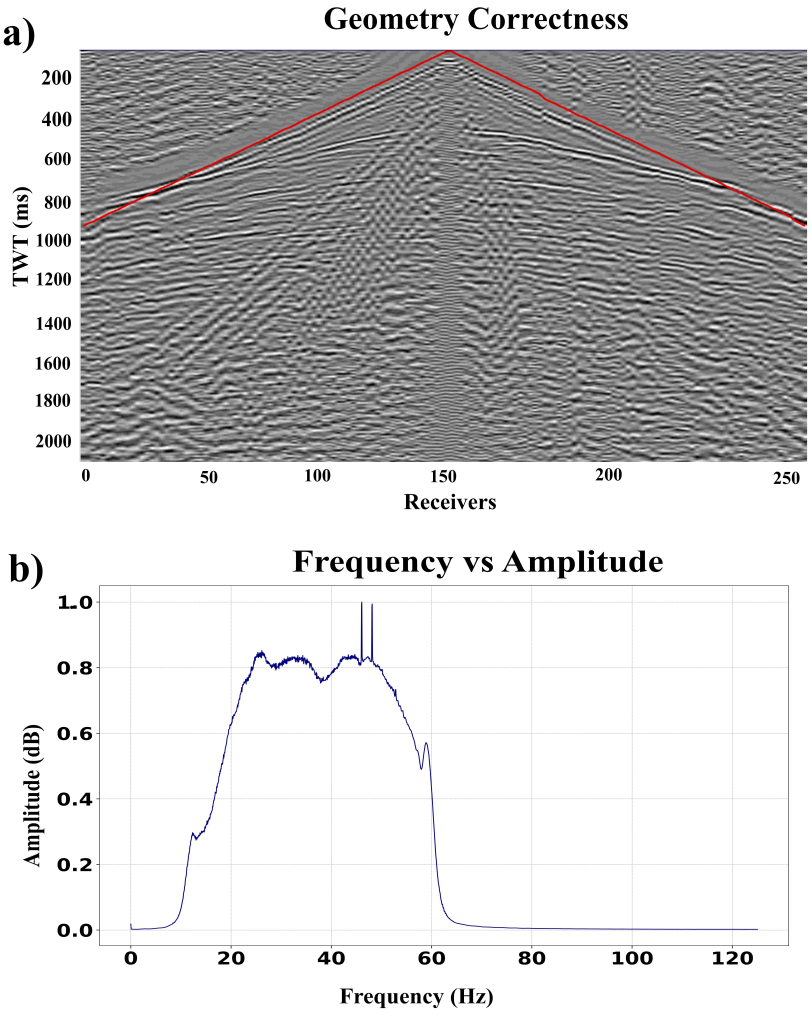

Figure 4.5: (a) Shot gather with marked offset. The offset (red line) was converted to time using a constant velocity value. The first arrivals in the seismic shot match the peak of the red line, demonstrating that the earliest arrivals correlate to the lowest offsets. (b) Frequency spectrum of the shot record.

4.2.7 Generating a Brute Stack

Common depth point (CDP) stacking is the most efficient method for improving signals. Seismic traces are added together mathematically in this procedure if they all originate from the same reflection point (the same CDP trace-gather). The total of these collections generates a new trace (the stack trace) that represents the average of all traces in the CDP-gather. Reflection signals on separate traces are added together in this way to create a single, greater amplitude reflection signal. Since seismic noise is inherently chaotic, it

may be minimized by destructively summing it (Yilmaz, 2001, p. 7). Figure 4.6 is a brute stack for profile RT480. This stack was generated once the geometry of the seismic profile was established. Upon verifying the correctness of the geometry, a normal moveout (NMO) algorithm was applied to the raw shot gathers to produce this preliminary brute stack.

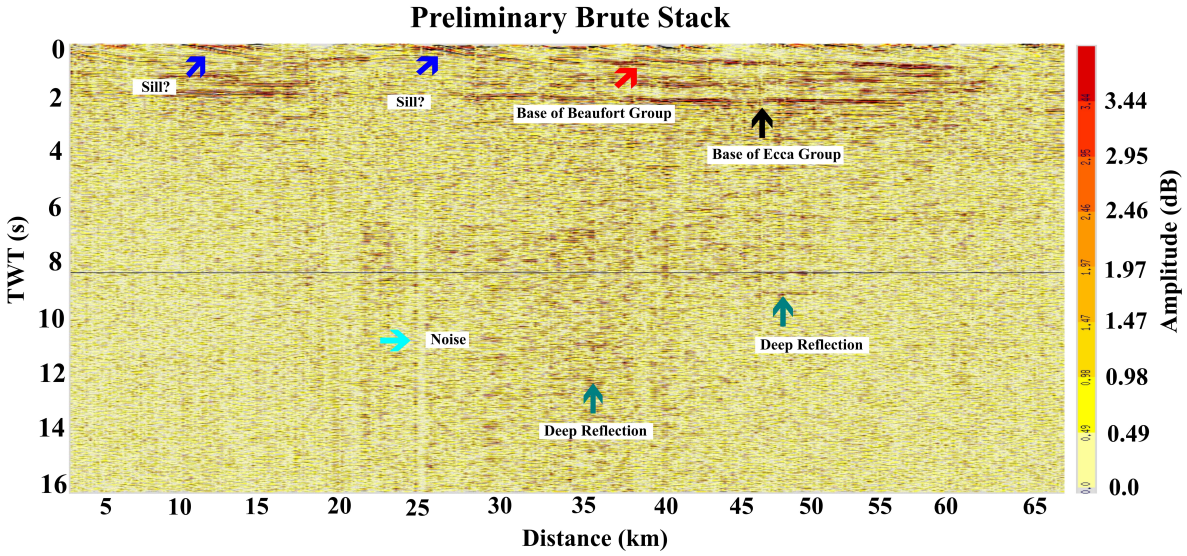

Figure 4.6: Preliminary brute stack of the entire profile. This is a brute stack of the raw shots generated after establishing the geometry of the seismic data. The red and black arrows indicate some reflections associated with boundaries between the layers, the blue arrows show dipping reflection events associated with sills, the light green arrow around 11 s two-way travel time (TWT) shows some noise in the data and the green arrows show some of the seismic reflection events present at greater depths.

4.3 Application of Gain Recovery Functions

This processing is concerned with correcting the effects of amplitude losses such as geometric spreading by applying several recovery functions. Gain is a time-variant scaling in which the scaling function is based on the desired criterion (Al-Sadi, 1980, p. 128). It is applied on different levels of processing, i.e., on both pre-stack and post-stack stages. Moreover, the gain is applied to seismic data for display purposes, e.g., AGC (Automatic Gain Control) enhances weak signals when applied to the data. It is important to apply gain with caution because the character of the signal can be potentially destroyed (Yilmaz, 2001, p. 81). A good example of this situation is when strong reflections become similar to weak reflections from applying an instantaneous Automatic Gain Control with relatively small time gates (Yilmaz, 2001, p. 82). Figure 4.7 (a) shows a shot record before applying the recovery function and Figure 4.7 (b) shows the results after applying

a gain function.

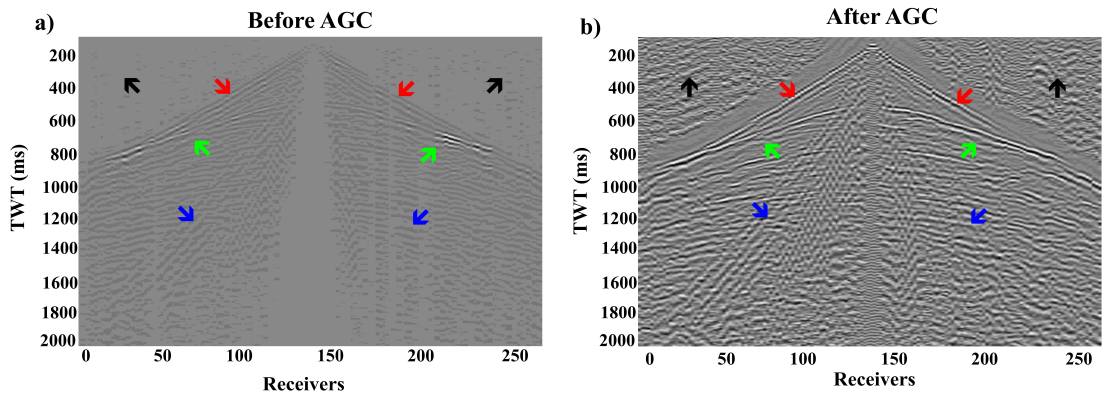

Figure 4.7: (a) Raw shot gather from the seismic data before applying a recovery function. One can observe that it is difficult to identify most of the seismic waves, e.g., noise (black arrows), P-wave first breaks (red arrows), ground rolls (blue arrows), and P-wave reflections (green arrows). (b) The same shot gather after applying normal AGC (automatic gain control) with a window length of 300 ms. It is evident that AGC helps enhance the desired signals of the wavelets. The different seismic events are indicated with the corresponding arrows.

4.4 Pre-stack Processing

4.4.1 First Break Picking

P-wave first breaks, also known as first arrivals, are the initial transmission of energy from a surface source to a geophone (Yilmaz, 2001, p. 374). They also serve as the trace's first indicator of seismic energy. The first break occurs when these traces appear. It's important to keep in mind that the near-surface circumstances and the kind of source employed during acquisition might drastically affect the quality of the first breaks. The departure of first arrivals from the overall linear trend may substantially be ascribed to the change in elevation together with the shot profile.

The technique of identifying the initial seismic signal, known as first break picking, can be executed through various methods: interactively, by hand, fully automated, or by employing a blend of these strategies (Sheriff and Geldart, 1995, p. 306; Yilmaz, 2001, p. 374). It's essential to recognize that the accuracy of this picking technique is fundamental in determining the success of static correction approaches that are based on both

reflection and refraction principles. If executed with precision, the initial seismic waves and those refracted from the sub-surface layer of low velocity are rendered into a straight line after incorporating adjustments for elevation and the underlying low-velocity layer to the raw data. An illustration of this can be seen in Figure 4.8 (a), which displays the application of P-wave first break picking on a seismic shot record. Subsequently, Figure 4.8 (b) demonstrates the application of linear moveout (LMO) correction to the shot record, which is a crucial step in the process.

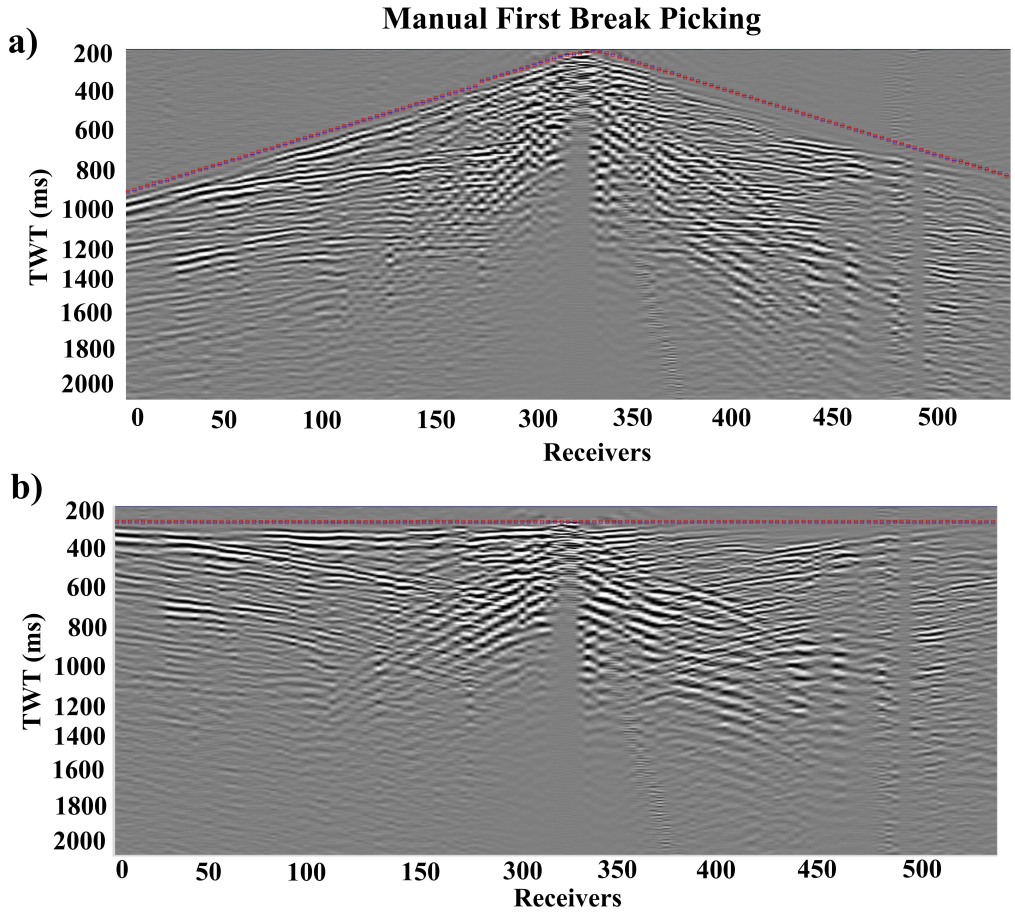

Figure 4.8: (a) Manual first break picking performed on a shot gather, the red line along the first arrivals represents the picks applied on this gather. (b) The shot gathers is flattened using a linear moveout approach to determine if the picks are done correctly. A straight line (red) indicates that the correct picks have been applied.

In other instances, shot records may resemble shallow and deep refraction events, distinct refraction events, noise-contaminated first breaks, a vibroseis shot gather with not-so-unique first breaks, and a shot record with a fuzzy first break initiation. To estimate the parameters of the model that lie close to the Earth's surface, an inversion method is applied to the first break picks that are linked to the delayed arrival timings. In this

scenario, the root mean square (RMS) inversion approach was applied (Woodward, 1992).

4.4.2 Dealing with Poor Picks

Poor picks from the inversion process were eliminated using the ability to modify/update and reload the first breaks to resolve bad picks on a shot or trace-by-trace basis. The 'High-residual rejection factor' is a new option on the 'refraction statics inversion parameters' that enables the user to ignore samples with abnormally high residuals. Standard deviations from the mean were used to establish the rejection factor; a value of 4 is normally acceptable.

To avoid disrupting the inversion before the model has stabilized, the rejection takes effect only after the first iteration. There is no automatic pick rejection performed if the parameter is not filled in. It was discovered that 0.9% of the picks done for this project and had to be eliminated using this rejection method. Figure 4.9 shows a plot for the polyselect rejection method applied in this profile.

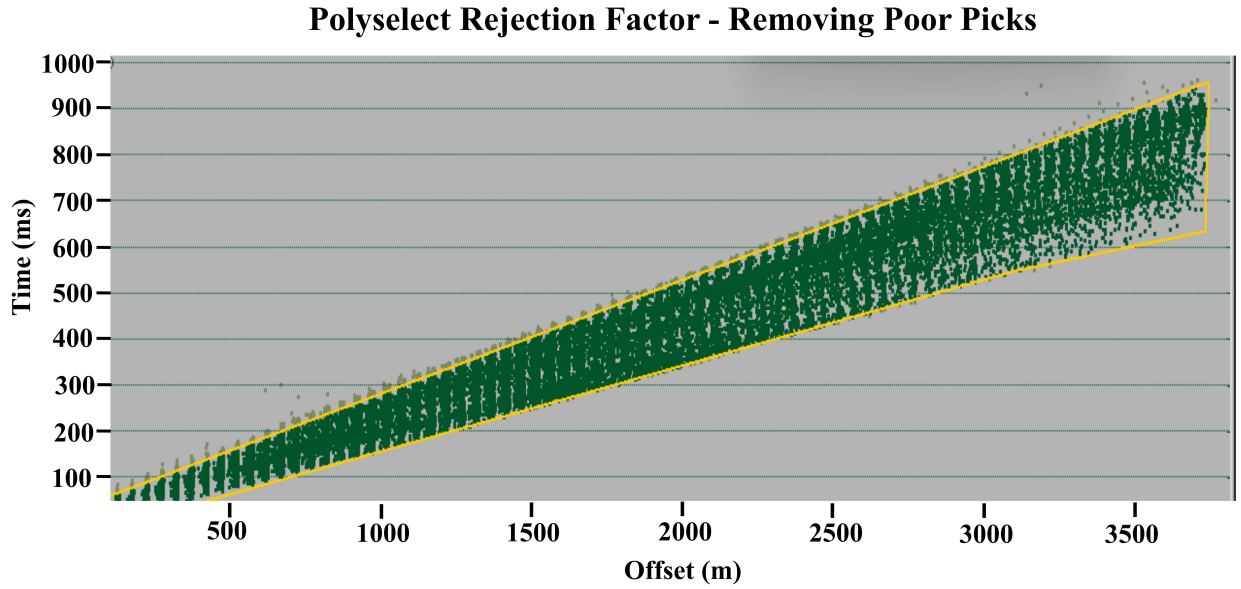

Figure 4.9: Time-offset plot obtained to check quality of picks. All shots are included and a polygon selection method was applied to eliminate poor picks and reserve the better ones so that refraction statics are applied as accurately as possible.

4.4.3 P-wave Refraction Tomography

The P-wave first breaks were also used to produce a P-wave tomogram (Figure 4.10 (a)). Seismic tomography is a technique used in geophysics to image the subsurface of the Earth with seismic waves. In this case, it is essentially a 2D model of the subsurface, indicating the velocity at which P-waves travel through different types of rocks and geological structures. These velocities can reveal a lot about the types of materials present and the physical conditions, like temperature and pressure. This refraction tomogram adds value to the seismic section and it does so because the static corrections supported by a refraction tomogram enhance the quality of the reflections on seismic sections.

The layers with color-coded seismic velocities represent different geological formations and features. Each layer has a specific P-wave velocity, which is typically measured in meters per second (m/s). The velocities depend on the rock type, porosity, fluid content, and other factors. High velocities often indicate hard, compact rocks like granite, while lower velocities may indicate softer or fractured materials. Figure 4.10 (b) is the accompany ray path diagram with shows the trajectory of the seismic waves.

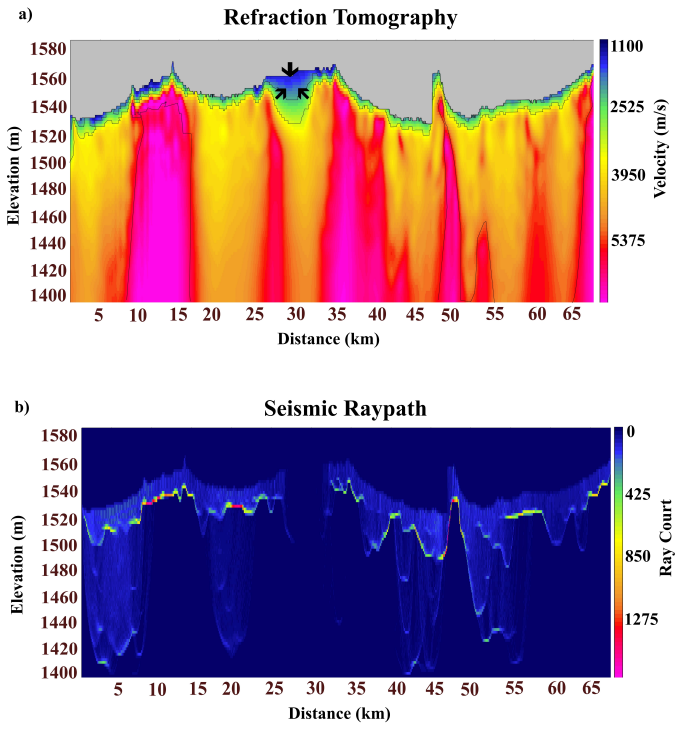

Figure 4.10: (a) The refraction tomography of P-wave velocities for the seismic data. (b) The path followed by the seismic waves during propagation (ray path diagram).

4.4.4 Refraction Statics

Seismic data often showcase significant variations in the terrain near the surface, ranging from hard, weathered outcrops to softer or even marshy soils. These variations result in substantial localized differences in seismic velocity, as extensively documented in the literature (Al-Sadi, 1980, p. 170; Yilmaz, 2001, p. 183). Such disparities in velocity are critical to address for accurate seismic analysis.

To correct these velocity variations, a method akin to "floating datum corrections" used for elevation discrepancies is employed. This technique involves estimating the differences in near-surface velocity and then compensating for them with a uniform replacement velocity. This approach, designed to standardize the velocity variations, is similar to adjustments made for elevation, ensuring consistent and reliable seismic interpretation (Yilmaz, 2001, p. 184).

4.4.5 Inversion Model

The initial step in assessing variations in velocity near the surface involved generating a velocity model based on refracted and direct waves. This model provided an approximation of the upper low-velocity stratum and its depth. To adjust for this stratum, a static correction model was formulated (Figure 4.11 (a)). Additionally, the times at which the first seismic waves were detected were recorded to construct a model of the near-surface velocity, which was subsequently used to calculate static corrections (Figure 4.11 (b)).

The procedure begins with the software creating a model that aligns with the data's layout. It then simulates the path of seismic waves, using the positions of the sources and detectors to estimate the theoretical times of first arrivals. These theoretical times are then matched against the actual recorded times, and adjustments are made to the model to reduce discrepancies between the two data sets (Figure 4.11).

The "sub-weathering layer," or the base layer of the velocity model, was also updated to improve the refraction velocity models (Figure 4.11 (c)). One may roughly infer this from the gradient of the first breaks throughout the first few meters, which represents the near-surface. Upper and lower bounds for velocity estimations were established so that they are consistent with the local geology. The velocity of these layers was then adjusted accordingly to produce a reasonable inversion model. It is generally advisable to begin with a simple model and add complexities as the model converges to the desired value.

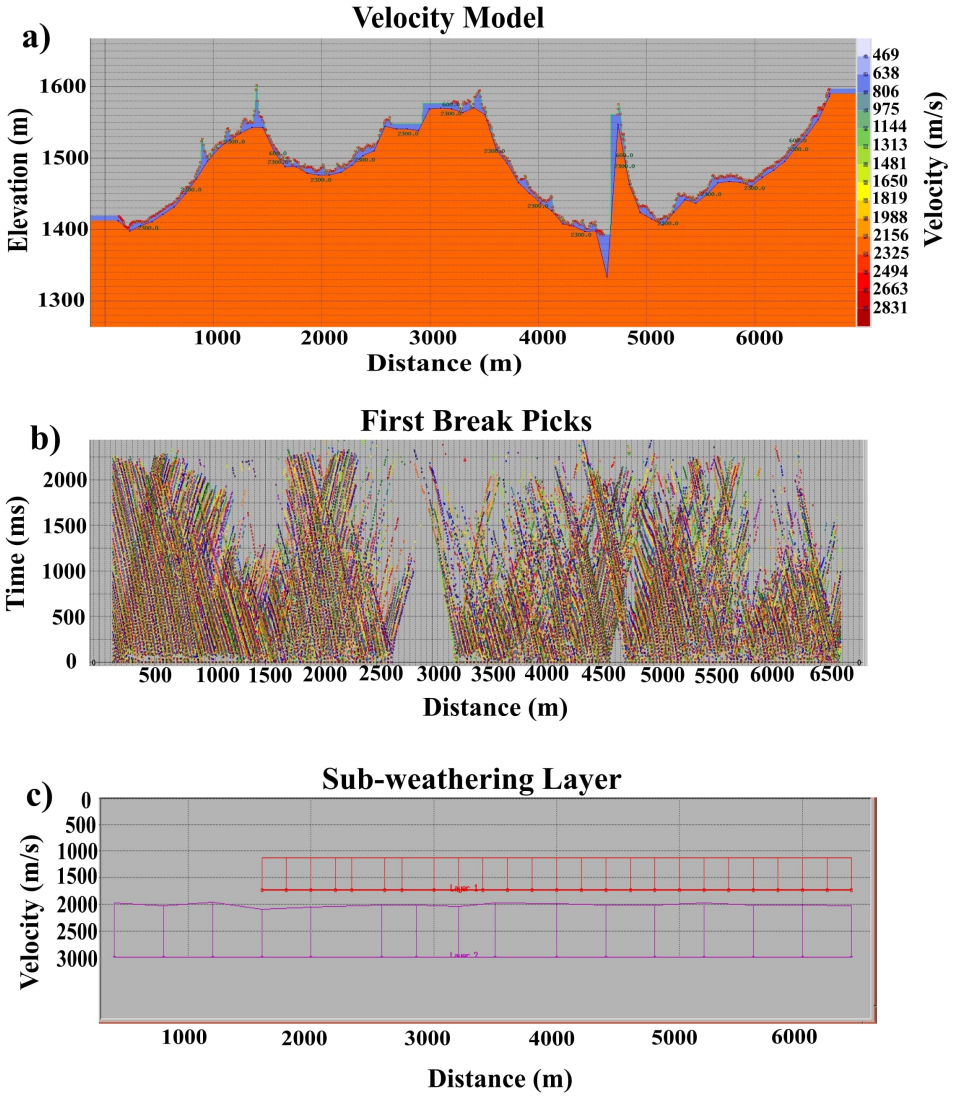

Figure 4.11: (a) Velocity model window obtained for the initial velocity model. The structure of the subsurface is shown in elevation, with the strata being color-coded according to the speed at which they move. (b) First break picks for each shot gather. (c) The model of the sub-weathering layer.

An iterative process was also performed, where the inversion was allowed a few iterations to complete (Figure 4.12). After that, tests with various parameters were run on the model. This was achieved by allowing for a more intricate depth or velocity structure or by expanding the allowed range of layer-level velocity variations. The objective was to minimize the RMS difference between the observed first break picks and the predicted first arrival times (Woodward, 1992; Wang et al., 2016). For each iteration, the changes

were monitored.

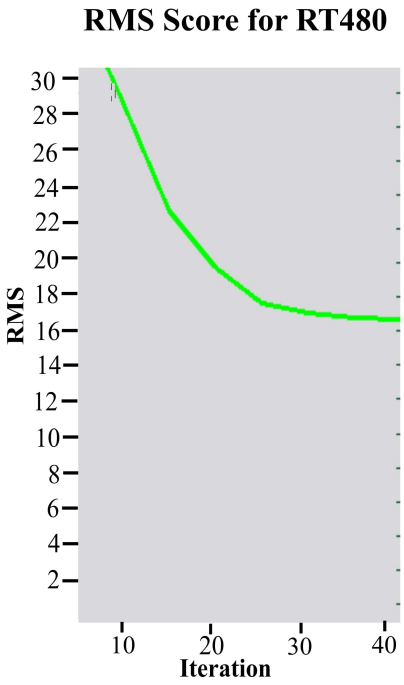

Figure 4.12: Root mean square (RMS) calculation graph. This graph shows the process followed to quantify the root-mean-square value contrast between the calculated first break picks and a general model interpolated using the processing software.

There was a root-mean-square discrepancy between the first break picks that were supplied and the ray-traced inversion outcomes for each iteration when the inversion procedure was executed. This had the potential to make wrong interpolations in the refraction velocity model. Refstat2D makes small but steady changes to the velocity and geometry to bring that RMS value down with each cycle. The RMS usually began at approximately 40 and decreased to roughly after six iterations, with all criteria satisfied.

When a stable model was achieved, below 20 ms, the static shifts were applied to the data using a process flow so the computed velocity models with the relevant adjustments could be part of the entire dataset. For this study, an RMS value of 20 ms was achieved. When the near-surface velocity and elevation corrections were combined, the refracted and direct arrivals coming from the low-velocity yielded a linear shape giving an indication of whether a sufficient correction has been done. Figure 4.13 shows plots of peg numbers against two-way travel time for elevation statics results (Figure 4.13 (a)), residual statics corrections (Figure 4.13 (b)), and total statics corrections (Figure 4.13 (c)).

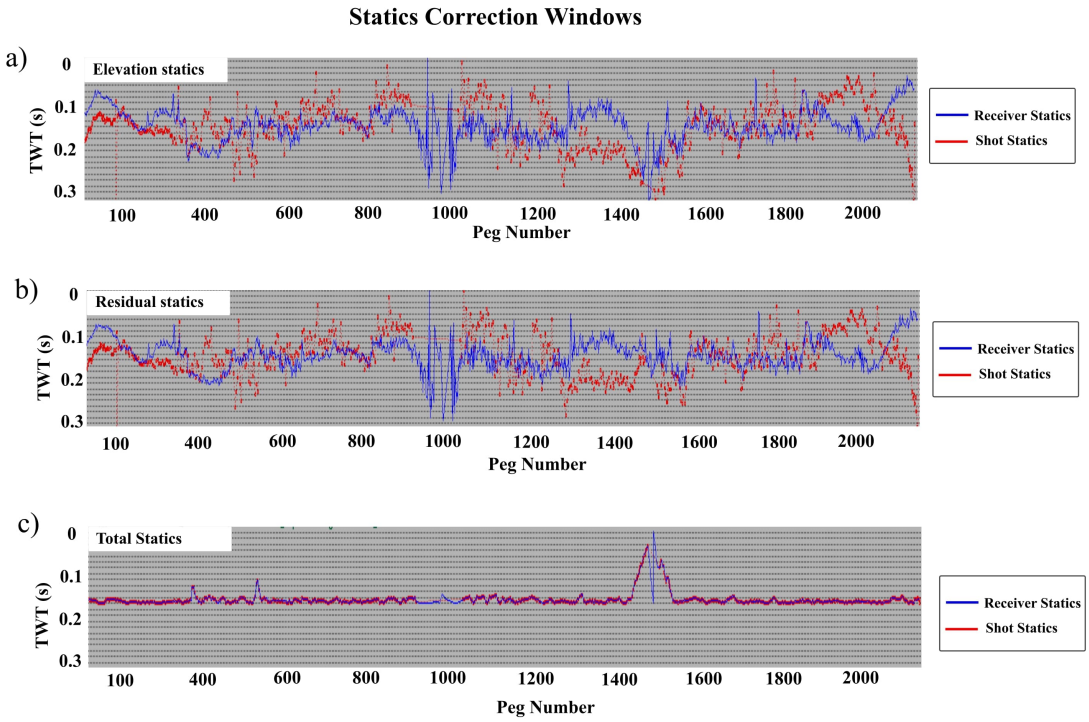

Figure 4.13: (a) Elevations statics. (b) Residual statics. (c) Total statics. These are the static view windows for the seismic data. Receiver statics (blue) and shot statics (red) are shown across all windows. The total statics obtained (c) were by merging the model-based and the residual statics corrections represented by (a) and (b) respectively.

Following the application of corrections calculated through the various tools outlined previously, the dataset underwent a transformative enhancement. This meticulous correction process was pivotal in repositioning both reflections and refractions to their accurate elevations, thereby aligning them more closely with their true subsurface origins. The raw data, as initially captured, exhibited discrepancies in the positioning of these seismic events, as evident in Figure 4.14 (a). This figure distinctly showcases a raw shot gather from the dataset prior to the implementation of static corrections, where one can observe the irregular formations presented by the primary waves (indicated by red arrows) and the hyperbolic reflections (marked by blue arrows).

These irregularities in the waveforms were effectively rectified post-correction, resulting in a more coherent and interpretable seismic image. Figure 4.14 (b) and (c) offer a visual representation of the substantial improvement in the wave shapes following the application of floating datum and total static corrections, respectively. These corrected images not only facilitate a more accurate analysis of the subsurface but also enhance the reliability and precision of the subsequent interpretative processes undertaken by

geoscientists.

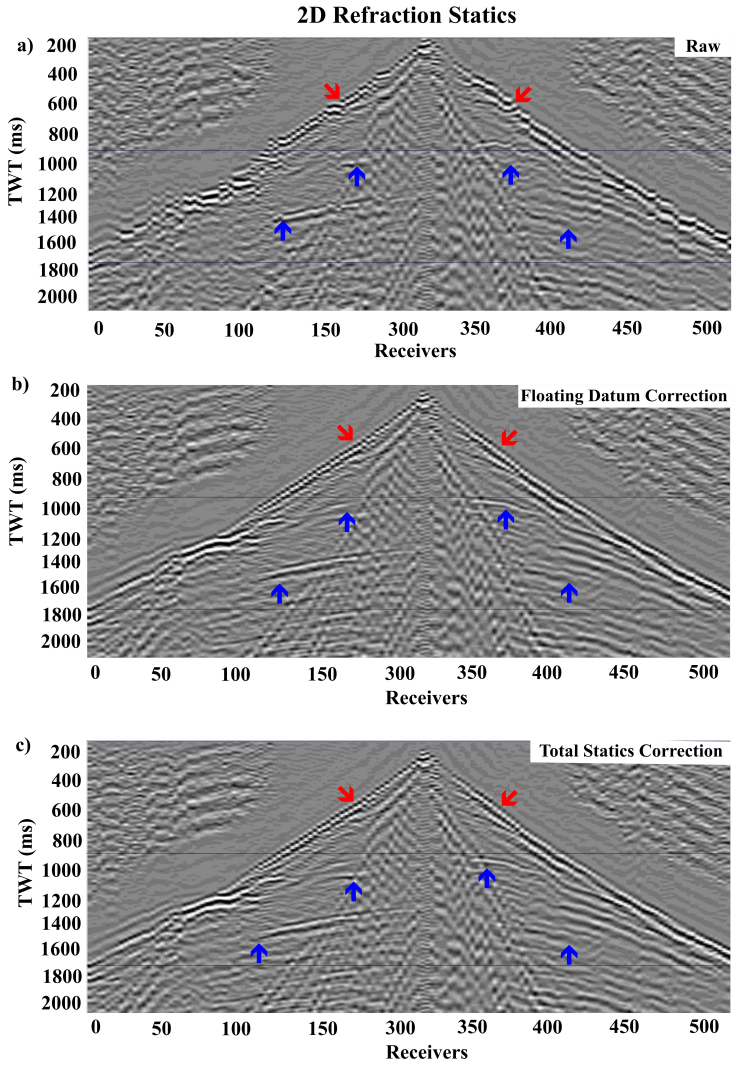

Figure 4.14: Results of applying the total corrections on the shot records is shown in this figure. (a) The original shot gather, (b) The shot gather after applying floating datum correction, and (c) The shot gather after applying total statics corrections. Primary waves (red arrows) and hyperbolic reflections (blue arrows) are the target events for correction and have been corrected sufficiently.

4.4.6 Noise Suppression

Refraction Muting

After the near-surface velocity changes have been addressed, the information provided by the refracted and direct arrivals is no longer helpful. The intensity of these events might produce artifacts when it comes to the use of certain signal processing algorithms such

as frequency filters; thus, one needs to choose a mute to get rid of them. The mute was automatically repeated on both the positive and negative offsets and interpolated from the points that were isolated as selections were made. Through the use of a process flow, the mutes were applied in an automated fashion to every shot gather. Figure 4.15 (a) is an example of a shot gather before muting and Figure 4.15 (b) shows the shot record after applying surgical mutes.

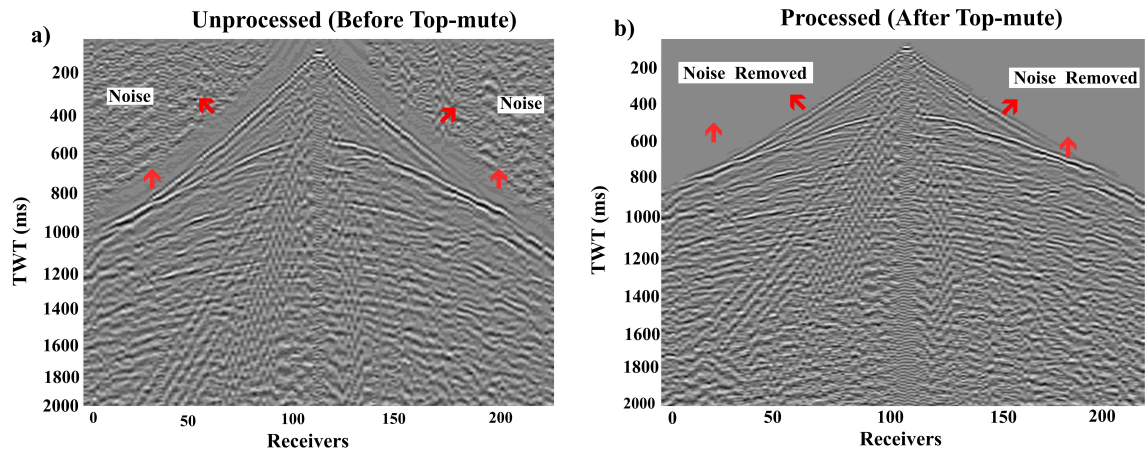

Figure 4.15: (a) A shot gather before applying a top mute. (b) The same shot gather after applying a front mute. The red arrows in both sub-figures show the noise removed using the muting process.

Frequency-Wavenumber Filtering

The process of handling the "ground roll cone" energy is crucial for enhancing the clarity and accuracy of seismic data interpretation. The "ground roll cone" energy, characterized by its distinct noise cone with velocities ranging from 850 to 900 m/s, often obscures the reflected events within its range, making it challenging for geophysicists to analyze the subsurface structures effectively. By meticulously measuring the apparent velocity of the noise cone in each shot, one can quantify the extent of its interference with the primary seismic signals.

The removal of this disruptive energy was achieved through careful adjustments to the frequency spectrum of the shots. Specifically, every set of 20 shots undergoes a precise modification process where the high-frequency ground roll signals are eliminated. This is done by cropping the signals with a calculated dip ranging from approximately 16 to 20 ms/trace, effectively isolating and removing the noise generated by the ground roll cone. The raw data in Figure 4.16 (a) is contrasted by the adjusted frequency spectrum in Figure 4.16 (b), which offers a cleaner and more accurate representation of the seismic

data. This allows for a more reliable analysis of the reflected events.

This approach to noise reduction not only enhances the visibility of reflected events but also significantly improves the overall quality of the seismic data collected. The ground roll cone, with its characteristic low-frequency energy, often masks subtle signals that are imperative for detailed subsurface imaging and analysis. By systematically removing this pervasive noise, one can access a clearer picture of the geological layers beneath the surface. The refined data, free from the clutter of ground roll noise, facilitates a more straightforward and accurate interpretation process.

This process is particularly vital in areas where the geological structures are complex, and the reflected signals are faint. With the noise meticulously removed, the data becomes a more reliable tool for making informed decisions in exploration and extraction activities, ultimately leading to more efficient and successful operations in the field. The noise removal process, therefore, is not just a technical necessity but a strategic enabler that supports the broader objectives of geophysical exploration and study.

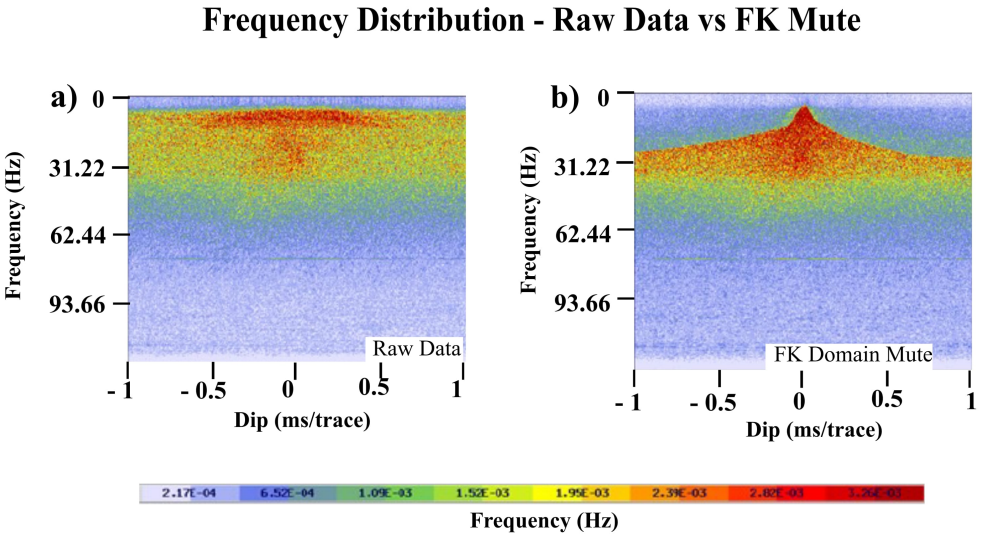

Figure 4.16: (a) The frequency-wavenumber (f-k) showing the original data. (b) Data after applying the f-k domain mute in the noise cone.

In addition to removing noise using a refraction top mute, f-k filtering was also used to remove the ground roll signals efficiently. Figure 4.17 (a) shows the selected raw shot gather before frequency filtering while Figure 4.17 (b) shows the result of applying the frequency transformation on the selected gather. This transformation was applied across all the shot records that make the profile. The bandstop filter was also used to remove noise potentially related to unwanted electrical signals, which are evident on the frequency

spectrum graph as spikes, Figure 4.17 (c). Moreover, Figure 4.17 (d) shows the resulting frequency spectrum graph after applying the frequency transformations.

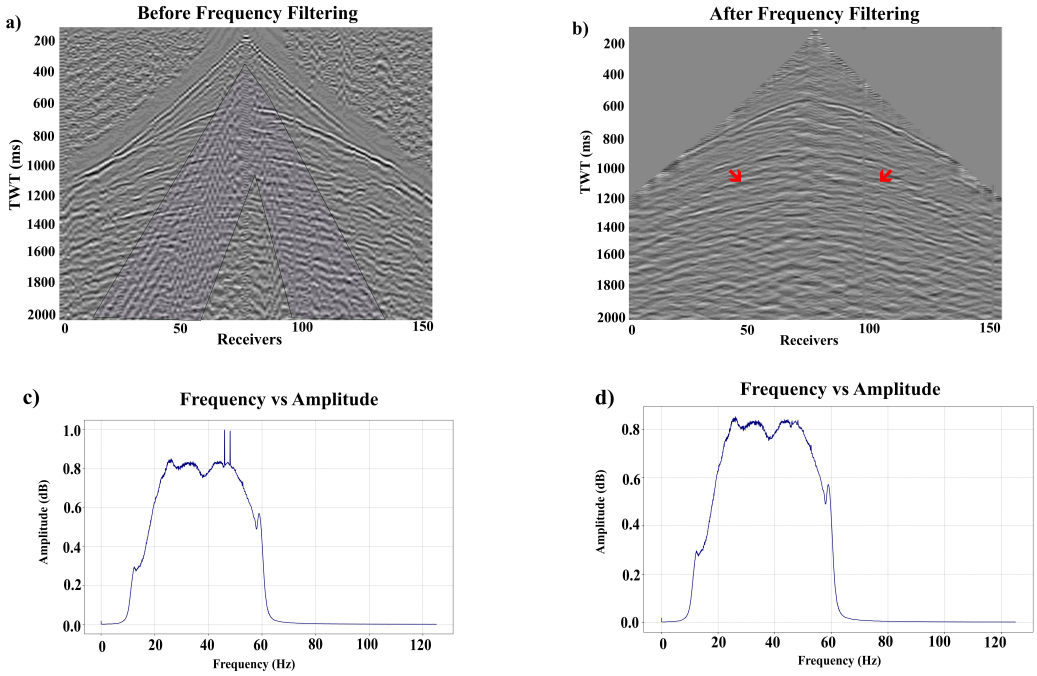

Figure 4.17: (a) A shot gather before applying an f-k (frequency-wavenumber) and a BS (band stop) filter. One can observe a ground roll cone (highlighted in purple). (b) The same shot gather after the application of f-k filtering, where ground rolls are removed. (c) Frequency spectrum graph with a very sharp spike between 45 Hz and 50 Hz. (d) Frequency spectrum graph after applying a bandstop filter. The spike on the frequency spectrum has been eliminated.

4.4.7 Pre-stack Deconvolution

The main aim of deconvolution is to compress any reverberant part of the wavelet, such as short-period multiples, and to change the wavelet shape, whitening it so that it has more frequencies and a sharper pulse. One important filter that is used to implement deconvolution is the optimum Wiener filter. This filter aims to produce an estimate of the desired signal by linear time-invariant filtering of the observed noisy signal. The filter is designed in the frequency domain and is optimum in the mean square error (MSE) sense, meaning it minimizes the average of the squared differences between the estimated and true signals (Yilmaz, 2001, p. 179). The seismic wavelet may be converted into any form that is required by using the Wiener filter. For instance, a Wiener filter, which functions in a manner very similar to that of the inverse filter, may be developed to

transform a seismic wavelet into a spike (Idier and Goussard, 1993). After analyzing the reverberations using autocorrelation functions, different types of deconvolution processes were applied to selected shot gathers from the pre-processed seismic data.

These processes were used to define different gaps and operators. To be more explicit, a deconvolution widow file was generated, and in this particular instance, one can adjust the size of the deconvolution gap based on a loop structure. This indicates that a unique deconvolution algorithm was used for each value of the loop's repeat parameter. It is important to keep in mind that a gap of 0 indicates a single sample or "spiking" deconvolution. The gap length of every 10th shot record was computed initially where the resulting values were automatically stored in a spreadsheet integrated with in the processing software. Subsequently, a processing flow including deconvolution then was applied across the datataset. Figure 4.18 (a) and (b) show a selected shot record before and after the application of deconvolution respectively, while Figure 4.18 (c) and (d) show the frequency spectra before and after deconvolution.

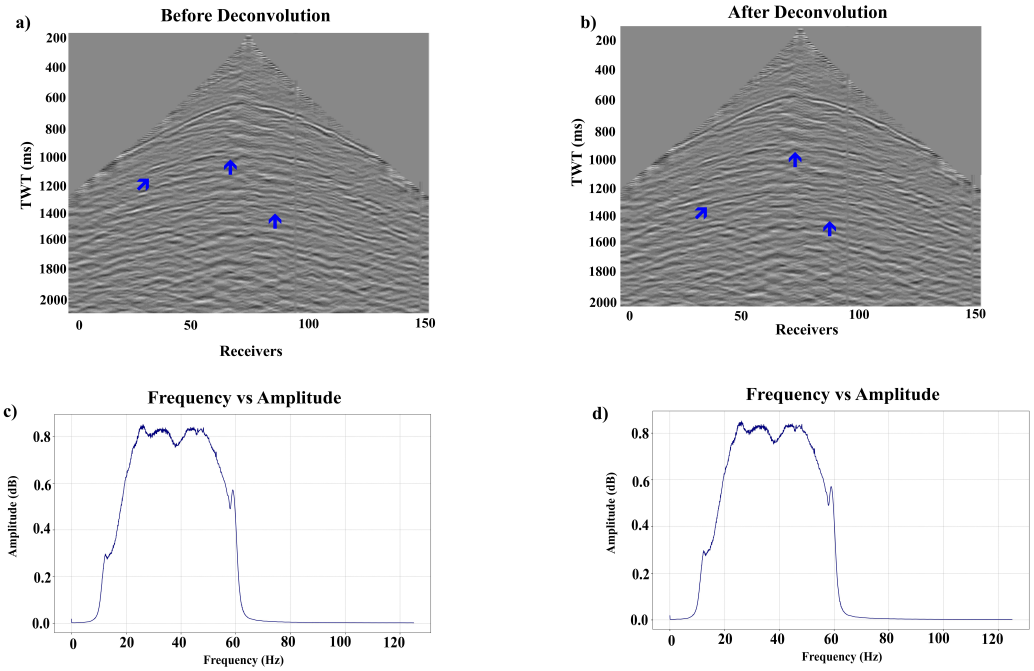

Figure 4.18: (a) A shot gather before applying deconvolution. (b) The same shot gather after applying deconvolution with a gap length of 36 ms. This length varies amongst different shot gathers. It is evident that wavelets are compressed and short-period multiples are reasonably eliminated (as shown with blue arrows). (c) The frequency spectrum graph of the record before deconvolution. (d) Frequency spectrum graph after deconvolution.

4.4.8 Velocity Analysis

Various moveout adjustments to the data were tested to achieve this processing. A measure of the trace-to-trace cross-correlation with various NMO (Normal moveout) corrections applied is shown in the form of a sequence of corrected gathers, a mini-stack, or a semblance display. The analysis was achieved using the CVA (constant velocity analysis) feature and there are two ways to do it, constant velocity and variable velocity modes Figure 4.19 (a)-(c) shows the raw stack with velocity values, a velocity model with calculated velocity values and the resulting velocity model without velocity values respectively.

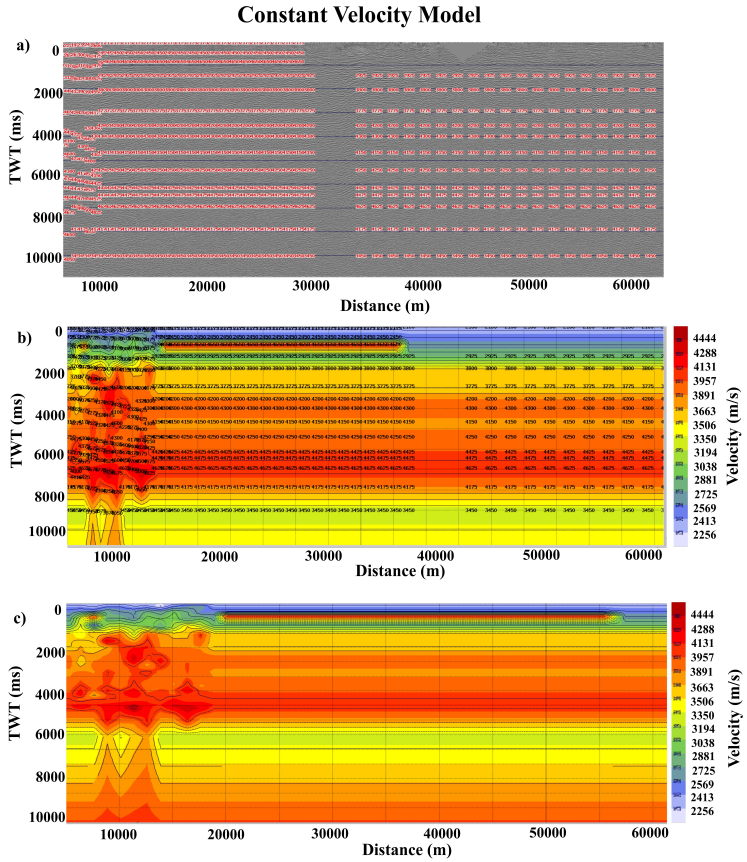

Figure 4.19: Velocity model for the seimic profile. The primary and secondary wave velocities of all the rock types that the profile covers were approximated using time values of reflections using a semblance approach. They were saved as NMO (Normal moveout) files. (a) Stacked section with estimated velocities across the entire profile. (b) The resulting velocity model with their estimated values. (c) The resulting velocity model.

In this case, the variable velocity approach was followed. Here, the velocities used in the semblance, stack, and gather displays are calculated around a central function for every CDP location in the stack. As a result of performing this process, the approximate velocity values for targeted reflections were calculated across the entire stack with CDP intervals.

4.5 Stacking

Stacking is the second principal process when processing seismic data (Yilmaz, 2001, p. 48). It is essential for enhancing seismic data's S/N and image quality (Kiran, 2005). One of the most commonly used stacking methods is the common midpoint (CMP) stacking and is used in this study. Stacking can attenuate uncorrelated noise remarkably by using repetition in CMP recording, thereby incrementing the S/N. Stacking can also reduce a large segment of the coherent noise within data, such as guided waves and multiples. Figure 4.20 is the stacked section of the entire 16 s TWT section of the seismic data. It was normal moveout (NMO) corrected using the velocity model generated during velocity analysis. Furthermore, before stacking, the primary velocity function was used to do the normal moveout (NMO) correction for the profile.

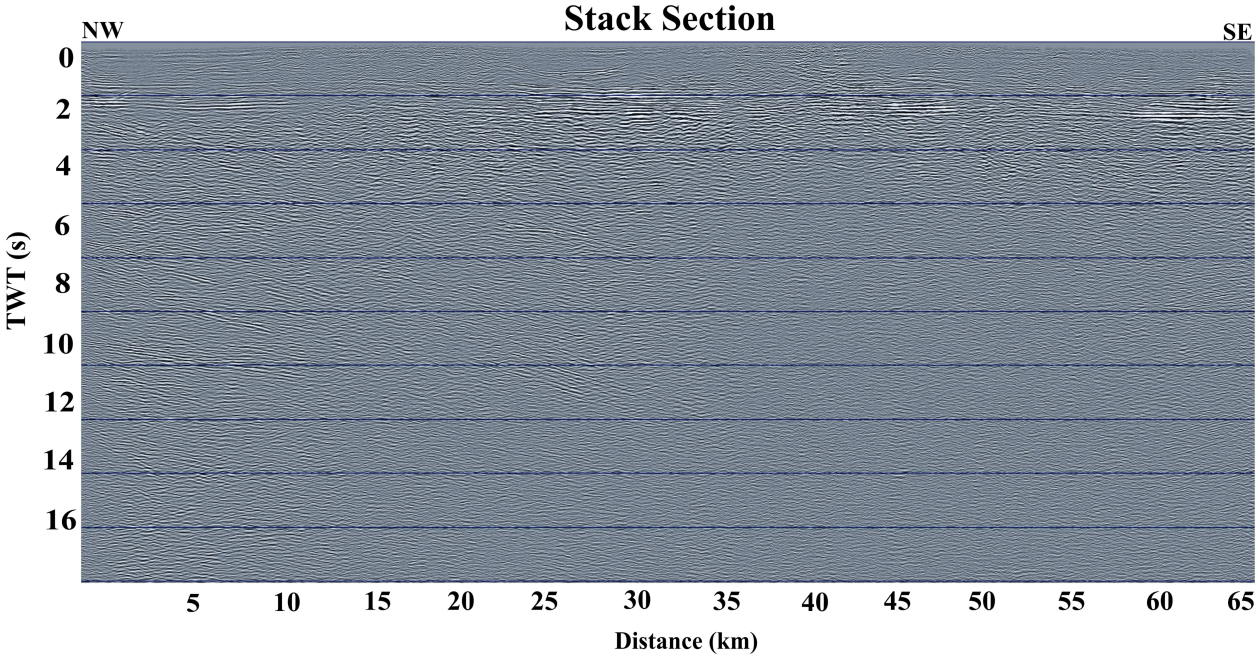

Figure 4.20: Stacked section of the seismic profile RT480. This stack was Normal moveout (NMO) corrected using the velocity model generated from velocity analysis. No migration applied.

4.6 Post-Stack Processing

4.6.1 Applying Seismic Migration

Migration procedures depend on an operator who alters the original picture in both positive and negative ways. This may result in artifacts around the margins (sides and bottom) of the seismic section as well as if there is significant fluctuation in the trace amplitudes. These effects have to be mitigated first. In this study, a "rolling gate balance" with a sequence of 1000 ms windows that are 50% overlapping was used to address the trace-to-trace amplitude variance. Compared to an AGC, which may potentially have a detrimental effect on the migration operator. Figure 4.21 shows the final output after applying Kirchhoff post-stack time migration on the seismic data.

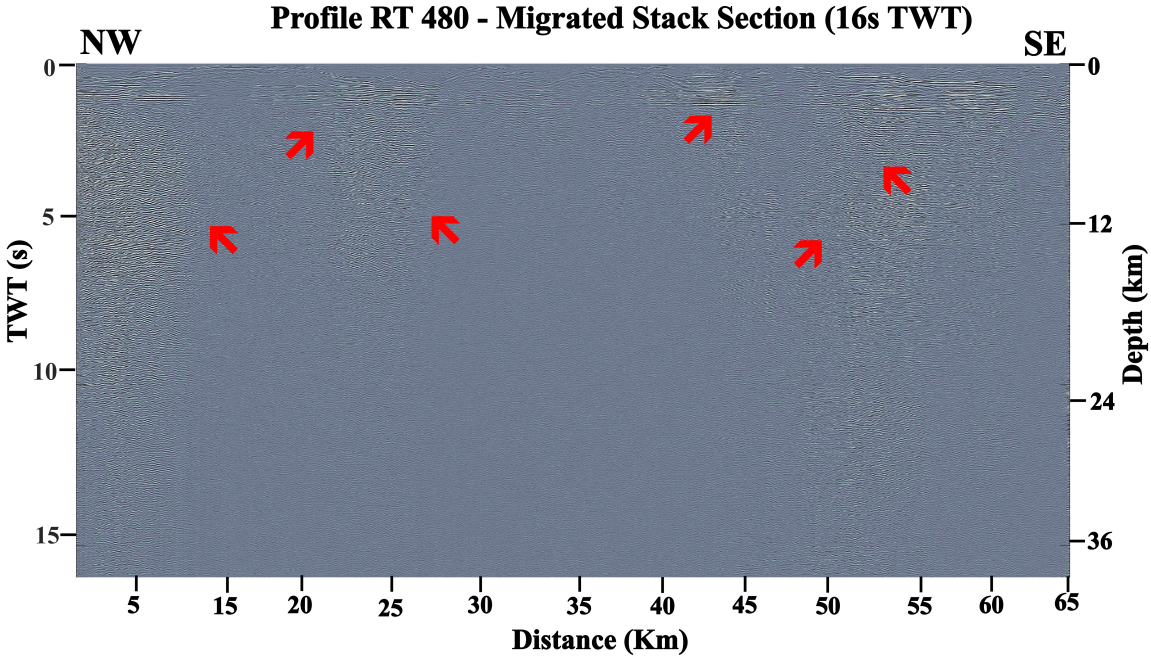

Figure 4.21: Stacked section of the seismic data. The red arrows show that the reflections were moved to their true depths (red arrows). Kirchhoff migration with a migration velocity of 5000 m/s was applied to achieve this image.

In this step, balance gates were stored within an integrated spreadsheet file and were applied on the stack first. After applying these scaling operations, a processing flow was used to create and migrate the stack using an imaging module. Through practical experimentation and comparative analysis of various migration techniques and velocities, it was determined that a 2D Kirchoff time migration with an average velocity of 5000 m/s was the most precise for this case.

Figure 4.22 zooms into the migrated seismic data to demonstrate the improvement made with the migration process where Figure 4.22 (a) is the raw stack, with displaced reflections (red arrows) and Figure 4.22 (b) is the stack after applying migration. One can observe that the reflections (red arrows) are geometrically relocated to their true position in the subsurface rather than the location where the recording occurred on the surface.

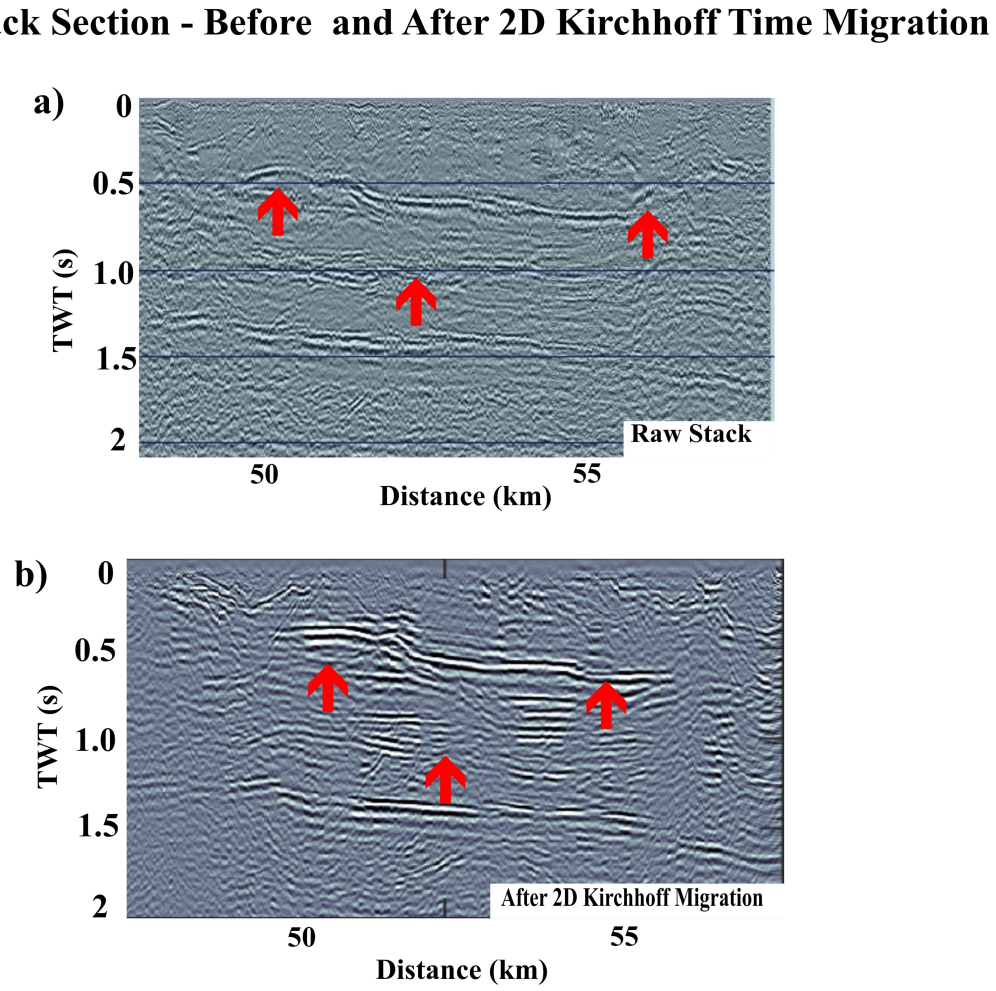

Figure 4.22: (a) A segment of the raw stack, with displaced reflections (red arrows). (b) The segment after applying 2D Kirchhoff migration to the seismic data. Kirchhoff migration with a migration velocity of 5000 m/s was used in this case, the reflections (red arrows) are geometrically relocated to their true position.

4.6.2 Synthetic Seismogram

A synthetic seismogram was generated to outline the relationship between the well and seismic data to allow one to associate geological layers with seismic events in the data. A record of the sonic velocity was taken for well WE1/66 and it showed a consistent speed

of 5000 m/s. As mentioned earlier, this velocity log was recorded by SOEKOR (Southern Oil Exploration Corporation) in the 1970s (Rowsell, 1976).

Ultrasonic velocities and densities of different lithological units of the basin were calculated under laboratory conditions (Coetzee, 2018). These results were therefore used in this study to calculate synthetic seismograms of the data for multiple pairs of these lithological units along well WE1/66. A custom Matlab program was used to plot the synthetic seismogram (Figure 4.23).

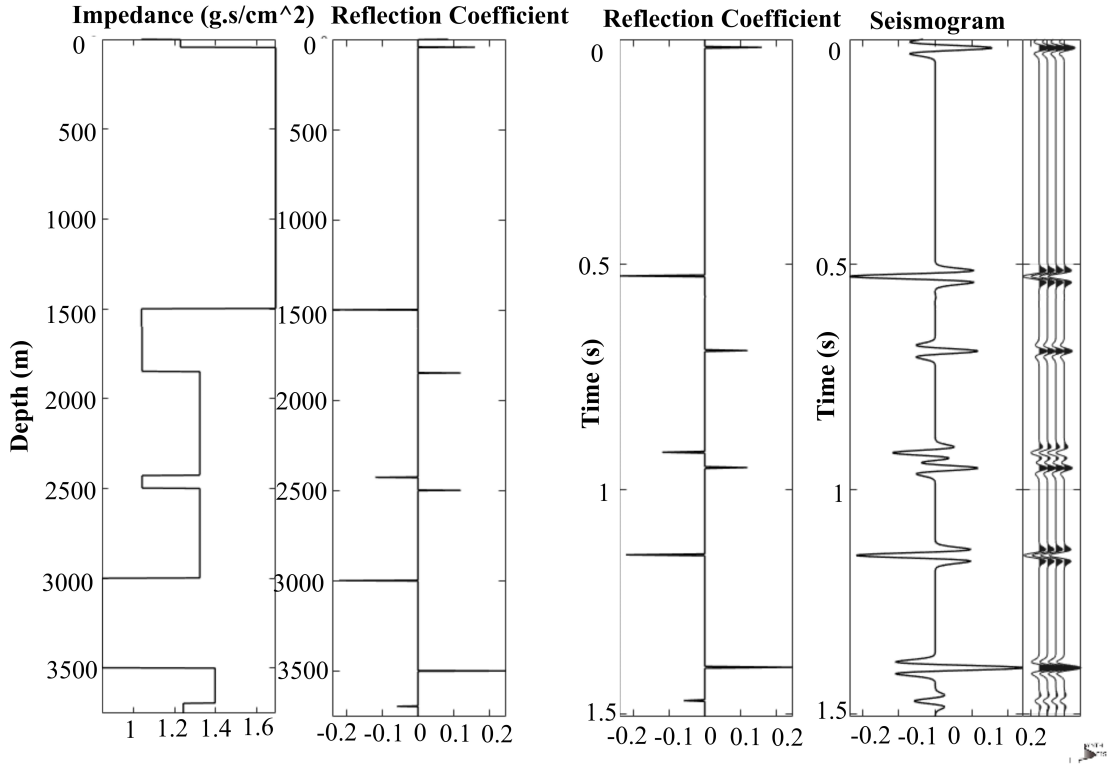

Figure 4.23: This synthetic seismogram was created using a sampling rate of 2 ms and a dominating frequency of 30 Hz. It contains characteristics of both minimum and maximum-phase wavelets. A synthetic seismogram helps us understand how seismic waves travel through different subsurface layers. They assist in interpreting stratigraphic features and identifying key seismic reflections. In this case, one can observe highly reflective events between 0.5 s and 1.5 s on the seismogram and they are associated to the geological boundaries present between 0.5 s and 1.5 s on the seismic section.

4.6.3 Correlating the Section With a Synthetic Seismogram

Computer-generated trace, often referred to as a synthetic seismogram, plays a pivotal role in the realm of geoscience. This tool is instrumental in helping geoscientists gain a

deeper understanding of how seismic waves travel through the Earth's subsurface. By simulating how these waves propagate, geoscientists can make more informed decisions about the Earth's internal structures and the materials they encounter. One of the primary uses of generating the trace is in the calibration and correlation of seismic data with well logs.

Well logs provide direct measurements of subsurface properties at specific locations, and when combined with seismic data, they offer a comprehensive view of the subsurface. This synergy allows for a more accurate interpretation of stratigraphic features, which are the layers and formations of rocks and sediments beneath the Earth's surface. Understanding these features is crucial for determining the history and processes that have shaped a particular region. Additionally, the computer-generated trace serves as a reliable benchmark for assessing the quality of seismic data that has been acquired. In the world of geoscience, the accuracy and reliability of data are paramount. By comparing the synthetic seismogram with the actual acquired data, geoscientists can identify any discrepancies or anomalies, ensuring that the data they work with is of the highest quality.

Moreover, in the high-stakes arena of exploration, where companies invest significant resources in search of valuable resources like oil and gas, the computer-generated trace acts as a risk mitigation tool. By providing a clearer and more detailed understanding of subsurface structures and conditions, it allows exploration teams to make more informed decisions. This clarity reduces the uncertainties and risks associated with drilling and exploration activities, ensuring that efforts are directed in the most promising and safe directions.

Figure 4.24 demonstrates a correlation process of the seismic data with the generated synthetic seismogram. Because it was challenging to identify the base of the Beaufort Group through field and well logs, it was instead determined on the seismic section as the uppermost layer of a series of robust reflectors (with a two-way travel time of 1.15 - 1.35 seconds and a depth of 2.6 - 2.9 km) (Scheiber-Enslin et al., 2021). A distinct reflection should also indicate the boundary between the Karoo Basin's base and its underlying Natal basement. The reason for this could be explained by the difference in acoustic impedance between the Carboniferous shales and tillites on one hand, the Archean basement of the Kaapvaal Craton in the northwest, and the granite-gneiss basement of the Natal Mobile Belt in the southeast on the other.

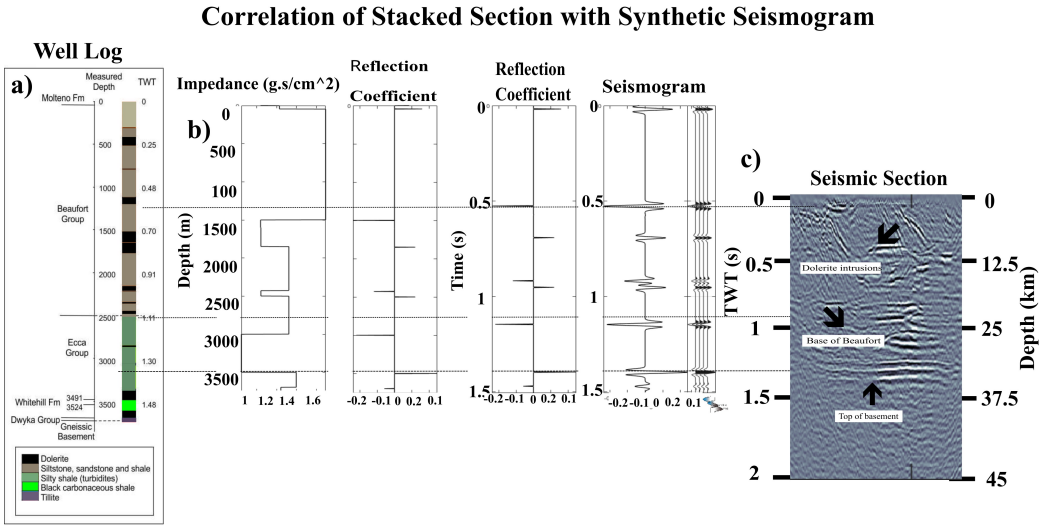

Figure 4.24: (a) Well log WE 1/66 (Scheiber-Enslin et al., 2021). (b) The synthetic seismogram was generated using velocity, density, and depth values observed in the area to calculate impedance and reflection coefficient. (c) A segment of the seismic data showing stratigraphic boundaries. One can generally observe that the depths of reflections from the stack correlate well with reflections obtained from the synthetic seismogram.

It was challenging to identify the precise distinction between the basin and the basement since there exist a few robust reflectors (possibly due to loss of seismic energy) close to the lower part of the Ecca Group. Because there are only a few dolerite sills that have intruded the basement in the Karoo Basin, it was decided to use the top of the basement as a reference point at the beginning of the chaotic reflectors.

This means that it was assumed that all of the strong reflectors are contained within the Ecca Group. This reliability of picking is reinforced by the depth value obtained from well log WE1/66 (Scheiber-Enslin et al., 2021). The Whitehill Formation and the unique tillites found in the Dwyka Group meet at the lower part of well WE1/66, but they are both thin, measuring around 33 m and 35 m, respectively (Scheiber-Enslin et al., 2021). As a result, the seismic data, which have a resolution limit of approximately 43 m, cannot distinguish between them.

4.7 Summary - Methods

When processing the data, the pre-stack steps that were taken include amplitude recovery done on multiple processing stages, manual first break picking, static corrections, which involved floating datum, residual statics, refraction statics, and total statics, trace muting, frequency and frequency-wavenumber filtering and predictive deconvolution. Floating da-

tum refraction statics were done during geometry setup using a fixed datum elevation of 1600 m and a replacement velocity of 6000 m/s. Refraction statics correction required first break picking of the first arrivals first. The picking of these arrivals was done using a manual approach. Once all shots were picked, a processing module provided by the software was utilized to apply a Generalized Linear Inversion (Woodward, 1992) approach to calculate the refraction statics by inverting the picked first break arrivals for each shot record.

The RMS error of the final inverted model was at 20 ms. The first arrivals were also used to generate a refraction tomography. Frequency and frequency-wavenumber filtering was also done to eliminate unwanted frequencies that are either higher or lower than the desired frequency intervals, such as high amplitude ground-roll signals. The frequency spectrum of every 20 shots was analyzed to remove these high-frequency signals. This process required cropping the signals with a dip of approximately 16 to 20 ms/trace.

A bandpass filter was used to eliminate signals outside the Vibroseis sweep range, as was a notch filter to reduce a vertical 50 Hz spike caused by electrical noise that appeared throughout the profile. Predictive deconvolution was applied before stacking. The initial zero-crossing of the autocorrelogram was used as the gap length for every 10th shot gather and the operator length for predictive deconvolution. The intermediate shot gather' gap, and operator lengths are automatically interpolated by the processing software. An average gap length of 36 ms and an operator length of 30 ms were used.

Velocity analysis was performed using the constant velocity stack approach where possible seismic velocity values of lithologies at the survey area are assigned to the respective reflections obtained on the generated zero offset stack. NMO correction was also applied using velocities that range between 4200 and 6700 m/s, and velocity inversions induced by dolerite intrusions required high-velocity values (5712 m/s). After performing velocity analysis, the shot gathers were stacked. Residual statics corrections were also applied for two cycles after stacking the data. Post-stack Kirchhoff time migration was also applied on the data to improve imaging.

5. Results and Discussions

5.1 Seismic Resolution Limit

Understanding all factors that influence seismic resolution is crucial for a comprehensive analysis of the data. The impedance contrast, which is the difference in acoustic impedance between the target and host rock, significantly affects the data's clarity and precision. A higher impedance contrast often results in clearer images of the subsurface formations, making it easier to distinguish between different geological layers. The target's shape and thickness also play a pivotal role, as these characteristics can either enhance or obscure the seismic signals, thereby affecting the interpretability of the data.

Furthermore, the design of the survey and the type of instruments used are fundamental in capturing high-resolution data. A well-planned survey design, coupled with advanced, sensitive instruments, can effectively minimize noise levels and capture more accurate and reliable seismic data. This careful consideration of various influencing factors ensures that the gathered data is of high quality, providing a reliable basis for interpreting the geological formations present in the subsurface (Manzi et al., 2014; Scheiber-Enslin et al., 2014; Westgate et al., 2020).

The seismic resolution limit is determined by three factors: the dominant frequency of the data, the seismic velocity of the targets, and the prominent wavelength (λ) in the data. In the seismic profile, at a depth of around 3 km, the reflected signal has a dominating frequency of approximately 30 Hz. If we assume that the mean velocity is 4500 m/s, as calculated by aggregating seismic velocities of the different layers observed in the area, and ultrasonic velocities from similar rocks measured by Coetzee (2018), then the dominant seismic wavelength (λ) is 150 m, and the tuning thickness ($\lambda/4$) is approximately 37.5 m (Widess, 1973).

If the tuning thickness is less than a quarter of the dominant seismic wavelength, then the top and bottom of geological features may not be resolved, e.g., Rayleigh criteria of

the vertical resolution limit. Smaller features as little as ($\lambda/32$) however may still be recognized, though the detection will rely on the diffractions and not only on the seismic amplitude (Manzi et al., 2014; Malehmir et al., 2018).

5.2 Comparing Legacy and Reprocessed Data

5.2.1 Technical Comparisons

The primary objective of this research is to determine whether using contemporary algorithms and techniques to reprocess the RT480 seismic profile can provide clearer insights into the structures of the area under investigation. Since the profile's acquisition in 1992, processing algorithms and workflows have advanced. Additionally, newer data, especially from magnetic and borehole studies, have become accessible, further aiding in seismic interpretation.

In general, the reprocessing of the seismic data has significantly improved the visualization of both stratigraphy and structural elements along the profile. This includes clearer delineations of the configuration of the sills and enhanced continuity of reflections associated with the sill structures and their configuration. Reflections occurring between layer boundaries have also been more distinctly captured.

The initial shot records and the migrated legacy stack data were provided in the SEG-Y format by Anglo Gold Ashanti. Unfortunately, there's no detailed account of the original processing workflow for the legacy data, except a list of brief processing steps presented in Table 5.1. The final results (i.e., stacked and migrated section) from this reprocessing work are compared with the final 1992 legacy seismic section. The old processing steps and related output could not be compared to the results from this study because they were not made available.

The seismic profile's irregular trajectory poses challenges to the clarity of seismic imaging (Adam et al., 1998). For instance, neglecting the profile's crooked layout, especially at its NW extremity, during the processing phase could result in steeply inclined reflectors not being depicted in the resulting stacked section due to misalignment in common depth point (CDP) collections. Yet, significant advancements have been made in refining 2D crooked line imaging in rocky terrains, particularly on a crustal level.

Various methods to enhance this type of imaging are explored in past studies, (e.g., Kim et al., 1992; Nedimovic and West, 2003). Table 5.2 shows the processing records

followed when reprocessing the data. Despite the many challenges, several contributing factors led to improved updated imaging. One of these factors is the consideration that the RT480 profile significantly follows a crooked path. Opting for the conventional crooked survey line approach was crucial in enhancing the quality of the imaging.

Another significant factor was the use of noise mitigation algorithms. For instance, the notch filter was employed to eliminate a prominent 50 Hz element (normally caused by electrical signals from power lines) from the data, and the bandpass filter was utilized to reduce frequencies outside the sweep range. These measures effectively reduced background noise in the reprocessed data, a step not evident in the legacy processing procedures.

Furthermore, the predictive deconvolution algorithm merits attention. The operator length used to process the legacy data was a mere 30 ms, which is substantially shorter than the 160 ms used for reprocessing. It's essential that the operator length be sufficiently long to encompass the entire primary wavelength, including its side lobes. The velocity analysis step was also pivotal. The stretch mute value of 130% used for the legacy data exceeds the 70% employed for reprocessing. This discrepancy could have resulted in the reprocessed data exhibiting a more refined normal moveout (NMO). A judicious application of a tighter stretch mute value can yield cleaner reflections.

Seismic migration is also one of the most important steps in improving imaging. The details of migrating the legacy data are not fully recorded. However, the reprocessed data was post-stack time migrated using the 2D Kirchhoff method where the NMO corrected velocity model obtained from constant velocity analysis was used as an input. A migration aperture size of 1400 m was utilized to accommodate the velocities that range from 4000 m/s to 5700 m/s.

Table 5.1: Summary of legacy processing sequence for profile RT480.

Procedures
Edit - Noisy trace removal and editing
Statics - Weathering statistics applied to floating datum
F-K filter - Full fan tapered f-k filter, full on at 2 000 m/s
Scale - Trace equalization and spherical divergence correction
Deconvolution - Minimum-phase-predictive deconvolution, operator length = 160 ms, gap = 24 ms
CMP Sort and NMO - Crooked line sorting and velocity-derived function stacks and gathers CMP interval = 25 m
Statics - Data corrected from floating datum to regional datum
Autostatics - Residual statics applied
NMO - Revised velocity applied with 130% stretch mute
Stack - Nominal 2400% stack with root mean compensation
Filter - Space variant band-pass filter applied 0-5000 ms
Residual Static Corrections - repeat NMO
Migration : 2D Kirchhoff

Table 5.2: Summary of reprocessing sequence for profile RT480.

Preprocessing
Demultiplexing **Reformatting** - From SEGD to SEGY **Amplitude Recovery** - AGC **Geometry Assignment and CDP bin** - sources and receivers assigned to each trace with a CDP size of 25 m **Floating datum correction** - fixed datum elevation of 1600 m and replacement velocity of 6000 m/s
Pre-stack Processing
First Break Picking - automatic and manual methods **Refraction Statics Correction** - two-layer model using first arrivals, RMS = 11 - 12 ms **Trace Muting** - Top mute using first arrivals **Bandpass Filter** - 50-60-160-170 Hz **F-k filter** - surgical mute with dip = 16 to 20 ms per trace **Velocity Analysis** - constant velocity stack **NMO corrections** - 4200 - 6100 m/s, stretch mute of 70% **Residual Static Corrections** - repeat NMO Stacking - Normal
Post-stack Time Migration : 2D Kirchhoff
Time To Depth Conversion - 1D constant velocity: 5500 m/s

5.2.2 Structural Comparisons

The seismic section, when observed up to 2 s two-Way travel time (TWT), reveals primary features that align closely with those detailed by De Wit and Tinker (2004). Specifically, the Beaufort Group is situated directly above the Ecca Group. Below the Beaufort Group, one can identify the Dwyka Group. A more comprehensive breakdown of these structures, including their intricacies and relationships, is provided in the interpretation section. Through reprocessing, the data have undergone significant refinement. This has resulted in sharper reflections and an enhanced signal-to-noise ratio, facilitating a more precise identification of these geological formations' locations.

Such refinements have paved the way for more accurate depth interpretation and more detailed visualization of smaller structural components. This includes features like layer boundaries and sills, which, in the legacy stack, were not as distinctly represented, espe-

cially in specific sections. For optimal visualization and given that the most pronounced enhancements are evident within this range, both sections are limited to 2 s TWT. Notably, there are discernible differences between Figure 5.1 (a) and Figure 5.1 (b). These variations are highlighted and further explored within the colored rectangles in Figures 5.2 and 5.3. One can also observe the frequency differences in Figure 5.1 (c) (High frequency with spikes) and Figure 5.1 (d) (Lower frequency with smooth values), which indicate a general reduction in noisy frequency content.

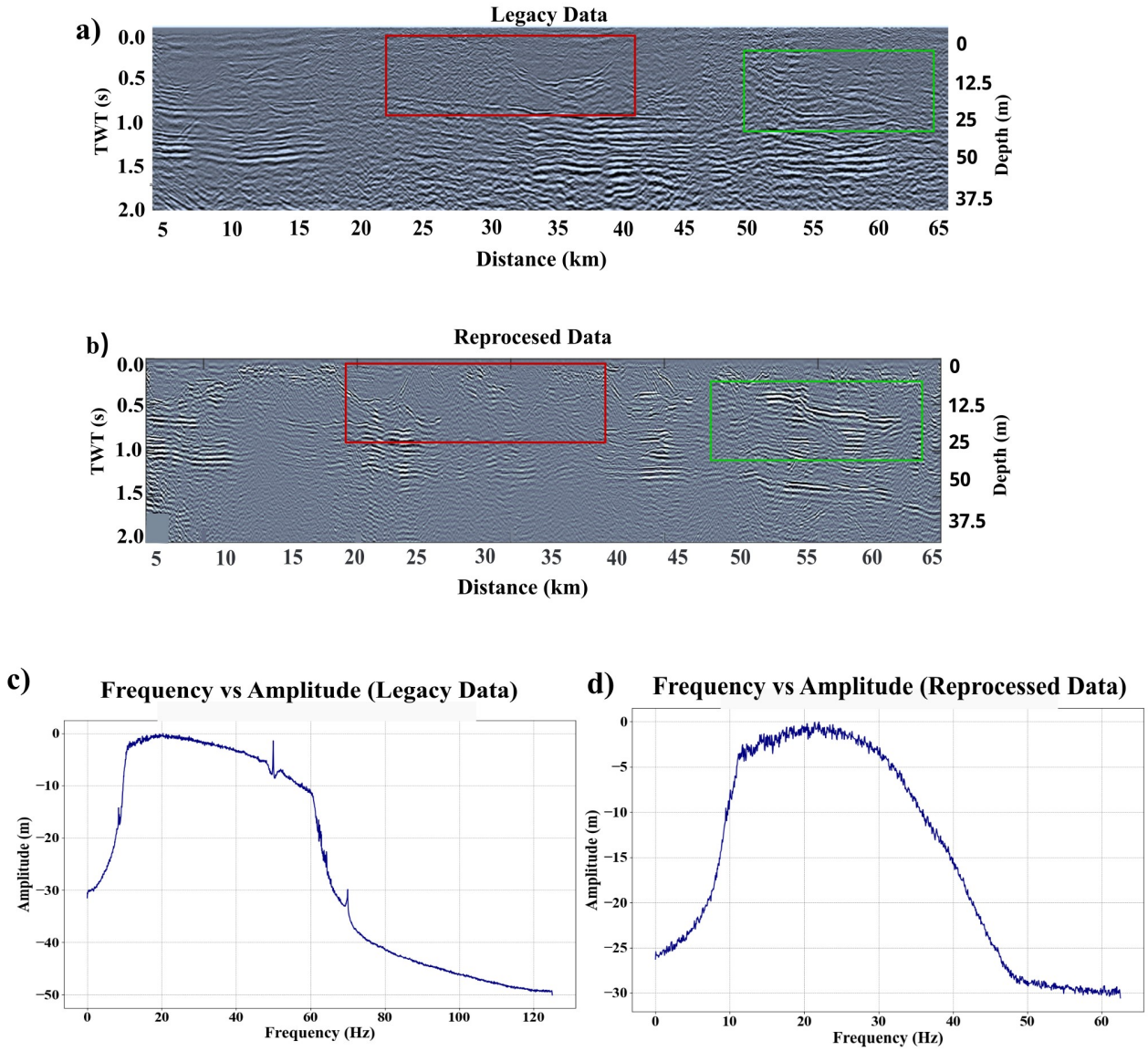

Figure 5.1: Comparing the original stack section (a) to the reprocessed stack section (b), areas with significant enhancements are highlighted in rectangles. Detailed views of these areas are presented in Figures 5.2 and 5.3. (c) Frequency spectrum graph of the entire legacy stack. (d) Frequency spectrum graph of the entire reprocessed data.

In Figure 5.2 (a) and (b), a distinct reflection is noticeable, which is associated with a sill structure. This reflection spans approximately between 0.5 two-way traveltime (TWT) and 0.9 TWT. In the legacy stack, represented by Figure 5.2 (a), this sill wasn't adequately visualized, as the reflections appear somewhat muted and less defined. However, a marked improvement is evident in the reprocessed data, depicted in Figure 5.2 (b). Here, the reflections associated with the sill are more pronounced and better defined.

This enhancement in clarity is further corroborated by the frequency spectra in Figure 5.2 (c). The reprocessed data exhibit a smoother frequency spectrum when juxtaposed with its legacy counterpart.

The observed enhancement in the reprocessed data can be attributed to the meticulous velocity analysis undertaken during the process. This careful analysis was instrumental when interpolating and creating the velocity model for the events present within the data. Shifting the focus to Figure 5.3 (a) and (b), these sections highlight the base of the Beaufort Group. The legacy section, represented by Figure 5.3 (a), struggles to provide a clear demarcation of this boundary. In contrast, the reprocessed data in Figure 5.3 (b) offers a lucid delineation of this boundary. This clarity in the reprocessed data is further supported by the smooth curve in Figure 5.3 (c), which stands in stark contrast to the more erratic curve from the legacy data.

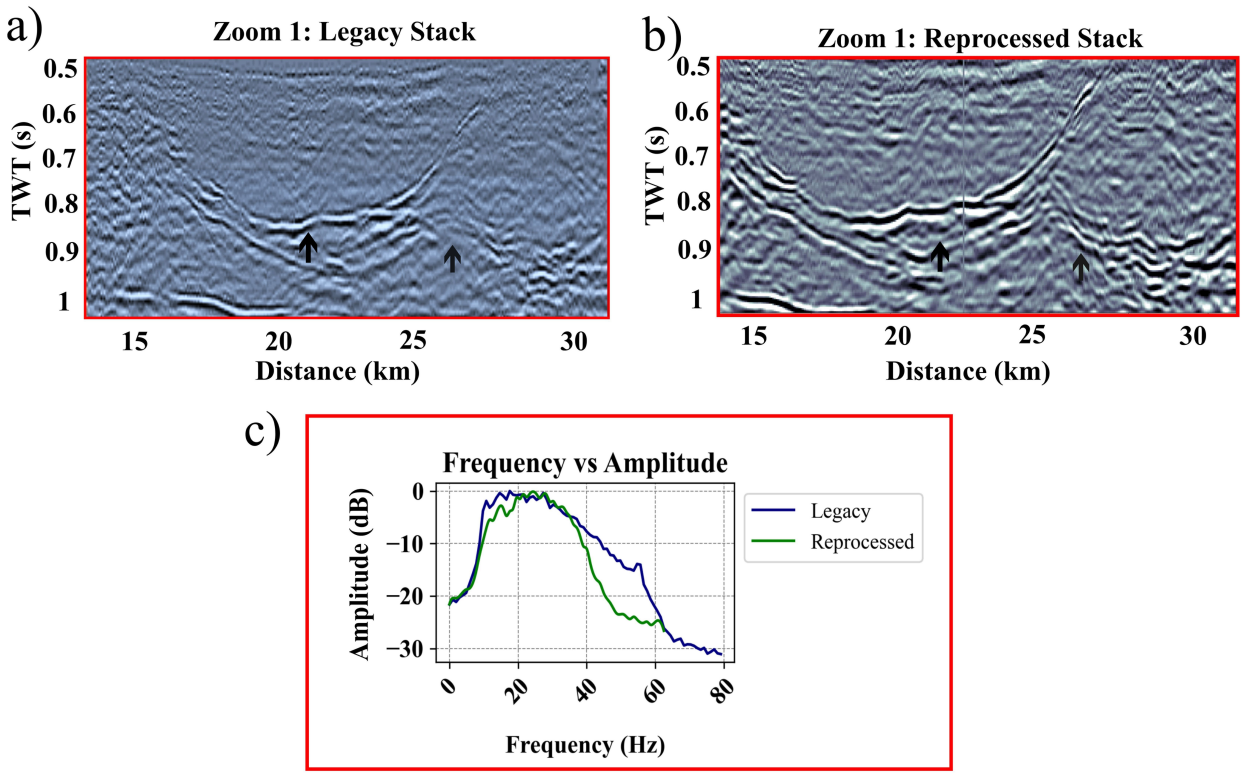

Figure 5.2: Close-up areas of the legacy stack (a) and reprocessed stack (b) with a frequency spectrum graph obtained for these particular sections (c). The reprocessed data (b) clearly image the geometry and continuity of the sills with increased quality as compared to the legacy one (a). This is shown using black arrows in the figure. The frequency trend of the reprocessed data is evidently smoother than the legacy data. The key observation here is that the higher frequencies on the legacy spectrum are adequately eliminated in the reprocessed section. The high frequencies on the legacy data are most likely related to noise that was not handled efficiently.

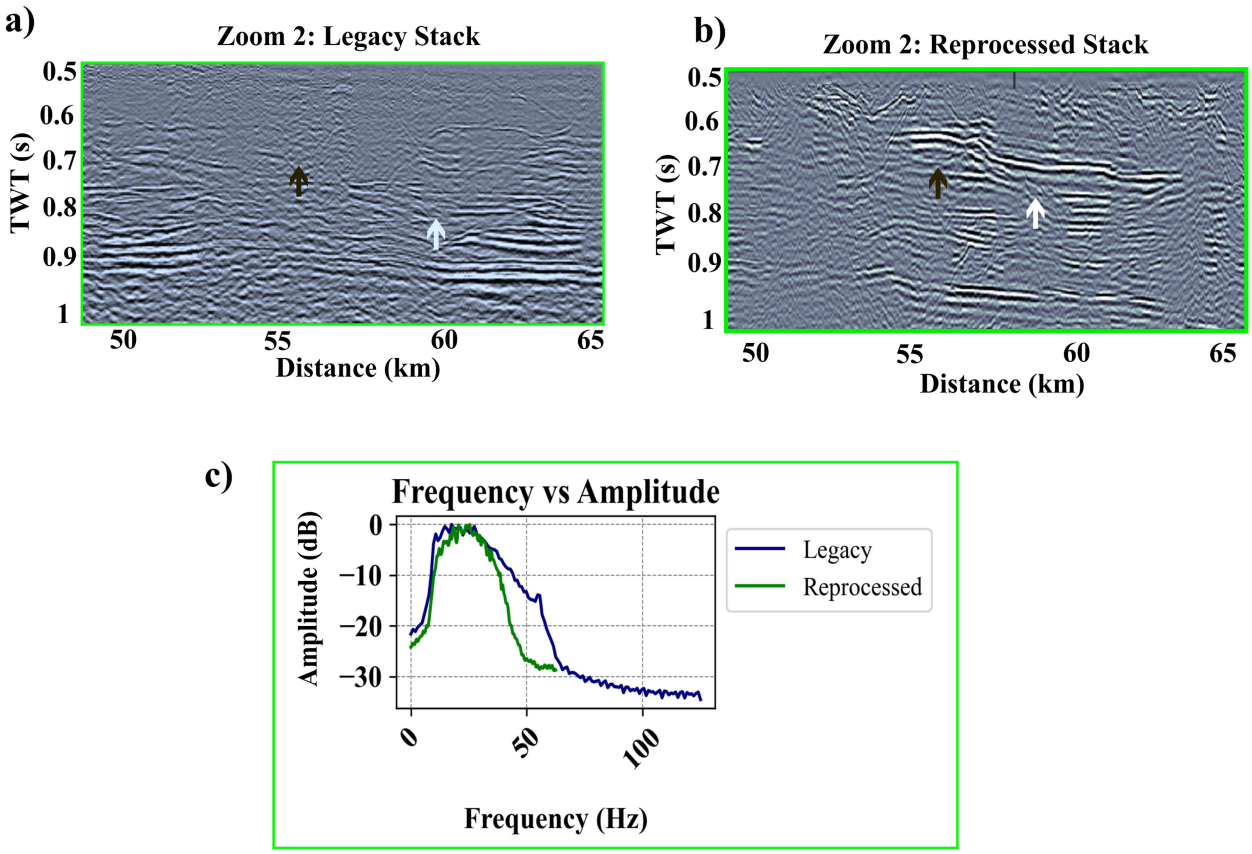

Figure 5.3: Close-up areas of the legacy stack (a) and reprocessed stack (b) with a frequency spectrum graph obtained for these particular sections (c). The reprocessed data (b) clearly image the continuity of the base of the Ecca Group with increased quality as compared to the legacy one (a). This is shown using black and white arrows in the figure. The frequency trend of the reprocessed data is evidently smoother than the legacy data. The key observation here is that the higher frequencies on the legacy spectrum are highly eliminated in the reprocessed section. The high frequencies on the legacy data are related to noise.

Figures 5.4 and 5.5 zoom into more areas in the stack where significant improvements have been achieved. In summary, the comparative analysis between the legacy and reprocessed data, as illustrated in Figures 5.1 - 5.5, underscore the significant advancements in seismic data processing. The reprocessed data not only offers a clearer visualization of geological structures, such as the sill and the base of the Beaufort Group but also presents a more refined frequency spectrum. This enhancement in data quality can be largely attributed to the advanced processing techniques. Such improvements are pivotal, as they provide geoscientists with a more accurate and detailed understanding of subsurface structures, ultimately aiding in more informed decision-making in exploration

and research endeavors.

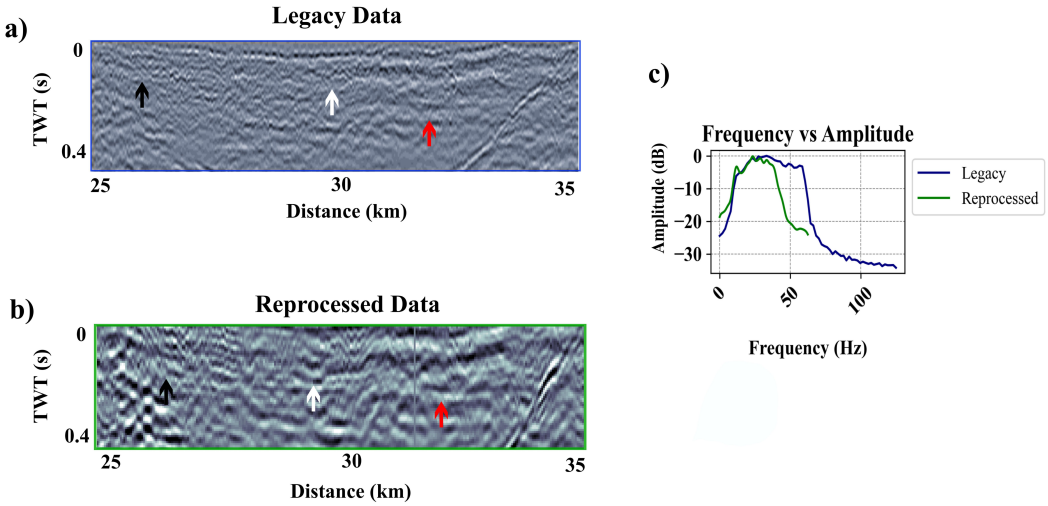

Figure 5.4: Close-up areas of the legacy stack (a) aligned with those of the reprocessed stack (b). The black, white, and red arrows point to possible reflection events enhanced by reprocessing. (c) Corresponding frequency spectrum. High frequencies on the legacy spectrum are eliminated in the reprocessed section.

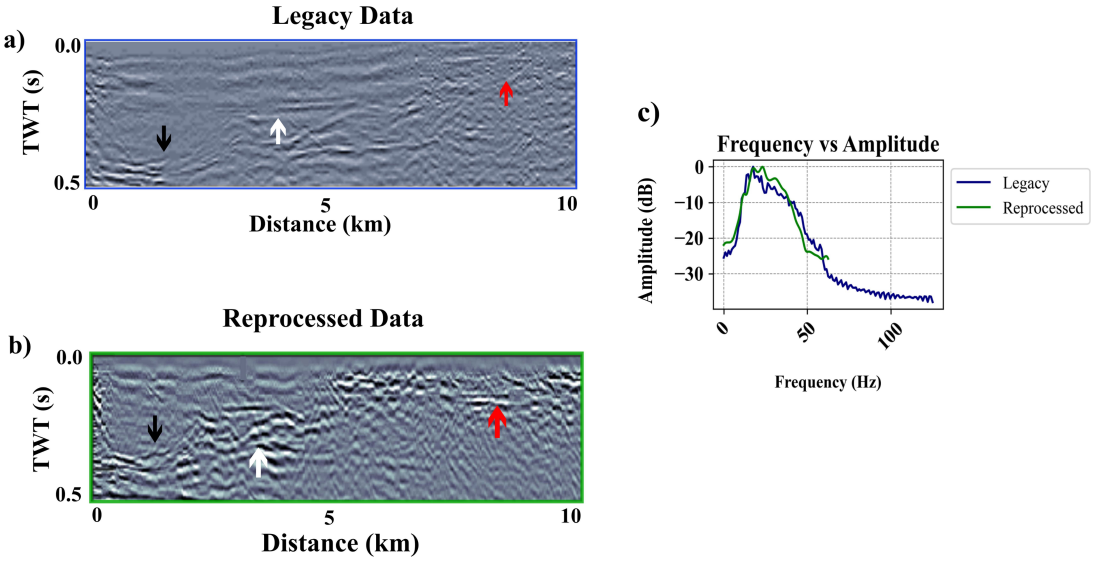

Figure 5.5: Close-up areas of the legacy stack (a) aligned with those of the reprocessed stack (b). The black, white, and red arrows point to possible reflection events enhanced by reprocessing. (c) Corresponding frequency spectrum. High frequencies on the legacy spectrum are eliminated in the reprocessed section.

5.3 Interpretations

5.3.1 Refraction Tomography

Figure 5.6 is the elevation profile for the entire seismic line. A refraction tomography or velocity model for the near-surface velocity variations of the entire RT480 profile is also shown in Figure 5.7. Geological observations and data were used to interpret the reflections. This seismic tomogram was utilized to impose constraints when interpreting the seismic data.

It is evident in Figure 5.7 (a) that the top layer is characterized by P-wave velocities that range from 1100 m/s to 2525 m/s at an estimated depth of 1100 m. Secondly, the weathering layer occurs at an estimated depth of 1300 m and is characterized by P-wave velocities that range between 2600 m/ and 3950 m/s. Moreover, one can also observe that it is possible to associate the bedrock with P-wave velocities that range between 4000 m/s and 4700 m/s at an estimated depth of 1700 m.

The P-wave velocity of the top layer is in agreement with the sandstone, siltstone, and shale rocks while the weathering layer and the bedrock velocities agree with the dolerites and turbidites (Scheiber-Enslin et al., 2021). In addition, one may associate some of the high P-wave velocity regions with the dolerite intrusions that occur across the profile. Some of these regions are labeled with arrows. The seismic ray path diagram is also shown in Figure 5.7 (b) which represents the path along which the seismic wave energy propagated through the rocks.

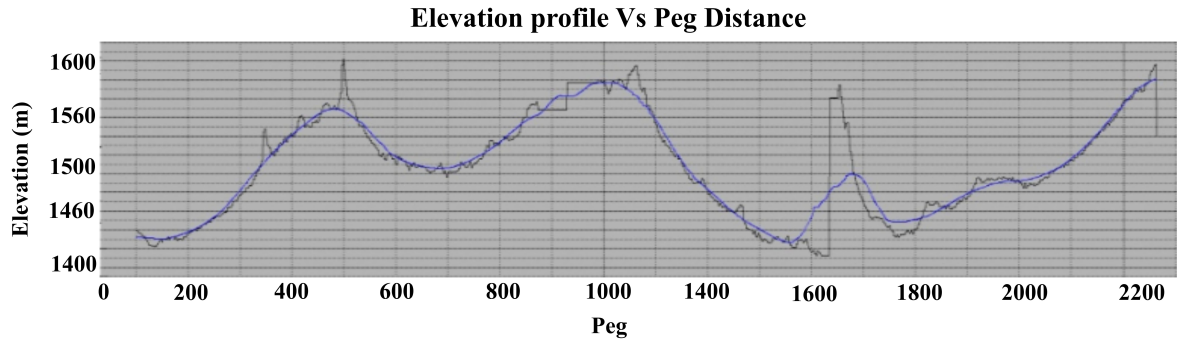

Figure 5.6: Elevation profile of RT480. Here, the elevation difference (black line) across the survey line is plotted against peg numbers (blue line) assigned to each shot and receiver location.

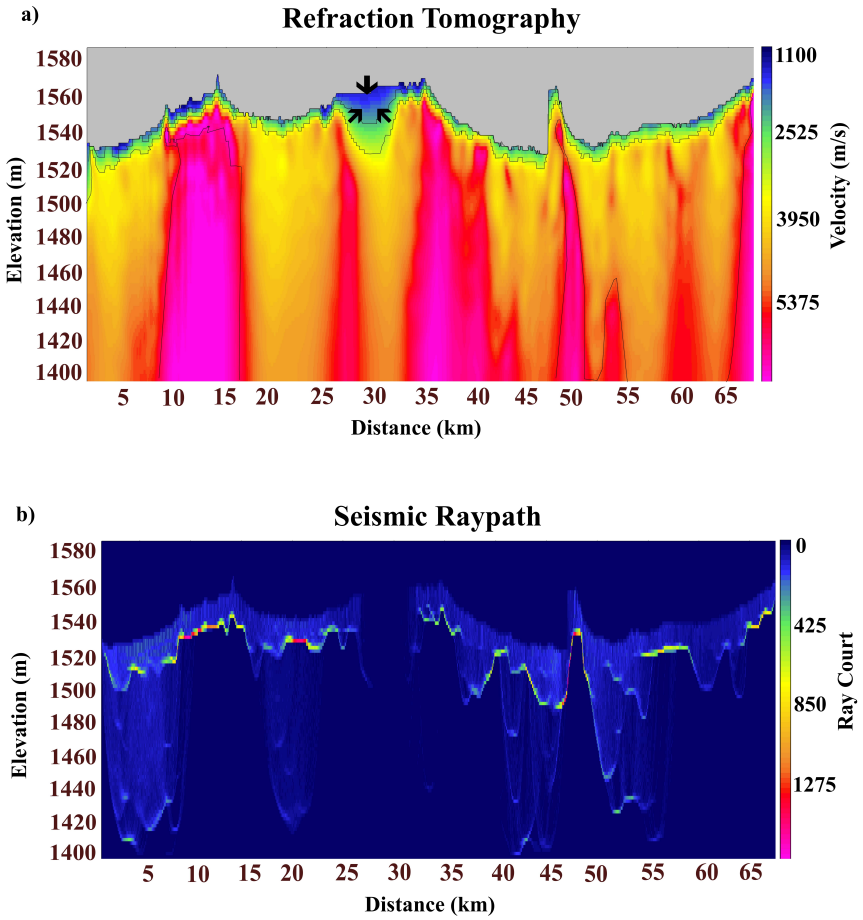

Figure 5.7: (a) The refraction tomography of P-wave velocities for the data. (b) The path followed by the seismic waves during propagation (ray path diagram).

5.3.2 Seismic Section

Interpretation of the area can only be limited to apparent dips and thicknesses of the individual reflectors since a comprehensive three-dimensional interpretation of the region is not achievable using a 2D seismic section. With a depth extension of 4.5 km and a distance along the profile of nearly 65 km, the vertical exaggeration on the seismic section is noteworthy. The results exhibit an estimated 1:14 vertical exaggeration, suggesting that 13 more pages should be added to the seismic section to acquire the proper dip on the possible features. As a result, features look steeper in Figure 5.8 than they actually are.

Figure 5.8 (a) zooms into the prominent near-surface events by displaying the post-stack time migrated zero offset data (less than 4 km deep), and Figure 5.8 (b) shows a

simple stratigraphic interpretation that is superimposed over the data. The section is distinguished by a powerful reflection package that can be found between 0.6 and 1.1 s TWT in the northwest (NW) end of the profile. This package then gently dips southeastwards and can be found between 1.25 and 1.85 s in the southeast (SE) end of the profile. According to De Wit and Tinker (2004), it has an average thickness of 1250 m and it is understood as being the Ecca Group of the Karoo Supergroup. The strong acoustic impedance between the Groups Ecca and Dwyka is caused by the changes in velocity and density as the seismic waves propagate through the layers.

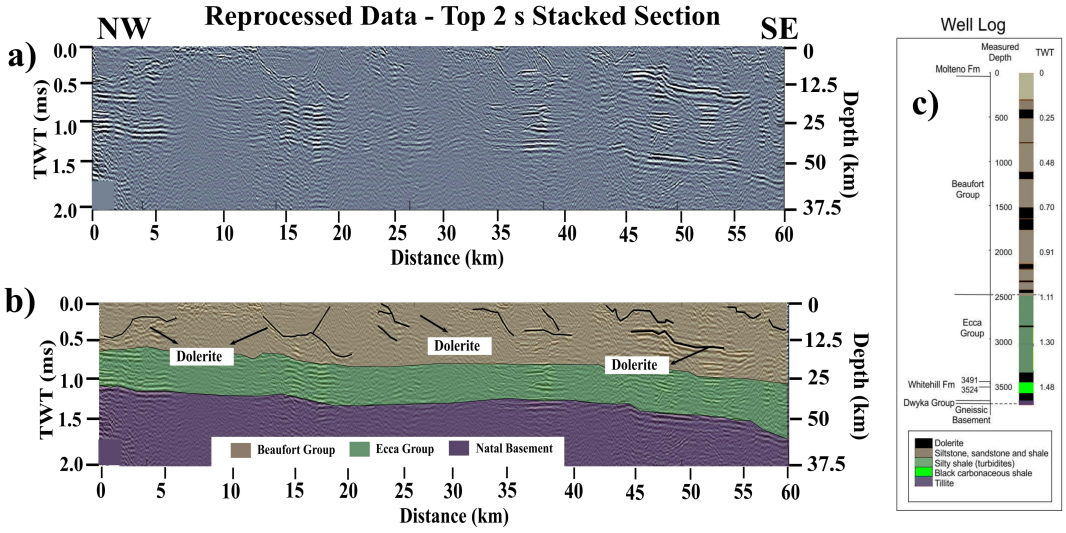

Figure 5.8: (a) Top 2 s TWT of time migrated zero offset seismic section for profile RT480 with prominent near-surface events highlighted. (b) One can interpret the three major stratigraphic groups and dolerite intrusions. (c) Well log WE 1/66 (Scheiber-Enslin et al., 2021).

The Beaufort Group sits above the Ecca Group; it has an average thickness of 2 km according to De Wit and Tinker (2004) and is peppered with Karoo dolerite sills throughout its composition (Figure 5.8 (b)). These dolerite intrusions make up between 10 to 30 percent of the Karoo Basin's thickness (Chere et al., 2017). At smaller depths of 1.0 s TWT (less than 2 km in the subsurface), saucer-shaped reflectors suggest the presence of shallower sills which are situated 3 km below ground surface (Figure 5.8 (b)) (Scheiber-Enslin et al., 2021). Figure 5.9 provides a closer look into the section to highlight the dolerite sills and some of the geological boundaries such as the top of the Beaufort Group and the base of the Ecca Group.

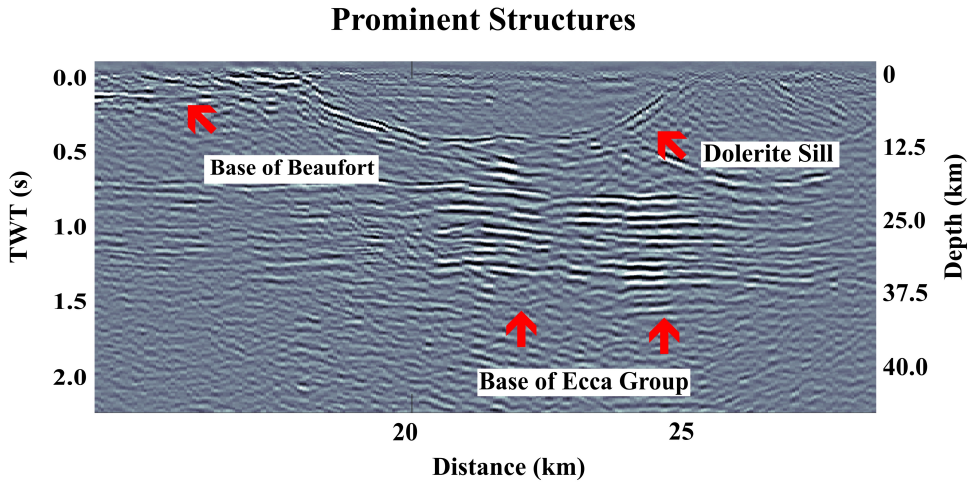

Figure 5.9: Seismic section highlighting some of the geological artifacts such as sills and boundaries. The red arrows point to the features as labeled in the figure.

The gas escape features observed in Figure 5.10 were also observed by Scheiber-Enslin et al. (2021). These features may be associated with the hydro-thermal vents present in the area and may have resulted from the heating of shale rocks and caused hydrocarbons to mature, thereby causing gas to escape out of the subsurface.

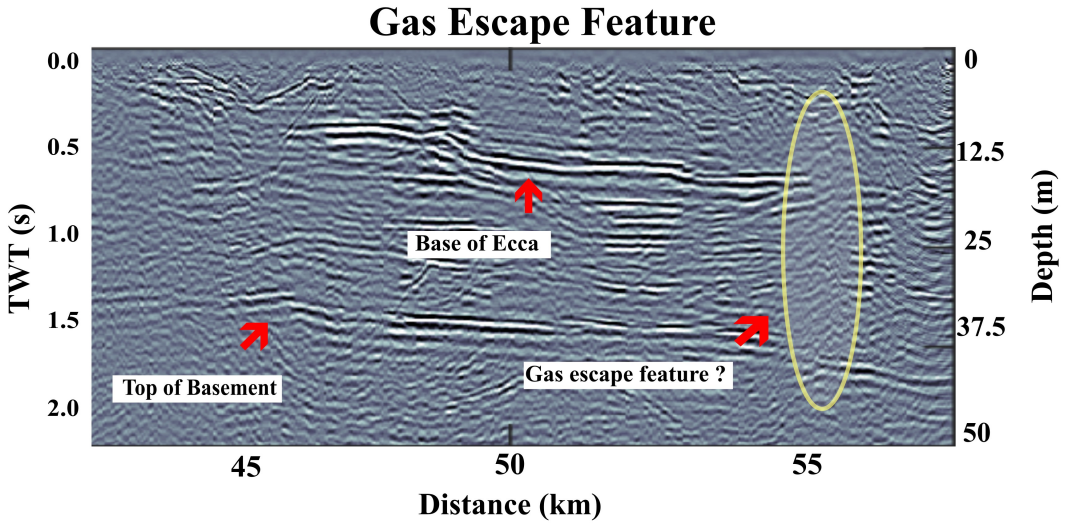

Figure 5.10: Seismic section highlighting major geological boundaries (red arrows) and an example of a gas escape feature (yellow oval shape).

Figure 5.11 (a) shows the stack for the entire profile. The profile traverses the southern-

most part of the Kaapvaal craton (De Wit and Tinker, 2004). Seismic reflectors in the top crust seem to be originating from two different crustal blocks that are separated along a southeast dipping boundary. This boundary is thought to represent the thrust border between the Kaapvaal craton (footwall) and the overlaying younger Natal-Namaqua crust (about 1.2 to 1.0 Ga, in the hanging wall) (De Wit and Tinker, 2004). This is in very good accord with both the geology of the surface (Thomas et al., 1994) and the depth-integrated thermochronology (Schmitz and Bowring, 2003). Moreover, one can observe dipping reflections between 4 s to 6 s TWT (6.5 to 8.5 km deep), which might be associated with other geological intrusions worth investigating. The depths of the Karoo Supergroup layers are constrained based on the results obtained from well log WE 1/66 (Figure 5.11 (b)).

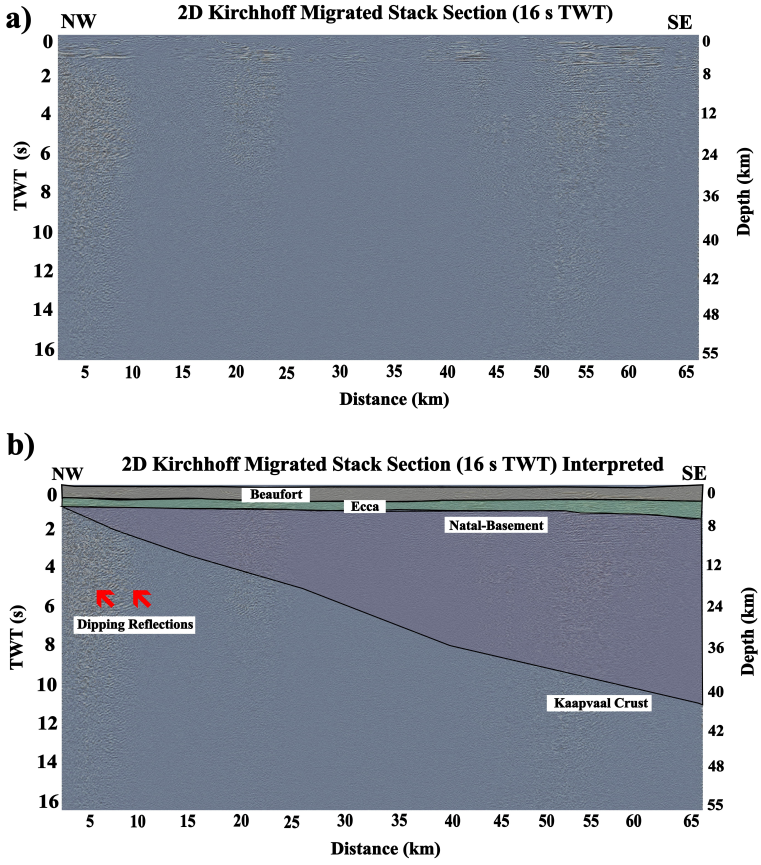

Figure 5.11: Full 16 s two-way traveltime (TWT) post-stack time migrated seismic section. Major reflection events are evident on the stack, mostly in the top 2 s TWT.

6. Conclusion

The reprocessed seismic profile RT480 not only offered greater precision in imaging but also allowed for a more detailed characterization of the subsurface geology. By revealing the intricate details of geological boundaries and the distribution of dolerite intrusions within the Karoo Basin, the project significantly enhanced the geological model of the area. Such detailed mapping is critical, especially when considering the complex geology that characterizes shale gas reservoirs. The improved seismic data quality has proven to be a pivotal factor in de-risking the exploration process, ensuring that subsequent exploratory drilling can be more accurately targeted.

Moreover, the use of advanced algorithms facilitated some discernment of finer geological features, which were previously indistinguishable. The ability to identify and analyze these features is essential for understanding the depositional environment and tectonic history of the basin. As a result, the findings from the reprocessed data have the potential to reshape the current understanding of the Karoo Basin's geology. This is particularly relevant for the identification of sweet spots for shale gas exploration, as dolerite intrusions can significantly impact the quality and quantity of recoverable resources.

In conclusion, the successful reprocessing of seismic data not only improves the resolution of the images but also amplifies our knowledge of the basin's geology. This enhancement in data quality is a significant leap forward in the quest for energy resources in South Africa and exemplifies the profound impact that technological advancements can have on the field of geosciences. The project, therefore, sets a new benchmark for seismic studies in the region and could serve as a blueprint for similar ventures aiming to unlock the hidden potential of subsurface resources.

References

Aarnes, I., F. Kirsten, P. Sverre, and S. Henrik, 2011, The impact of host-rock composition on devolatilization of sedimentary rocks during contact metamorphism around sheet intrusions: Geochemistry, Geophysics, Geosystems, **12(10)**, 2011.

Adam, E., B. Milkereit, and M. Mareschal, 1998, Seismic reflection and borehole geophysical investigations in the Matagami mining camp: Canadian Journal of Earth Sciences, **35(6)**, 686–695.

Al-Sadi, H. N., 1980, Seismic exploration technique and processing: Journal of the Canadian Society of Exploration Geophysicists.

Arias, A., F. J. Sanchez-Sesma, and E. Ovando-Shelley, 1981, A simplified elastic model for seismic analysis of earth-retaining structures with limited displacements: Proc., Int. Conf. on Recent Adv. in Geotech. Earthquake Engrg. and Soil Dyn., Univ. of Missouri, Rolla, Mo, 635–642.

Baker, B. B., and E. T. Copson, 2003, The mathematical theory of Huygens' principle: American Mathematical Society.

Ben-Menahem, A., and S. S. Jit, 2012, Seismic waves and sources: Springer Science and Business Media.

Bolt, B. A., 1978, Earthquakes: a primer.

Bonomi, E., and G. Cabitza, 1994, Migration of seismic data: Journal of Statistical Physics, **76**, 703-723.

Born, M. and E. Wolf, 2013, Principles of optics: Electromagnetic theory of propagation, interference and diffraction of light: Elsevier.

Botha, W. and J. B. Linstrom, 1978, A note on the stratigraphy of the Beaufort Group in north-western Natal: South African Journal of Geology, **81**, 35-40.

Brijs, T., G. Swinnen, K. Vanhoof, and G. Wets, 1999, Using association rules for product assortment decisions: A case study, In Proceedings of the Fifth ACM SIGKDD International Conference on Knowledge Discovery and Data Mining, 254-260.

Catuneanu, O., P. J. Hancox, and B. S. Rubidge, 1998, Reciprocal flexural behaviour and contrasting stratigraphies: A new basin development model for the Karoo retroarc foreland system, South Africa: Basin Research, **10**, 417-440.

Cawthorn, R. G., 2012, Distribution of dolerite sills in the Karoo Supergroup, In Extended Abstract LASI 5 Conference, **29**, 30.

Chapman, L., G. L. Brown, and D. W. Fair, 1981, The Vibroseis system: A high-frequency tool: Geophysics, **46(12)**, 1657-1666.

Chen, Y., J. Yuan, S. Zu, S. Qu, and S. Gan, 2015, Seismic imaging of simultaneous-source data using constrained least-squares reverse time migration: Journal of Applied Geophysics, **114**, 32 - 35.

Chen, Y., H. Chen, K. Xiang, and X. Chen, 2017, Preserving the discontinuities in least-squares reverse time migration of simultaneous source data: Geophysics, **82(3)**, S185-S196.

Chere, N., B. Linol, M. De Wit, and H. M. Schulz, 2017, Lateral and temporal variations of black shales across the southern Karoo Basin-implications for shale gas exploration: South African Journal of Geology, **120**, 541-564.

Christie, A. D. M., 1981, Stratigraphy and sedimentology of the Molteno Formation in the Elliot and Indwe area, Cape Province: Phd thesis, University of Kwazuli-Natal.

Chun, J. H. and C. A. Jacewitz, 1981, Fundamentals of frequency domain migration: Geophysics, **46**, 717-733.

Coetzee, J., 2018, The effect of physical properties on the reflection seismic method: Implications for shale gas exploration in the Main Karoo Basin, South Africa: MSc. thesis, University of the Witwatersrand.

Cole, D. I., 1992, Evolution and development of the Karoo Basin, In Conference on Inversion Tectonics of the Cape Fold Belt, 87-99.

Gerald, L., D. S. Spain, W. S. Hodgkiss, and E. L. Edmonds, 1991, The simultaneous measurement of infrasonic acoustic particle velocity and acoustic pressure in the ocean by freely drifting swallow floats: IEEE Journal of Oceanic Engineering, **16**, 195-207.

De Wit, M and Tinker, J., 2004, Crustal structures across the central kaapvaal craton from deep-seismic reflection data, South African Journal of Geology, **107**, 185 - 206.

Dean, D. R. and R. Mallet, 1991, The founding of seismology: Annals of Science, **48**, 39-67.

Decker, J.E. and Marot, J., 2012. Annexure A: Resource Assessment (Editors), In: Department of Mineral Resources, 2012. Report on Investigation of Hydraulic Fracturing in the Karoo Basin of South Africa. 81p., 15 annexures.

Du Toit, A. L., 1920, The Karroo dolerites of South Africa: A study in hypabyssal injection: South African Journal of Geology, **23**, 1-42.

Duncan, A. R. and Marsh, J.S., 2006. The Karoo Igneous Province: Geological Society of South Africa and Council for Geoscience, 461–499.

Duncan, R. A., P. R. Hooper, J. Rehacek, J. Marsh, and A. R. Duncan, 1997, The timing and duration of the Karoo igneous event, southern Gondwana: Journal of Geophysical Research, **102**, 18127-18138.

Egbai, J. C., E. Atakpo, and C. O. Aigbogun, 2012, Predictive deconvolution in seismic data processing in Atala prospect of Rivers State, Nigeria: Advances in Applied Science Research, **3**, 520-529.

Ellis, S. and B. Stöckhert, 2004, Elevated stresses and creep rates beneath the brittle-ductile transition caused by seismic faulting in the upper crust: Journal of Geophysical Research, **109(B5)**.

Eriksson, P. G., 1984, A palaeoenvironmental analysis of the Molteno Formation in the Natal Drakensberg: South African Journal of Geology, **87**, 237-244.

Evans, B., 1997, A handbook for seismic data acquisition in exploration: Society of exploration geophysicists, **7**, 1-150.

Fathi, A., B. Poursartip, H. K. Stokoe, and L. F. Kallivokas, 2016, Three-dimensional P- and S-wave velocity profiling of geotechnical sites using full-waveform inversion driven by field data: Soil Dynamics and Earthquake Engineering, **87**, 63-81.

Fomel, S., E. Landa, and M. T. Taner, 2007, Poststack velocity analysis by separation and imaging of seismic diffractions: Geophysics, **72**, 89-94.

Fouch, M. J., E. D. James, J. C. VanDecar, and S. Van der Lee, 2004, Kaapvaal Seismic Group. Mantle seismic structure beneath the Kaapvaal and Zimbabwe cratons: South African Journal of Geology, **107**, 33-44.

Geometrics, 2015, What is an "air wave"? - Geometrics: Geophysics, **80**, G15-G26.

Hale, D., 1992, Migration by the Kirchhoff, slant stack, and Gaussian beam methods: Technical report, Colorado School of Mines, Golden, CO (United States), Center for Wave Phenomena.

Hansen, D. M., A. J. Cartwright, and D. Thomas, 2004, 3D seismic analysis of the geometry of igneous sills and sill junction relationships: Geological Society, London, Memoirs, **29(1)**, 199-208.

Hatton, L., M. H. Worthington, and J. Makin, 1986, Seismic data processing: Theory and practice: Technical report, Merlin Profiles Ltd.

Idier, J. and Y. Goussard, 1993, Multichannel seismic deconvolution: IEEE Transactions on Geoscience and Remote Sensing, **31(5)**, 961-979.

Kim, J., M. W. Moon, J. A. Percival, and F. G. West, 1992, Seismic imaging of shallow reflectors in the eastern Kapuskasing structural zone, with correction of crossdip attitudes: Geophysical Research Letters, **19(20)**, 2035–2038.

Kiran, K. T., 2D and 3D land seismic data acquisition and seismic data processing: College of Science and Technology, Andhra University, Andhra Pradesh, India.

Kuster, G. T. and M. N. Toksöz, 1974, Velocity and attenuation of seismic waves in two-phase media: Part I. Theoretical formulations: Geophysics, **39(5)**, 587-606.

Kuznetsov, S. V., 2011, Seismic waves and seismic barriers: Acoustical Physics, **57**, 420-426.

Landa, E., S. Fomel, and M. Reshef, 2008, Separation, imaging, and velocity analysis of seismic diffractions using migrated dip-angle gathers: In 2008 SEG Annual Meeting, OnePetro, **27(1)**, 2176-2180.

Leith, M. J., 1970, Well completion report of SP1/69: Internal Soekor Report PSV684a, 37.

Levin, F. K., 1971, Apparent velocity from dipping interface resections: Geophysics, **36(3)**, 510-516.

Linol, B., N. Chere, T. Muedi, V. Nengovhela, and M. J. De Wit, 2016, Deep borehole lithostratigraphy and basin structure of the southern Karoo Basin re-visited: In Origin and evolution of the Cape Mountains and Karoo Basin, Springer International Publishing, 183 – 192.

Makama, A., K. Kuladinithi, and A. Timm-Giel, 2021, Wireless geophone networks for land seismic data acquisition: A survey, tutorial and performance evaluation: Sensors, **21(15)**, 5–171.

Malehmir, A., Bergman, B., Andersson, B., Sturk, R and Johansson, M., 2018, Seismic imaging of dyke swarms within the sorgenfreitornquist zone (sweden) and implications for thermal energy storage: Solid Earth, **9(6)**, 1469 - 1485.

Manzi, M. S. D., K. A. A. Hein, R. J. Durrheim, and N. King, 2014, The Ventersdorp Contact Reef model in the Kloof Gold Mine as derived from 3D seismics, geological mapping and exploration borehole datasets: International Journal of Rock Mechanics and Mining Sciences, **66**, 97–113.

Manzi, M. S. D., A. Malehmir, and R. J. Durrheim, 2019, Giving the legacy seismic data the attention they deserve: First Break, **37(8)**, 89–96.

McQuillin, R., M. Bacon, and W. Barclay, 1984, An introduction to seismic interpretation in petroleum exploration.

Mendel, J. M., 2013, Optimal seismic deconvolution: An estimation-based approach: Elsevier.

Nedimovic, M. R., and G. F. West, 2003, Crooked-line 2D seismic reflection imaging in crystalline terrains: Part 2, migration: Geophysics, **68(1)**, 286–296.

Nengovhela, V., B. Linol, L. Bezuidenhout, T. Dhansay, T. Muedi, and M. J. De Wit, 2021, Shale gas leakage in lower Ecca shales during contact metamorphism by dolerite sill intrusions in the Karoo Basin, South Africa: South African Journal of Geology, **124(2)**, 443–464.

Neveling, J., P. J. Hancox, and B. S. Rubidge, 2005, Biostratigraphy of the lower Burgersdorp Formation (Beaufort Group; Karoo Supergroup) of South Africa - implications for the stratigraphic ranges of Early Triassic tetrapods: Palaeontologia Africana, **41**, 81–87.

Nguyen, K. T. P., M. Jin Nam, and C. Park, 2015, A review on time-lapse seismic data processing and interpretation: Geosciences Journal, **19**, 375–392.

Onajite, E., 2013, Seismic data analysis techniques in hydrocarbon exploration: Elsevier.

Rapetsoa, M. K., and M. Manzi, 2021, In-mine seismic method for platinum orebody exploration in Maseve Platinum Mine, South Africa: NSG2021 2nd Conference on Geophysics for Infrastructure Planning, Monitoring and BIM, European Association of Geoscientists and Engineers, **2021**, 1–5.

Rost, S., and C. Thomas, 2002, Array seismology: Methods and applications: Reviews of Geophysics, **40(3)**, 2–1.

Rowsell, A. M. J., and D. M. De Swardt, 1976, Diagenesis in Cape and Karroo sediments, South Africa, and its bearing on their hydrocarbon potential: South African Journal of Geology, **79(1)**, 81–145.

Rubidge, B. S., Biostratigraphy of the Beaufort Group (Karoo Supergroup): South African Committee for Stratigraphy Biostratigraphic Series, 45.

Scheiber-Enslin, S., S. J. Webb, and J. Ebbing, 2014, Geophysically plumbing the main Karoo Basin, South Africa: South African Journal of Geology, **117(2)**, 275–300.

Scheiber-Enslin, S. E., M. Manzi, and S. J. Webb, 2021, Seismic imaging of dolerite sills and volcanic vents in the central Karoo, South Africa: Implications for shale gas potential: South African Journal of Geology, **124(2)**, 465–480.

Schmelzbach, C., A. G. Green, and H. Horstmeyer, 2005, Ultra-shallow seismic reflection imaging in a region characterized by high source-generated noise: Near Surface Geophysics, **3(1)**, 33–46.

Schmitz, D. M., and S. A. Bowring, 2003, Ultra-high temperature metamorphism in the lower crust during Neoarchean Ventersdorp rifting and magmatism, Kaapvaal Craton, Southern Africa: Geological Society of America Bulletin, **115(5)**, 533–548.

Schneider, W. A., 1971, Developments in seismic data processing and analysis: Geophysics, **36(6)**, 1043–1073.

Sheriff, R. E., and P. L. Geldart, 1995, Exploration Seismology: Cambridge University Press.

Sheriff, R. E., 2002, Encyclopedic Dictionary of Applied Geophysics: Society of Exploration Geophysicists.

Sleep, N. H., and N. Nakata, 2015, Nonlinear attenuation from the interaction between different types of seismic waves and interaction of seismic waves with shallow ambient tectonic stress: Geochemistry, Geophysics, Geosystems, **16(7)**, 2336–2363.

Smith, R. M. H., P. G. Eriksson, and W. J. Botha, 1993, A review of the stratigraphy and sedimentary environments of the Karoo-aged basins of southern Africa: Journal of African Earth Sciences (and the Middle East), **16(1-2)**, 143–169.

Stavrakis, N., 1980, Sedimentation of the Katberg Sandstone and adjacent formations in the southeastern Karoo Basin: South African Journal of Geology, **83(3)**, 361–374.

Stolt, R. H., 1978, Migration by Fourier transform: Geophysics, **43(1)**, 23–48.

Svensen, H., S. Planke, A. Malthe-Sørenssen, B. Jamtveit, R. Myklebust, T. R. Eidem, and S. S. Rey, 2004, Release of methane from a volcanic basin as a mechanism for initial Eocene global warming: Nature, **29(6991)**, 542–545.

Svensen, H., B. Jamtveit, S. Planke, and L. Chevallier, 2006, Structure and evolution of hydrothermal vent complexes in the Karoo Basin, South Africa: Journal of the Geological Society, **163(4)**, 671–682.

Telford, W. M., L. P. Geldart, and R. E. Sheriff, 1990, Applied Geophysics: Cambridge University Press.

Thomas, R. J., A. L. D. Agenbacht, D. H. Cornell, and J. M. Moore, 1994, The Kibaran of Southern Africa: Tectonic evolution and metallogeny: Ore Geology Reviews, **9(2)**, 131–160.

Thomas, R. J., D. H. Cornell, and R. A. Armstrong, 1999, Provenance age and metamorphic history of the Quha Formation, Natal Metamorphic Province: A U-Th-Pb zircon SHRIMP study: South African Journal of Geology, **102(1)**, 83–88.

Visser, J. N. J., 1986, Lateral lithofacies relationships in the glacigene Dwyka Formation in the western and central parts of the Karoo Basin: Transactions of the Geological Society of South Africa, **89**, 373–383.

Visser, J. N. J., 1987, The palaeogeography of part of southwestern Gondwana during the Permo-Carboniferous glaciation: Palaeogeography, Palaeoclimatology, Palaeoecology, **61**, 205–219.

Visser, J. N. J., 1992, Deposition of the early to late Permian Whitehill Formation during a sea-level highstand in a juvenile foreland basin: South African Journal of Geology, **95(5)**, 181–193.

Wang, H., M. Li, and X. Shang, 2016, Current developments on micro-seismic data processing: Journal of Natural Gas Science and Engineering, **32**, 521–537.

Westgate, M., M. S. D. Manzi, I. James, and W. Harrison, 2020, New insights from legacy seismic data: Reprocessing of legacy 2D seismic data for imaging of iron-oxide mineralization near Sishen Mine, South Africa: Geophysical Prospecting, **68(7)**, 2119–2140.

Widess, M. B., 1973, How thin is a thin bed? Geophysics, **38(6)**, 1176–1180.

Wiener, N., 1949, Extrapolation, interpolation, and smoothing of stationary time series: with engineering applications. The MIT press.

Wilson, J. C., and M. J. Wesolowsky, 2005, Shape memory alloys for seismic response modification: A state-of-the-art review: Earthquake Spectra, **21(2)**, 569–601.

Winter, R., and J. J. Venter, 1970, Lithostratigraphic correlation of recent deep boreholes in the Karroo-Cape Sequence: Soekor, 395-408.

Woodward, M. J., 1992, Wave-equation tomography: Geophysics, **57(1)**, 15–26.

Xu, S., and A. Stovas, 2018, Fresnel zone in VTI and orthorhombic media: Geophysical Journal International, **213(1)**, 18–193.

Xue, Z., Y. Chen, S. Fomel, and J. Sun, 2016, Seismic imaging of incomplete data and simultaneous-source data using least-squares reverse time migration with shaping regularization: Geophysics, **81(1)**, S11–S20.

Yilmaz, O., 2001, Seismic Data Analysis: Society of Exploration Geophysicists Tulsa, **1**.

Yin, Z., Y. Zhou, and Y. Li, 2020, Seismic exploration wireless sensor system based on Wi-Fi and LTE: Sensors, **20(4)**, 10–18.

Yu, C., S. Ji, and Q. Li, 2016, Effects of porosity on seismic velocities, elastic moduli and Poisson's ratios of solid materials and rocks: Journal of Rock Mechanics and Geotechnical Engineering, **8(1)**, 35–49.

Zhou, H-W., 2014, Practical Seismic Data Analysis: Cambridge University Press.

Zong, Z., X-Y. Yin, F. Zhang, and G. Wu, 2012, Reflection coefficient equation and pre-stack seismic inversion with Young's modulus and Poisson ratio: Chinese Journal of Geophysics, **55(11)**, 3786–3794.